Disorder-induced localization effects in nitride semiconductor compounds and devices

Wiebke Hahn

INSTITUT POLYTECHNIQUE DE PARIS

NNT : 2020IPPAX049

Thèse de doctorat

Disorder-induced localization effects in nitride semiconductor compounds and devices

Thèse de doctorat de l'Institut Polytechnique de Paris
préparée à École Polytechnique

École doctorale n°626 École Doctorale
de l'Institut Polytechnique de Paris (ED IP Paris)
Spécialité de doctorat : Physique

Thèse présentée et soutenue à Palaiseau de soutenance, le 17/09/2020, par

Wiebke Hahn

Composition du Jury :

Nicolas Grandjean Professeur École Polytechnique Fédérale de Lausanne – LASPE, Suisse	Rapporteur
Philippe Dumas Professeur, Aix-Marseille Université – CINaM, France	Rapporteur
James S. Speck Professeur UCSB – Materials Department, États-Unis	Examinateur
Sir Richard Friend Professeur University of Cambridge – Cavendish Laboratory, Royaume-Uni	Examinateur
Silke Biermann Professeur École Polytechnique – CPHT, France	Présidente
Mathieu Kociak Directeur de Recherche Université Paris Sud – LPS, France	Examinateur
Jacques Peretti Directeur de Recherche École Polytechnique – LPMC, France	Directeur de thèse
Claude Weisbuch Professeur École Polytechnique – LPMC, France UCSB – Materials Department, États-Unis	Co-encadrant

Institut Polytechnique de Paris
91120 Palaiseau, France

To my family

Acknowledgements

I strongly believe that true progress can only be achieved when people with different expertise come together to work for the best outcome possible. I was lucky to pursue my PhD thesis in such an environment. Therefore, I thank Mathis Plapp for welcoming me as a PhD student in the Laboratoire de Physique de la Matière Condensée at École Polytechnique.

I would like to express my deep gratitude to my supervisors and my mentor: Jacques Peretti, Yves Lassailly, and Claude Weisbuch. Jacques gave me the freedom to work and develop this scientific project. At the same time, he encouraged me enthusiastically with his useful critiques and comments. Yves taught me valuable lessons on the experimental study of semiconductors and offered me generous support far beyond the usual. Claude is a real mentor. He has shaped my scientific way of thinking and problem-solving. He also introduced me to the scientific community and let me build important connections. The discussions with Jacques, Yves, and Claude have always been illuminating, inspiring, and most of all motivating. I thank them for their generous support, guidance, and persistent help. I will always be in their intellectual debt.

As every PhD student from the Laboratoire de Physique de la Matière Condensée (LPMC), I am particularly grateful for the tremendous assistance given by Lucio Martinelli. Lucio always took the time to answer all of my questions from UHV leak detection and building a new optical setup to “where can I buy Pecorino Romano in Paris?”.

I would like to extend my sincere thanks to the whole “Electrons-Photons-Surfaces” group of LPMC. Especially, I would like to thank Fausto Sirotti and Alistair Rowe for the help with the UHV chamber as well as the development of the STL setup.

Many thanks to the Irregularity group of LPMC, in particular to Marcel Filoche and Jean-Marie Lentali, for the theoretical modeling and calculations, but also to Abel Thayil, Pierre Pelletier and Jean-Philippe Banon, for the fruitful discussions.

It has been a great pleasure to work with Mylène Sauty. We make quite a team! I especially thank her for all her questions and her strong motivation. I am sure she will achieve great things with the STL experiment.

I would also like to express my gratitude to the help of Fouad Maroun. He has been a great support in implementing the homemade adaptions to the Omicron STM, coding in LabVIEW, and taking the SEM measurements.

Thanks should also go to André Wack for the fabrication of mechanical components, to Didier Lenoir for building the electronic circuits for the STM, and to Sandrine Tusseau-Nenez for the HRXRD measurements.

From the moment I set foot at LPMC, I always felt welcome due to the friendly and at the same time inspiring atmosphere between all the members of the laboratory. It has been a real pleasure to be part of this laboratory.

I would also like to acknowledge the financial support of the French National Research Agency (ANR)[1], the Labex Nano-Saclay[2] as well as the Simons foundation[3]. Many thanks go to our (international) collaborators, in particular, at the University of California in Santa Barbara, for the growth of the samples, as well as at the Institut des Sciences Moléculaires d'Orsay, for inviting me to conduct experiments in their laboratory.

Thanks to Aurélien David for fruitful discussions and the samples grown at Soraa Inc.

I would also like to thank the “Freundestorus” back in Germany. Without them, studying physics would have been much harder and less fun.

I cannot begin to express my gratitude to my family who always encourages and supports me without doubt. Without them this journey would not have been possible.

Finally, I would like to thank Valerio Peri. I am deeply grateful for all of his support throughout the ups and downs of the rollercoaster of emotions of this research project as well as all his valuable comments and suggestions on this manuscript. Thank you very much for everything. You are my safe harbor!

[1] This work was supported by the French National Research Agency (ANR): CRIPRONI and ELENID projects, grants No. ANR-14-CE05-0048-01 and ANR-17-CE24-0040-01.

[2] This work was supported by the ELIDE project, a public grant overseen by the French National Research Agency (ANR) as part of the “Investissements d’Avenir” program: Labex NanoSaclay, reference ANR-10-LABX-0035.

[3] This work was supported by the Simons foundation: grant 601937.

Content

List of acronyms

1D DDCC	One-Dimensional Drift-Diffusion Charge Control
AFM	Atomic force microscopy
BBR	Band bending region
BEEM	Ballistic electron emission spectroscopy
CL	Cathodoluminescence
CR	Cosmic ray
DQW	Double quantum well
EELS	Electron energy loss spectroscopy
EMCCD	Electron-multiplying charge-coupled device
EQE	External quantum efficiency
FWHM	Full width at half maximum
HRXRD	High resolved X-ray diffraction
HVPE	Hydride vapor phase epitaxy
HWHM	Half width at half maximum
Int.	Intensity
IQE	Internal quantum efficiency
ITO	Indium tin oxide
IV	Current-Voltage (characteristics)
LED	Light emitting diode
LL	Localization landscape theory
MBE	Molecular beam epitaxy
MOCVD	Metalorganic chemical vapor deposition
PL	Photoluminescence
QCSE	Quantum confined Stark effect
QW	Quantum well
RT	Room temperature
SEM	Scanning electron microscopy
SQW	Single quantum well
STEM	Scanning transmission electron microscopy
STL	Scanning tunneling electroluminescence
STM	Scanning tunneling microscopy
STS	Scanning tunneling spectroscopy
UHV	Ultra-high vacuum
UID	Unintentionally doped
UV	Ultraviolet

Introduction

English version

This PhD thesis deals with disorder-induced localization effects in nitride semiconductor compounds and devices by the experimental approach of scanning tunneling electroluminescence (STL) spectroscopy.

Throughout history lighting has played a crucial role in the development of humankind. Ever since, we have been looking for more efficient ways to produce light. Our means to produce light evolved from flames of burning materials such as in candles, oil lamps, kerosene and gas lamps, to resistive heating of filaments and Thomas Edison's incandescent light bulb [1], to the electron discharge in fluorescent lamps and finally to efficient solid-state lighting in light-emitting diodes (LEDs).

Nitride semiconductor compounds such as GaN, InN, AlN and their alloys are nowadays ubiquitous in optoelectronic devices, e.g., LEDs and lasers devices and power technologies. Their ultimately successful story begins more than hundred years ago. Their development required a slow but steady progress. Prominently, the discovery of solid-state light (SSL) emitters, the development of p-n junctions and their application to lighting, as well as the advancement in heterostructure fabrication played an essential role. The first LEDs based on SiC exhibited only a limited quantum efficiency of 2×10^{-9} , even in pure materials [2]. This low performance triggered a subsequent vast search for materials better suited for solid-state lighting. Although nitrides were already considered in the 60s and early 70s [3,4], they were subsequently neglected due to their many difficulties. These drawbacks, such as the lack of a native substrate, the poor growth quality of the material, the difficulty to p-dope GaN or its alloys were mainly overcome by the pioneering work of Isamu Akasaki, Hiroshi Amano and Shuji Nakamura. Their achievements finally led to efficient blue nitride-based LEDs and were awarded with the Nobel Prize in Physics in 2014 [5]. A complete review on the historical developments of LEDs and their challenges is provided by C. Weisbuch in [6–8].

The wide usage of the efficient nitride-based LEDs has a major impact on the energy consumption due to lighting. However, only with LEDs working at their physical limit energy savings of over 75% of the total energy consumption due to lighting can be achieved [9]. To push LEDs to their efficiency limit, further challenges of the III-nitride based semiconductors have to be overcome.

The goal of this PhD thesis is to foster our understanding of fundamental material properties of nitride ternary alloys. In particular, the objective of this thesis is to address the problem of localization effects induced by alloy disorder. The active region of opto-electronic devices commonly incorporates ternary alloys which exhibit intrinsic composition disorder due to the random positioning of atoms on the crystal lattice. In nitrides, the bandgap energy varies dramatically with alloy composition and spans over the whole spectral range from near IR to near UV. Therefore, the local intrinsic fluctuations of the alloy composition result in large potential fluctuations at the scale of a few nanometers which are thus expected to induce strong carrier localization effects that should impact the electronic processes. We have studied the localization effects due to alloy disorder in InGaN/GaN quantum wells at the relevant scale by an original local probe technique. The manuscript presented is structured as follows:

- **Chapter 1 – III-nitride semiconductors:**
  We introduce the challenges currently faced in III-nitride semiconductor compounds and devices related to the extrinsic to intrinsic material properties and their theoretical modeling.
- **Chapter 2 – Experimental method:**
  We describe the scanning tunneling electroluminescence (STL) setups and the experimental procedures that we developed to study disorder-induced localization effects in nitride ternary alloys.
- **Chapter 3 – Results:**
  We show the capabilities of our experimental approach to probe electronic processes at the nanometer scale in heterostructures containing a single InGaN/GaN quantum well and evaluate the effect of the intrinsic ternary alloy disorder on the carrier dynamics. We further compare our experimental findings to the predictions of the localization landscape theory.
- **Chapter 4 – Preliminary results on future research directions:**
  We present preliminary results on the investigation of several issues related to the disorder-induced localization effects: perpendicular transport in double quantum well structures, the temperature dependence of the local tunneling electroluminescence spectrum, a comparison of the local tunneling electroluminescence properties of samples produced in academic and industrial facilities, and the investigation of hole localization by STL in n-type InGaN/GaN structures.
- **Chapter 5 – Conclusion and perspectives:**
  Finally, we conclude this thesis by highlighting the main results and give some perspectives to further investigate the effects of alloy disorder on the electronic processes in nitride heterostructures and devices by STL. Moreover, we discuss the application of our experimental approach to study localization effects in other materials and show the latest developments of our setup.

Version française

L'objectif de cette thèse est la mise en évidence des effets de localisation induits par le désordre d'alliage dans les composés et dispositifs en nitrures semi-conducteurs par une approche expérimentale originale basée sur la microscopie d'électroluminescence à effet tunnel, dite STL.

Tout au long de l'histoire, l'éclairage a joué un rôle crucial dans l'évolution économique et sociale de l'humanité. La production de lumière a évolué de la combustion de matériaux comme la bougie, l'huile, le kérosène et le gaz, au chauffage de filaments résistifs comme dans l'ampoule à incandescence de Thomas Edison [1], à la fluorescence des gaz dans les lampes à décharge et enfin à l'électroluminescence dans les diodes semi-conductrices.

Les composés semi-conducteurs à base de nitrure, tels que le GaN, l'InN, l'AlN et leurs alliages, sont aujourd'hui largement utilisés dans les diodes électroluminescentes (LED), les lasers et l'électronique de puissance. Leur histoire à succès commence il y a plus de cent ans. Leur développement est le résultat d'un long processus de recherche fondamentale. La découverte des émetteurs de lumière à l'état solide, le développement des diodes à jonctions p-n, ainsi que les progrès réalisés dans la fabrication des hétérostructures ont constitué des étapes clés dans ce développement. Les premières LED à base de SiC, émettant du côté des courtes longueurs d'onde du spectre visible, n'ont montré qu'une efficacité quantique limitée à 2×10^{-9}, même dans des matériaux purs [2]. Cette performance modeste a suscité un vaste effort de recherche orienté vers des matériaux semi-conducteurs ayant de plus fortes efficacités quantiques. Bien que les nitrures aient été envisagés comme candidats potentiels dès les années 60 et au début des années 70 [3,4], ils ont par la suite été écartés en raison de nombreuses difficultés technologiques, telles que l'absence de substrat natif, la mauvaise qualité de croissance du GaN sur des substrats à fort désaccord de maille, la difficulté de réaliser un dopage de type p. C'est grâce aux travaux pionniers d'Isamu Akasaki, d'Hiroshi Amano et de Shuji Nakamura que la fabrication de LED à base de nitrure émettant efficacement dans le bleu a pu être développée. Cette découverte a été récompensée par le prix Nobel de physique en 2014 [5]. Une revue complète de l'historique du développement des LED et de leurs défis est présentée par C. Weisbuch dans [6–8].

L'utilisation de plus en plus large des LED à base de nitrure pour l'éclairage a un impact significatif sur la consommation d'énergie électrique. Cependant, pour réaliser les économies d'énergie attendues avec ces dispositifs, à savoir plus de 75 % de la consommation totale d'énergie due à l'éclairage [9], il est nécessaire de surmonter plusieurs difficultés liées aux propriétés intrinsèques des nitrures semi-conducteurs.

L'objectif de cette thèse de doctorat est la compréhension des propriétés électroniques fondamentales des alliages ternaires de nitrure et, plus particulièrement, des effets de localisation induits par le désordre d'alliage. En effets, la région active des dispositifs optoélectroniques incorpore généralement des alliages ternaires qui présentent un désordre de composition intrinsèque dû au positionnement aléatoire des atomes de l'alliage sur le réseau cristallin. Dans les nitrures, l'énergie de la bande interdite varie de façon abrupte avec la composition de l'alliage depuis le proche IR jusqu'au proche UV. Par conséquent, les fluctuations de composition dues au désordre intrinsèque d'alliage entraînent d'importantes fluctuations du potentiel électronique à l'échelle de quelques nanomètres qui induisent des effets de localisation des porteurs de charge. Au cours de ce travail, nous avons étudié les effets de localisation électronique dus au désordre d'alliage à l'échelle nanométrique dans les puits quantiques InGaN/GaN par une technique originale de microscopie à sonde locale qui permet d'accéder aux processus électroniques aux

échelles pertinentes. Ce travail est décrit dans le présent manuscrit de thèse qui est structuré comme suit :

- **Chapitre 1 - Les nitrures semi-conducteurs :**
  Nous introduisons les questions actuelles qui concernent les composés et dispositifs semi-conducteurs à base de nitrure, liées à leurs propriétés extrinsèques et intrinsèques ainsi qu'à leur modélisation théorique.
- **Chapitre 2 - Méthodes expérimentales :**
  Nous décrivons les dispositifs expérimentaux de microscopie STL que nous avons développés pour étudier les effets de localisation induits par le désordre d'alliage dans les composés ternaires de nitrures.
- **Chapitre 3 – Résultats :**
  Nous présentons les résultats de spectroscopie STL à l'échelle nanométrique obtenus sur des structures à puits quantiques InGaN/GaN et évaluons l'effet du désordre intrinsèque de l'alliage ternaire sur la dynamique des porteurs. Nous comparons ensuite nos résultats expérimentaux aux prédictions de la théorie du paysage de localisation.
- **Chapitre 4 - Résultats préliminaires sur les futurs axes de recherche :**
  Nous présentons des résultats préliminaires sur plusieurs problématiques que nous avons abordées qui concernent l'étude du transport perpendiculaire dans les structures à double puits quantique, la dépendance en température de l'électroluminescence locale, la comparaison des propriétés d'électroluminescence locale d'échantillons produits dans des installations universitaires et industrielles, et l'étude de la localisation des trous dans les structures InGaN/GaN de type n.
- **Chapitre 5 - Conclusion et perspectives :**
  Enfin, nous concluons cette thèse en mettant en évidence les principaux résultats obtenus et donnons des perspectives pour poursuivre l'étude, par la technique de microscopie STL, des processus électroniques à l'échelle du désordre d'alliage dans les nitrures. De plus, nous discutons de l'application de notre approche expérimentale à l'étude des effets de localisation dans d'autres matériaux et nous présentons les derniers développements de notre expérience.

1 III-nitride semiconductors

Although light-emitting diodes (LEDs) based on III-nitrides work already very efficiently and their applications led to significant energy savings, the nitride devices have to be pushed to their physical limit to meet the full predicted impact of their usage. In the following, we point out the relevant material properties of III-nitride materials and the challenges faced by the nitride technology.

1.1 III-nitride semiconductors

III-nitride semiconductors such as GaN, InN, AlN and their alloys, e.g., $In_xGa_{1-x}N$ or $In_xGa_yAl_{1-x-y}N$ exhibit unique material properties. Depending on their composition, their direct bandgap varies from about 0.7 eV corresponding to InN to 6.2 eV corresponding to AlN. The alloy bandgap thereby spans a wide wavelength range from the infrared over the visible spectrum to the deep ultraviolet (UV). Compared to other alloy compound semiconductors such as GaAs, which are grown in a zinc blend structure, cubic-like, III-nitride materials are commonly grown in wurtzite structure, hexagonal-like. The variation of bandgap of GaN, InN, AlN and their alloys as well as of other major semiconductors are shown in **Figure 1.1** along with the corresponding wavelength.

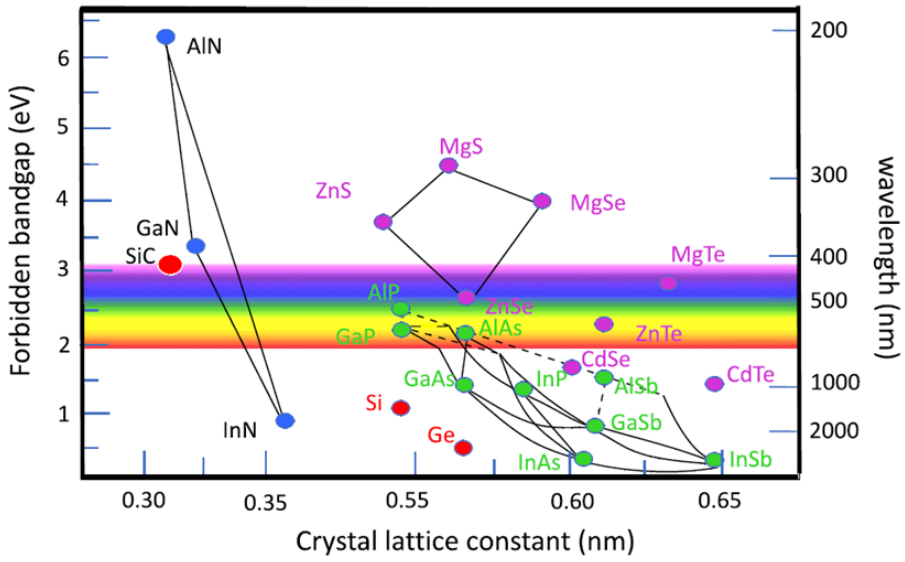

Figure 1.1: Direct bandgap of GaN, InN, AlN and their alloys depending on composition, and other major semiconductors and their alloys, against crystal lattice constant. Reprint from [6].

From **Figure 1.1** the application of nitride semiconductor compounds in opto-electronics is a logic consequence. However, the route that led to the fabrication of an InGaN/GaN LED with high-brightness in 1994 [10] was long and required tremendous research efforts and breakthroughs which culminated in the recognition by the Nobel Prize in Physics in 2014.

The light emission efficiency of LEDs is expressed by their *external quantum efficiency* (EQE). The EQE is the product of the *injection efficiency* (injected current into the active region which are the quantum wells (QWs) of an LED), *internal quantum efficiency* (conversion efficiency of injected

electron-hole pairs into photons inside the QWs), and the *light extraction efficiency* (ratio of photons emitted outside the LED to those generated inside) [7]. Multiplying the EQE by the *electrical efficiency* (the ratio of the electrical energy, mainly affected by ohmic or contact losses and quantum barrier heights in the active region, to the emitted photon energy), we obtain the *wall-plug efficiency* (WPE).
Unfortunately, a high WPE does not suffice. From 1994 to 2012 LEDs covered only a minor role until they became cost effective enough to penetrate the market [8]. State of the art blue-emitting LEDs reach a WPE of above 70% at low current densities [11]. However, there is prospect of operating LEDs at WPE ≥ 100% due to thermoelectric pumping of carriers by lattice heat [12].
The increased usage of LEDs shows already significant impact on the total consumption of electricity due to lighting [13].

The optoelectronic applications of III-nitrides are not only limited to lighting with LEDs and laser diodes (LD). For example, UV-LEDs are used for disinfection and water purification [14] and nitride based vertical-cavity surface-emitting lasers are used for fiber optic communication.

Besides these, nitride semiconductors also find wide-scale applications in power electronics. For example, in switching devices due to their ability to work at high switching frequencies [15].

Surprisingly, in view of the commercial success and application of nitride semiconductors, several challenges still need to be addressed to operate them at their physical limit. Tackling these remaining open questions is of great importance since immense energy savings are at stake. The challenges of III-nitrides will be explained in further details throughout this chapter.

1.2 Challenges of III-nitride semiconductors

1.2.1.1 Growth of III-nitride semiconductors

Due to the lack of a native substrate GaN heterostructures are grown on substrates with large lattice mismatch such as c-plane sapphire (Al_2O_3) or SiC. The defect density induced by strain due to this mismatch in the hetero-epitaxial growth is lowered by a first low-temperature grown, thin, seed layer followed by a thick GaN buffer layer. These layers greatly reduce dislocations and defect densities. However, there are still numerous threading dislocations ending in V-shaped pits on the surface with densities of 10^8 to 10^9 cm^{-2}. Such high defect densities usually diminish the performance of semiconductors. In III-nitride semiconductors, however, the role of threading dislocations has yet to find a widely accepted answer. Netzel et al. claimed in 2007 a universal relevance of V-shaped pit potential barriers around dislocations to prevent carriers to reach non-radiative centers in InGaN/GaN heterostructures and linked it to the high IQE [16]. This conclusion contradicts the finding of Cherns et al. in 2001 who identified the threading edge dislocations as non-radiative recombination centers [17]. Recently, Jiang et al. reported a breakthrough in the wall-plug efficiency of yellow LEDs via LEDs structures incorporating V-pits for improved carrier injection [18]. This finding underlines the claim by Netzel et al. that carriers are experiencing an energy barrier on their path to a non-radiative center due to thinned down QWs on the facets of V-pits from their slower growth in the c-direction [16].

Superlattices and underlayers below the active region lead to a general reduction of the defect density and impurities in III-nitride heterostructures [19]. The underlayer captures defects before they reach the InGaN QW which reduces the non-radiative recombination centers and therefore improves the efficiency [19,20].

The growth of nitride heterostructures on foreign substrates is, however, still a limiting factor on the efficiency of LEDs. A free standing GaN substrate would be lattice matched and induce a lower density of dislocations. In turn, it would reduce the strain effects in the heterostructure as well as dissipate heat more effectively [21]. The recent improvements in the growth of high-quality bulk GaN substrates by hydride vapor phase epitaxy (HVPE) made them commercially available [22]. LEDs such as bulk GaN based violet light-emitting diodes grown by Soraa Inc. exhibit a higher EQE and are, therefore, cost effective compared to LEDs grown on other substrates [23].

1.2.1.2 Conductivity of p-doped GaN

The basis for almost any opto-electronic device is the junction of p- and n-doped materials. One of the many breakthroughs to the final efficiently working LED was, therefore, a successful, efficient p-doping of GaN. The p-doping of GaN was first achieved by Amano and Akasaki with Mg acceptors being "activated" through e-beam irradiation [24]. In 1992, Nakamura achieved this by thermal annealing of Mg-doped GaN in an N_2 atmosphere [25], a much more practical technique. He also showed that the inactivity of Mg-doping was due to the presence of hydrogen atoms, originating from the decomposition of metal organic precursors, which passivate the Mg acceptors[4]. However, p-GaN still has a poor conductivity because of the deep acceptor levels with large activation energies of about ~170 meV of the Mg-doping [26] which leads to ~1% fraction of acceptors being ionized at room temperature and yielding a hole. Hence, the p-GaN exhibits an insufficient electrical conductivity which in turn induces poor current spreading and current crowding effects impacting the light extraction efficiency of LEDs [7,27]. Transparent ITO current spreading layers acting as top electrodes or sophisticated electrode designs on the p-GaN top LED layer have, however, led to a recovery of the loss in efficiency [27,28].

1.2.1.3 Polarization effects

The commonly used growth axis of [0001] on c-plane of III-nitride semiconductors induces built-in electric fields due to spontaneous and piezoelectric polarizations. These effects are large compared to other semiconductors such as GaAs and GaP. However, these effects are well studied and understood. Due to the polarization-induced internal electric field, the emission spectrum exhibits a red-shift as QW electron and holes separate under such fields. This effect is known as quantum confined Stark effect (QCSE) [29]. The accumulation of carriers in the QW under increasing optical or electrical injection screens the internal electric field and results in a blue-shift of the emission [29]. The polarization effects, however, have no direct effect on the internal quantum efficiency (IQE) at low injection since both radiative and non-radiative recombination are affected likewise [7]. These fields impact the IQE only indirectly, due to an increase in the carrier lifetime. However, in the absence of these fields the phenomenon of droop in efficiency appears at lower current density due to a faster accumulation of carriers in the active region [30].

1.2.1.4 Carrier recombination in III-nitride

To describe the recombination dynamics and efficiency of LEDs a simple polynomial fit of experimental data to three parameters A, B, and C is commonly used. In this so-called ABC-model,

[4] Let us remark that, as hydrogen is absent in MBE growth, the annealing step is not required. However, in spite of huge efforts, MBE materials still have poorer opto-electronic properties than MOCVD ones.

A stands for the non-radiative Shockley–Read–Hall coefficient, B for the radiative recombination coefficient, and C for the non-radiative Auger contributions. The effects associated with A, B and C are shown in **Figure 1.2**.

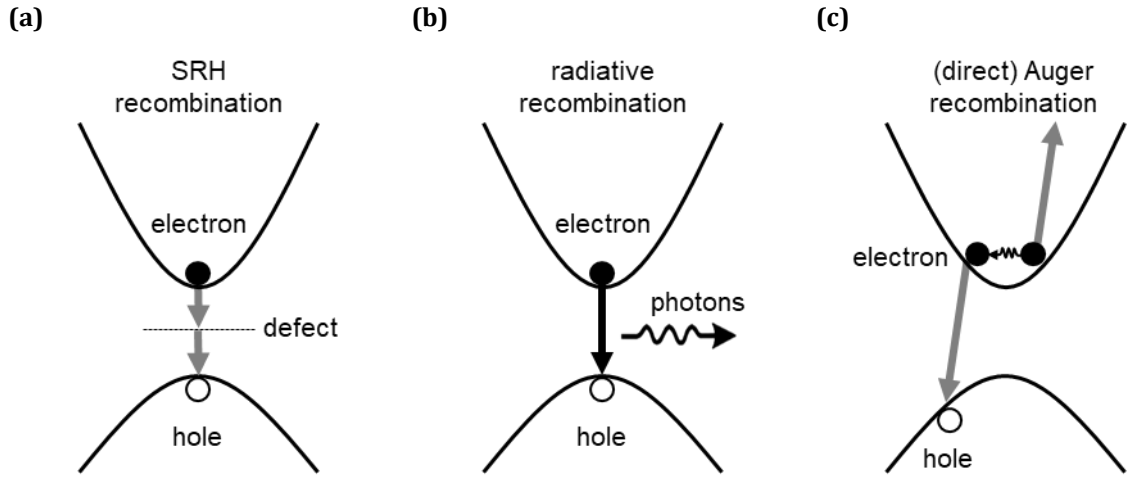

Figure 1.2: Recombination processes **(a)** non-radiative SRH effect, **(b)** radiative recombination, **(c)** non-radiative Auger effect (direct).

Although the physics behind these parameters is complex, the "droop" of IQE, i.e., the decrease of IQE arising at high-current densities, is captured in the n^3 term of the IQE formula:

$$\mathrm{IQE} = \frac{Bn^2}{An + Bn^2 + Cn^3},$$

where *n* is the carrier density [8,30].

The operation of LEDs at high current densities while retaining a high IQE is, however, a prerequisite to lower lamp costs because of the direct correlation between luminaire cost and semiconductor real estate area [8]. Therefore, vast efforts have been made to understand this non-linear behavior. Shen et al. argued in 2007 that the droop in efficiency originates from the Auger effect and is, hence, caused by an intrinsic material property. After years of controversial discussions (see C. Weisbuch [7] for a detailed review), it is now well-established that the Auger recombination is the main cause of the droop. It was first experimentally proven in [31].

1.2.1.5 Green gap

Another major and still unsolved challenge of nitride LEDs is their decreasing efficiency at increasing emission wavelength obtained by increased In concentration in their active region. This gives rise to the so-called "green gap" as other III-V materials systems provide efficient red emitting LEDs. Currently, to obtain white light emission high-efficient blue LEDs are down-converted with a phosphor coating. However, the down-conversion induces a loss in efficiency. Therefore, to fully exploit the physical limit of efficient LED lighting, white light generation through color-mixing of highly efficient blue, green and red LEDs is needed. The white lamp efficiency by employing high efficient blue, green and red LEDs via color-mixing is expected to reach 325 lm/W compared to only 250 lm/W for white lamps via phosphor-converting [9]. Up to now, we have only understood that random alloy fluctuations play an important role in green LEDs which connects the green-gap to intrinsic material properties [32]. However, even simulations which take into account alloy fluctuations and their effects cannot account for the high

turn-on voltage and the discrepancy between the expected and experimental emission wavelengths (shifted by about 30 nm from each other) for a typical In content of 24%.

1.3 Compositional disorder in nitride alloys

As mentioned above, the bandgap of visible nitride LEDs requires the use of ternary alloys with emission wavelengths that depend on the composition. Those nitride ternary alloys are, however, affected by alloy disorder. This compositional disorder induces fluctuations in the local bandgap and, hence, in the potential seen by carriers on a nanometer-scale which leads to localization effects. These localization effects might impact the operation and performances of III-nitride devices [33]. In detail, the efficiency droop due to Auger recombination has been linked to alloy disorder because of the absence of droop in PL measurements on pure GaN QWs [34,35]. As already mentioned, alloy fluctuations have also been shown to play an important role in the operation of green LEDs. It is therefore of primary importance to evaluate the impact of alloy disorder on III-N compounds and devices.

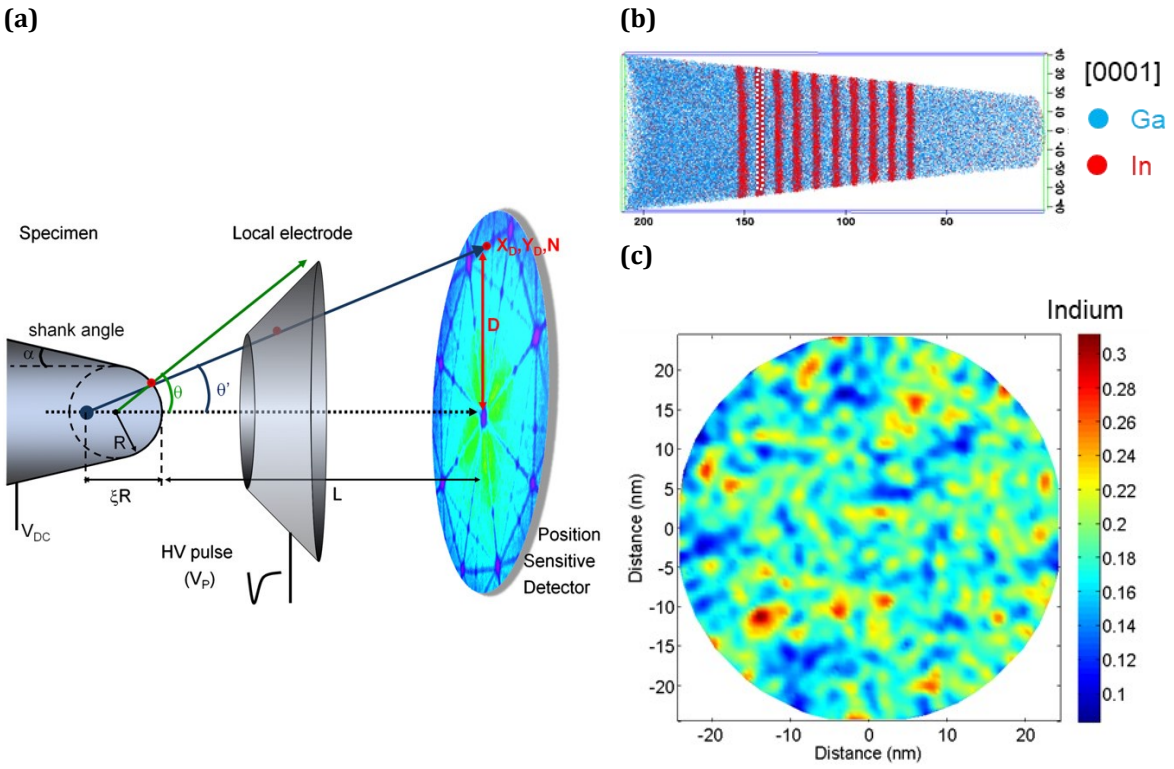

Figure 1.3: (a) Schematics of APT measurement, reprint from [36]. APT results of a multi-QW InGaN/GaN heterostructure giving an average In concentration of 17.98%: **(b)** APT specimen, **(c)** derived In concentration of marked QW. By courtesy of B. Bonef (see also [37]).

Experimentally, the compositional disorder of III-nitrides can be observed, for example, by atom probe tomography (APT). APT is a destructive microscopy method. It uses a high-power laser pulse (or high voltage pulse) to extract ionized atoms out of a specimen under an accelerating electric field. The projection of the ionized atoms on a screen provides their in-plane position. Based on the time-of-flight of the ions, their mass is determined, thus their chemical nature. Progressive erosion of the sample allows the 3D reconstruction of the specimen composition. A

schematic illustrating the working principle of APT including the specimen, the path of ions in the electric field, and the position sensitive detection is shown in **Figure 1.3 (a)**. An example of an APT measurement is illustrated in **Figure 1.3 (b)** and **(c)**. These APT results are taken on an InGaN/GaN heterostructure with the same concentration of In as the samples which will be discussed in **Chapter 3 Results**.

1.4 Disorder-induced localization effects

Accounting for the alloy fluctuations observed in III-nitride semiconductors and devices is a tremendous challenge from the theoretical standpoint. Due to the disorder manifesting at the atomic scale, usual models for semiconductors such as virtual crystal approximation, used for example in III-V alloys [38], or the plane Bloch wavefunctions approximation fail. Commonly, such disordered potential requires solving the Schrödinger equation for both electrons and holes to determine the energies and spatial structure of the localized quantum states. Such computations are, however, extremely demanding, if not impossible for realistic 3D LED structures.

In 2012, Filoche and Mayboroda introduced a theory to account for localization properties in random mathematical potentials and their resulting confining regions [39]. Their approach allows to estimate the energy and wavefunction shape of eigenmodes in random potentials without the need of solving the Schrödinger equation. In this so-called Filoche-Mayboroda localization landscape (LL) theory instead of solving the eigenvalue problem of the Schrödinger equation,

$$H\psi = E\psi$$

(with the Hamiltonian H and the wavefunction ψ), the much simpler Dirichlet problem:

$$Hu = 1$$

gets solved. The solution $u(\mathbf{r})$ of this equation is the so-called localization function [39]. Filoche and Mayboroda showed that low-energy eigenfunctions are localized inside the regions enclosed by the valley lines of $u(\mathbf{r})$ [39]. Moreover, an effective confining potential $W = \frac{1}{u}$ can be derived.

The crest or watershed lines of W corresponds to the valleys of $u(\mathbf{r})$ and act as barriers to the wavefunction ψ [39,40]. The application of the LL theory to nitride semiconductors in a self-consistent approach that solves Poisson, drift-diffusion equations and the landscape function has enabled the study of their quantum disorder and carrier dynamics [40–42]. The LL theory accounts well (due to the calculation of the overlap between conduction and valence bands) for the experimentally observed sub-bandgap absorption tail characteristic of alloy disorder. Even realistic 3D LED devices can now be simulated since LL theory reduces the computation time by multiple orders of magnitude compared to a direct solution of the Schrödinger equation [40–42].

Taking the randomness evidenced by APT measurements (see above), the effective confining potential with *localization regions* of about 5 nm size in III-nitride alloys is derived from the LL theory. **Figure 1.4** shows the effective confining potential derived from the alloy disorder seen by electrons of an InGaN structure with an In content of 18%. These values are comparable to those of the samples discussed in **Chapter 3 Results.**

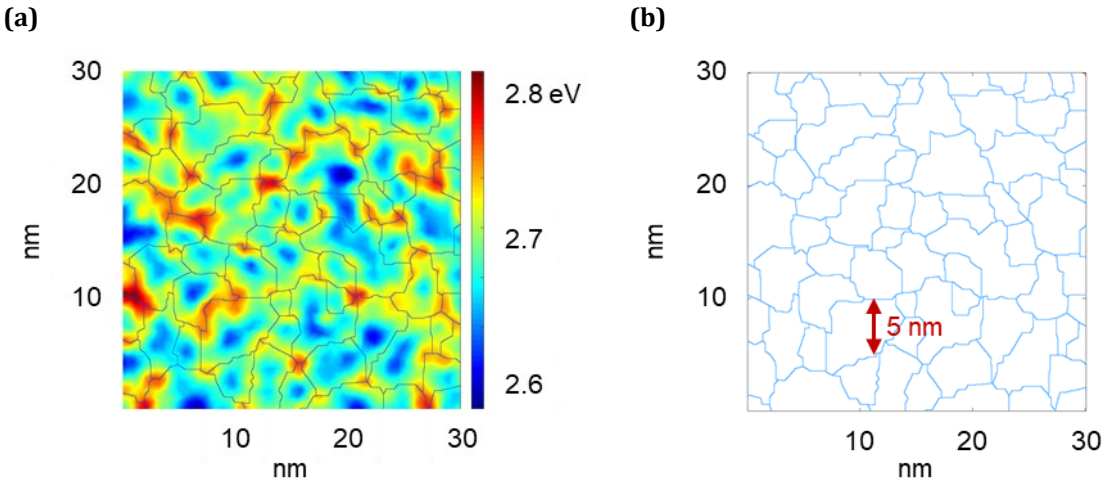

Figure 1.4: (a) Calculated 30 nm × 30 nm map of the localization function 1/u, the effective confining potential, for the electrons in the center plane of an InGaN QW of 18% average In concentration. The blue lines indicate the crest lines which delimit the localization regions. **(b)** Only crest lines obtained from **(a)**. By courtesy of J.-M. Lentali (see also [43,44]).

The experimental challenge is to probe these localization regions at the appropriate scale to study the disorder-induced localization effects and their influence on carrier dynamics.

1.5 Experimental evidence of disorder-induced localization effects

Several attempts have been made to experimentally investigate the effect of compositional disorder. By confocal microscopy [45], scanning near-field optical microscopy [46,47], and cathodoluminescence microscopy [48–50], spatial variation of the emission intensities and/or emission energies were observed. The size of the emitting domains probed in these studies was either in the micron or submicron (typically 100 nm) range. At room temperature line widths broader than 100 meV with moderate energy shifts were detected from these rather large-scale spatial fluctuations. However, these types of fluctuations are commonly associated with extrinsic growth inhomogeneities related, for example, to terraces separated by bi-atomic steps which can be evidenced by atomic force microscopy.

In contrast, the modeling of the random atom positioning in the nitride ternary alloy observed by APT (see section **1.3**), predicts that the compositional disorder induces Anderson-like localization in regions of a few nanometer size [32,40–42,51–53]. The emission from these localized states is expected to be as narrow as emission from single III-nitride quantum dots [54]. This conclusion should remain valid at room temperature. To underline the discrepancy between the measurements that have been performed so far and the theoretical predictions, we show the results of Suman et al. [55] in **Figure 1.5**. We perform a zoom on the original spectrally resolved photoluminescence microscopy map first to a scale of 500 nm × 500 nm in **Figure 1.5 (b)** and then to the scale of 30 nm × 30 nm in **Figure 1.5 (c)**. The latter scale corresponds to the domain of the effective confining potential simulated by LL theory shown in **Figure 1.4**.

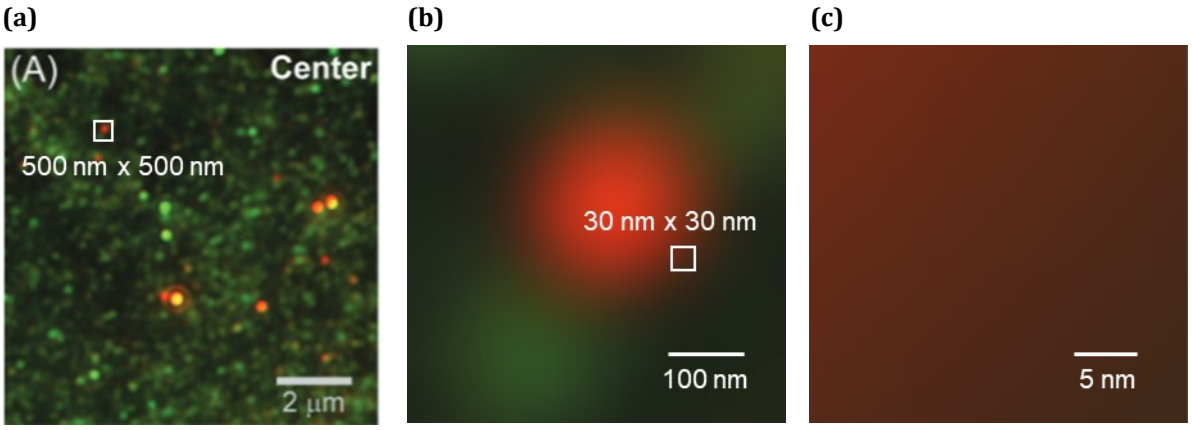

Figure 1.5: Spectrally resolved photoluminescence microscopy on InGaN GaN QW. Gradual zoom into marked area from original size in **(a)** to 500 nm × 500 nm in **(b)** to 30 nm × 30 nm in **(c)**. Reprint from [55].

It is clear from **Figure 1.5** that a microscopy technique with much higher resolution is needed to probe the disorder-induced localization effects at the characteristic scale of 5 nm.

In 1991, Renaud and Alvarado introduced scanning tunneling microscopy-excited luminescence with nanometer resolution on III-V heterostructures [56,57]. This technique is referred to as scanning tunneling electroluminescence (STL) in the present work. It uses the tip of a scanning tunneling microscope (STM) as a source of electrons to inject carriers in a semiconductor sample. The emitted light resulting from the radiative recombination of the injected carriers is then detected. **Figure 1.6** shows a schematic of the STL working principle.

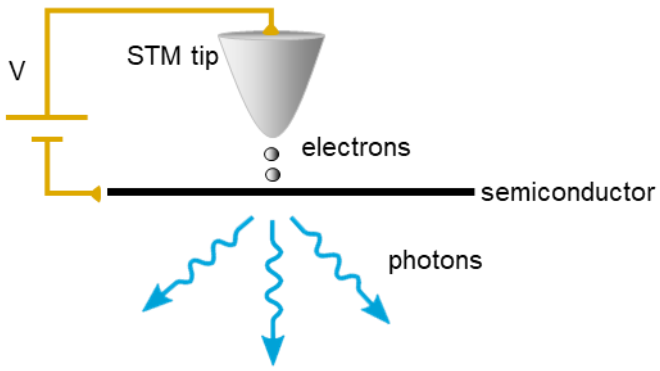

Figure 1.6: Schematic of the working principle of STL. STM tip in proximity of the surface with tunneling current flowing between tip and sample exciting luminescence in the semiconductor.

Renaud and Alvarado used this local luminescence technique to study the band bending profile and the conduction band discontinuities at the interfaces within p-doped $Al_xGa_{1-x}As/GaAs$ heterostructures [57]. They describe STL in a three-step model [57]:

1) tunneling injection of carriers from the STM tip to the sample surface,
2) carrier transport in the semiconductor,
3) radiative carrier recombination.

The first step of this process is comparable to the description for standard STM. However, band-to-band radiative recombination of the injected carriers requires the presence of the counter charge. When injecting electrons from the tip to the semiconductor, p-doped samples have to be used. Band-to-band radiative recombination can only occur beyond the band bending region that forms near the surface. The applied bias voltage has to account for the electron being injected into the conduction band and transmitted beyond the surface depletion region. This requirement sets the bias voltage threshold V_{th} of luminescence onset to $eV_{th} > E_C$, with E_C being the energy of the bottom of the conduction band in the bulk referred to the Fermi level. Comparable to the current transmitted through the metal layer in ballistic electron emission microscopy (BEEM) experiments, the integrated luminescence intensity follows a quadratic dependence on the applied bias voltage. Considering energy and momentum conservation parallel to the surface, an injection cone for the electrons crossing the depletion region to reach the bulk is described by [57]:

$$sin^2\Theta_c = \frac{m^*(eV_{th} - E_C)}{m^*(\delta + eV_{th} - E_C)} \times \frac{eV_{th} - E_C}{\delta + eV_{th} - E_C}.$$

The energy dependent effective mass $m^*(E)$ of the electrons accounts for the non-parabolicity of the band. The amplitude of the downward band bending is δ. Outside this injection cone, electrons are reflected or trapped in the band bending region, leading to the nanometer resolution of STL. Using STL, Renaud and Alvarado achieved nanometer resolution in their measurements of the conduction band profiles on $Al_xGa_{1-x}As$/GaAs heterostructures [57].

The application of STL has led to astonishing results from exciton trapping at localized defect states in organic semiconductors [58,59] and resonant energy transfer from the tunneling current to the excitons in 2D materials [60], to the evidence of photon emission in the visible range from quantum confined states in porous Silicon [61]. In nitride semiconductor heterostructures, Evoy et al. [62] and Manson-Smith et al. [63] applied STL to study the effect of defects on recombination. Their samples consisted of thick injection layers (respectively 100 nm in [62] and 200 nm in [63]) and a series of QWs in the active region in [62] and single QW capped by a GaN/AlGaN barrier in [63]. For a series of QWs, the emission spectra from the different QWs overlap each other leading to a summed signal. The single QW (SQW) used in [63] was buried 200 nm away from the surface, which broadened the injection cone of carriers and, therefore, leading to a summation of the emission from many localization regions. Hence, in both cases it was not possible to resolve the emission from single localized states.

We, therefore, propose to use a near-surface single GaN/InGaN/GaN QW to study localization effects induced by alloy disorder. Our experimental approach will be explained in detail in **Chapter 2 Experimental Method**, while the results gained on nitride semiconductors will be discussed in **Chapter 3 Results**.

2 Experimental method

In this chapter, we recall the basics of scanning tunneling microscopy and of scanning tunneling electroluminescence, which is a later development of the first. The experimental setups and the measuring procedures that we developed are described in detail.

2.1 Techniques

2.1.1 Scanning tunneling microscopy[5]

Scanning tunneling microscopy (STM) is a well-established surface sensitive local probe technique. For its invention Gerd Binnig and Heinrich Rohrer were awarded with the Nobel Prize in Physics in 1986 [64]. STM excels for the ability to probe the electronic density of states down to the atomic scale. Its application enabled surface imaging with atomic resolution, atom manipulation, spectroscopy of the local density of states of surfaces and materials, as well as many other advancements in condensed matter physics.

STM is based on quantum mechanical tunneling through a barrier. **Figure 2.1** offers a standard representation of tunneling through a potential barrier, e.g., vacuum or insulating layer, separating two conducting solids. When a bias voltage between the two materials is applied, a tunneling current flows through the barrier resulting from the overlap of the exponential tails of the electron wavefunctions on both side of the barrier.

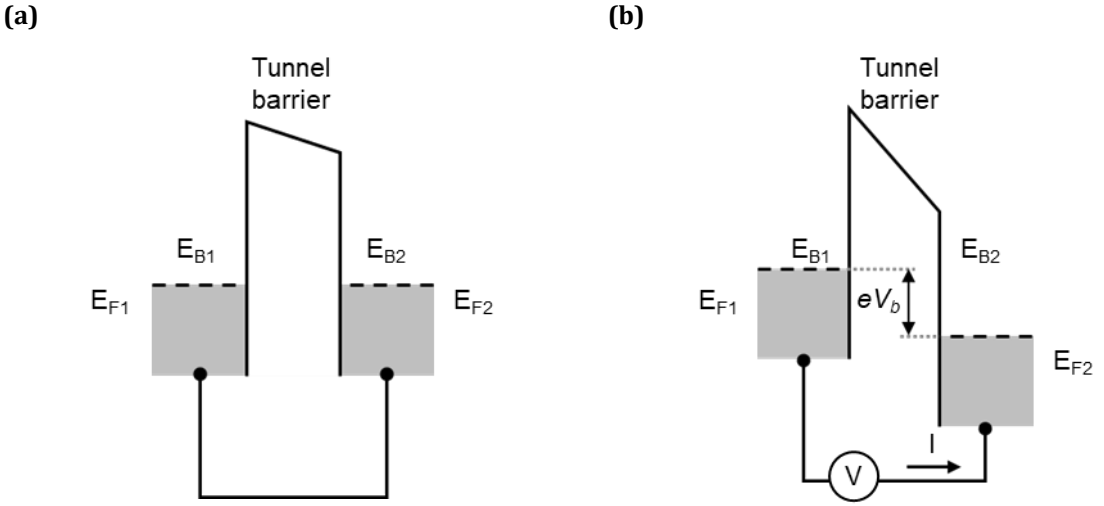

Figure 2.1: Tunneling through a barrier between two conducting solids with different work function. **(a)** Without applied bias voltage and **(b)** with applied bias voltage.

In the highly simplified case, the solution of the Schrödinger equation inside the barrier is:

[5] This is a short introduction to scanning tunneling microscopy. For more details, refer to the literature e.g. Dawn A. Bonnell, Scanning Probe Microscopy and Spectroscopy (Theory, Techniques, and Applications) [65] or C. Julian Chen, Introduction to Scanning Tunneling Microscopy [67].

$$\psi(z) = \psi(0)e^{-\kappa z} \qquad \text{with} \qquad \kappa = \frac{\sqrt{2m(V_b - E)}}{\hbar},$$

where V_b is the potential applied between the two sides of the barrier, E and m are respectively the electron's energy and mass.

The current I of the electrons tunneling through the barrier decays exponentially with the barrier thickness z:

$$\mathrm{I} \propto e^{-2\kappa z}.$$

In an STM, the conducting material on one side of the barrier is an atomically sharp metallic tip commonly made out of Pt-Ir or W. The other side is the sample surface which is to be measured. Between the sample and the tip, a bias voltage is applied. The STM tip is brought in proximity of the sample surface, so that the overlap of their wave functions results in a tunneling current flow. The tunneling current is:

$$\mathrm{I} = \mathrm{C}\rho_t\rho_s e^{z\cdot k^{1/2}},$$

for small voltages (V << work function of the material), with C a constant, and ρ_t and ρ_s being the density of states of the tip and of the surface, respectively [65]. **Figure 2.2** illustrates a schematic of the working principle of an STM with the tunneling current flowing between the apex of the tip and one atom on the sample surface (highlighted in blue).

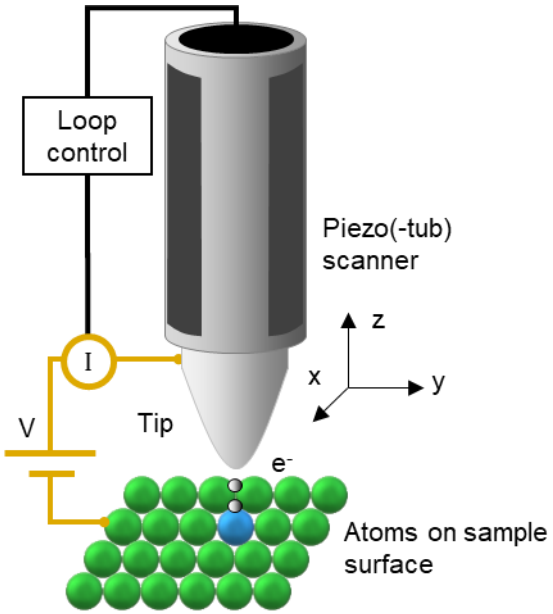

Figure 2.2: Schematic of the working principle of an STM. A bias voltage is applied between the tip and the sample. The STM tip is moved by piezo scanner. A feedback loop controls the tip-sample distance. The tip z-motion is recorded as a function of the tip position in the xy-scanning plane allowing for the surface topography measurement with atomic resolution.

The position and motion of the tip in the three spatial directions x, y and z are controlled via piezo-electric devices (piezo scanners). The distance between the STM tip and the sample surface is controlled by a feedback loop with gain control. The feedback loop allows to adjusts the tip-to-sample distance to ensure a constant tunneling current ("constant current"-mode) or if it is switched off to keep an initial absolute tip altitude constant (the current and tip-to-sample distance while scanning thus varies). The latter is called "constant height"-mode. In the "constant

current"-mode, when scanning the tip over the surface, the tip motion maps the iso-joint density of states of the material's surface. A second and larger set of piezo scanners enables movements to adjust the global xy-position of the tip on the sample (not shown in schematic).

2.1.2 Scanning tunneling electroluminescence

From the invention of STM, a large variety of scanning probe techniques have emerged. For example, atomic force microscopy, Kelvin probe force microscopy, scanning near-field optical microscopy, ballistic electron emission microscopy, and STL.

As already mentioned, STL consists of using the tip of an STM as a local source of electrons to inject carriers in a semiconductor and detecting the light emission resulting from the carrier recombination in the material.

Our goal is to study localization effects induced by alloy disorder in a near-surface $In_xGa_{1-x}N$/GaN QW by STL. Due to the local nature of the tunneling injection, we assume that electrons reaching the QW populate a limited number of the disorder-induced localization regions [43], as schematized in **Figure 2.3**. In these conditions, it is expected to obtain a signature of the emission from the different localized states by measuring the electroluminescence spectrum as a function of the tip position.

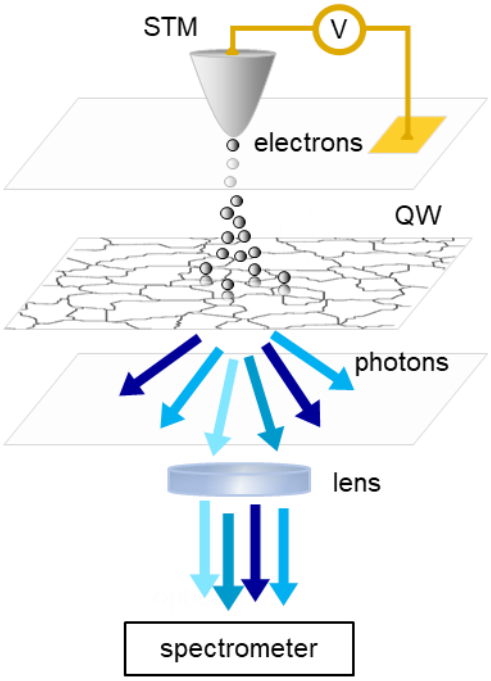

Figure 2.3: Schematics of STL measurement in InGaN/GaN heterostructures. The bias is applied between the tip and a gold pad on the sample surface to inject carriers in the semiconductor heterostructure and excite radiative recombination from the disordered QW. Contours of the localization regions calculated by the localization landscape theory are sketched in the QW plane.

2.2 Experimental setups

2.2.1 STL in ambient atmosphere

Our experimental setup in ambient atmosphere is based on an Omicron CRYOSXM with significant adaptations. These adaptations are implemented on the mechanics of the STM head, on the control and acquisition electronics, and on the software (partly performed and shown in [66]). The

Omicron CRYOSXM is inserted into an Oxford flow cryostat (Optistat SXM Bath) enabling STM measurements down to liquid helium temperature. The whole system is suspended inside a box shielded from acoustic noise and mechanical vibrations. A picture of this setup is shown in **Figure 2.4**.

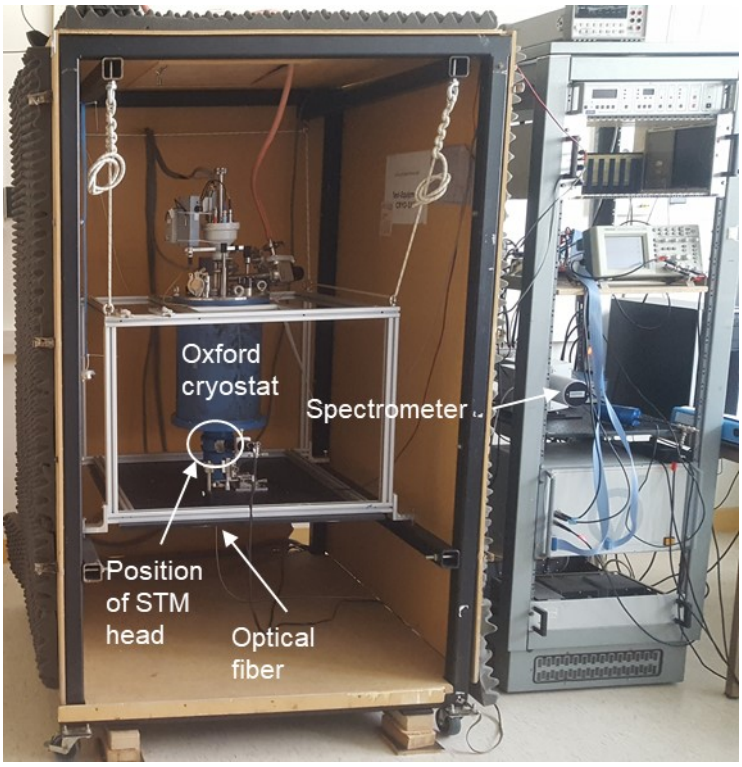

Figure 2.4: Omicron CRYOSXM STL in ambient conditions (air) setup free swinging inside the isolation box with homemade adaptions and spectrometer on the right-hand side.

In the original setup, the tip was fixed and pointed upwards while the sample was carried by the scanner with the sample surface to be studied facing the ground. To collect the emitted luminescence with a large aperture through the window at the bottom of the cryostat, we exchanged the position of the tip and the sample. The sample is now in a fixed position while the STM tip scans over the surface. The transparent nature of the samples (we are studying the emission of an InGaN QW inside a GaN structure grown on sapphire) enables to work in a *transmission geometry*. A sample holder has been designed with an inserted optical lens of short focal length (4 mm) and large numerical aperture of 0.6 (Thorlabs C610TME-A). A photo of the sample holder with the lens and contact pads is shown in **Figure 2.5 (a)**. **Figure 2.5 (b)** displays the sample holder with a contacted sample and the STM tip in close proximity of the surface.

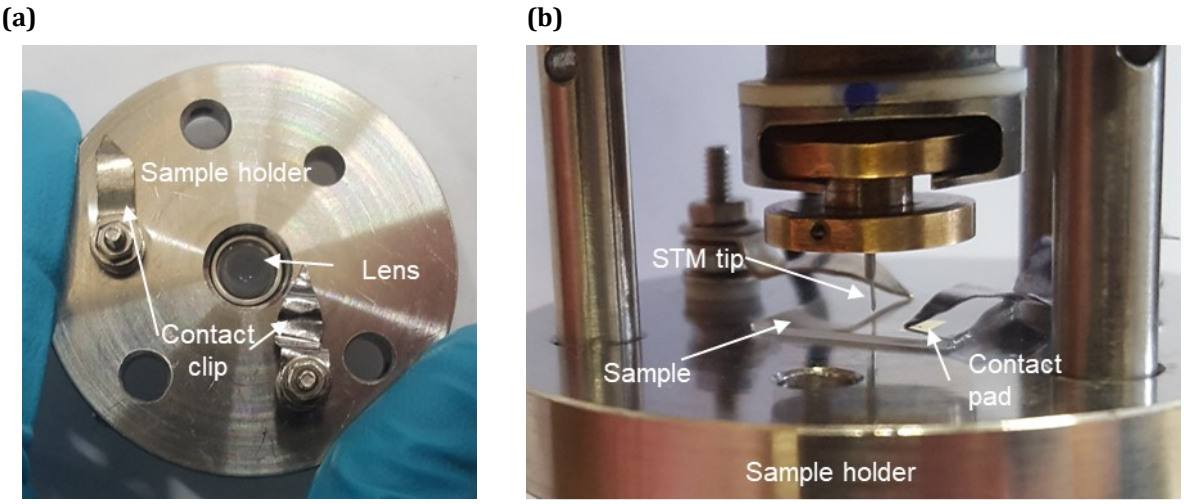

Figure 2.5: (a) Homemade sample holder containing a collecting lens with short focal length and contact clips. **(b)** sample placed on its holder and contacted via contact clips with STM tip close proximity to its surface.

The luminescence from the sample is collimated by the lens inside the sample holder. The lens-to-sample distance can be optimized with respect to the sample thickness. The emitted light is transmitted through the window at the bottom of the cryostat and focused via an achromatic 10 mm diameter lens with 0.24 NA (Thorlabs AC060-010-A-NL) at the entrance of an optical fiber (Thorlabs, M114L02) with 0.22 NA and 600 µm core diameter. The optical fiber guides the light to the entrance slits of the spectrometer. **Figure 2.6** shows a complete schematic of our STL setup.

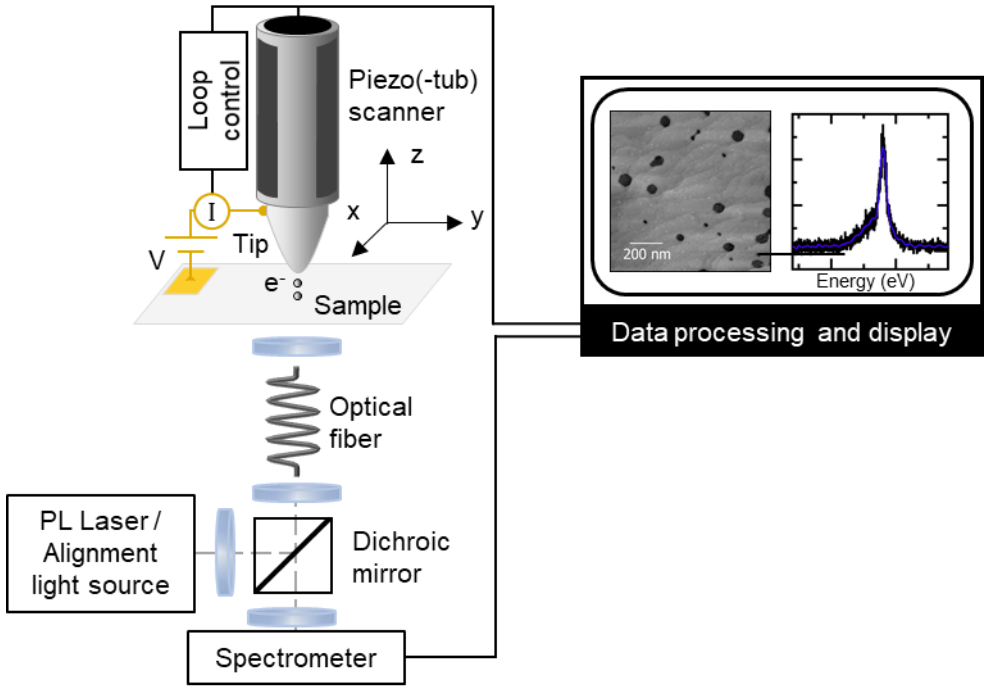

Figure 2.6: Schematic of our complete STL setup in ambient atmosphere, including the photoluminescence/alignment line and data processing.

We used two different spectrometers in our STL setup based on the Omicron CRYOSXM. The results at low tunneling currents of 2 nA presented in Chapter 3.2.3 were performed with a

Princeton Instruments IsoPlane SCT 320 spectrometer equipped with a 2D silicon detector. The resolution of this setup with fully opened slits is 35 meV. Starting from Chapter 3.3.2 (measurements at high tunneling current of 20 nA), we used a Horiba MicroHR Imaging Spectrometer with a Synapse EMCCD optimized for the UV to visible range. The slits of the spectrometers are closed to 600 µm giving a final resolution of 26 meV for the monochromator. The collection efficiency of the extracted light at the exit of the fiber is ~ 0.7%.

A typical topography measurement of a GaN surface (see **3.1.1.** for sample details) recorded with this STM setup is shown in **Figure 2.7**, along with a surface profile showing terraces separated by bi- and mono-atomic steps [43].

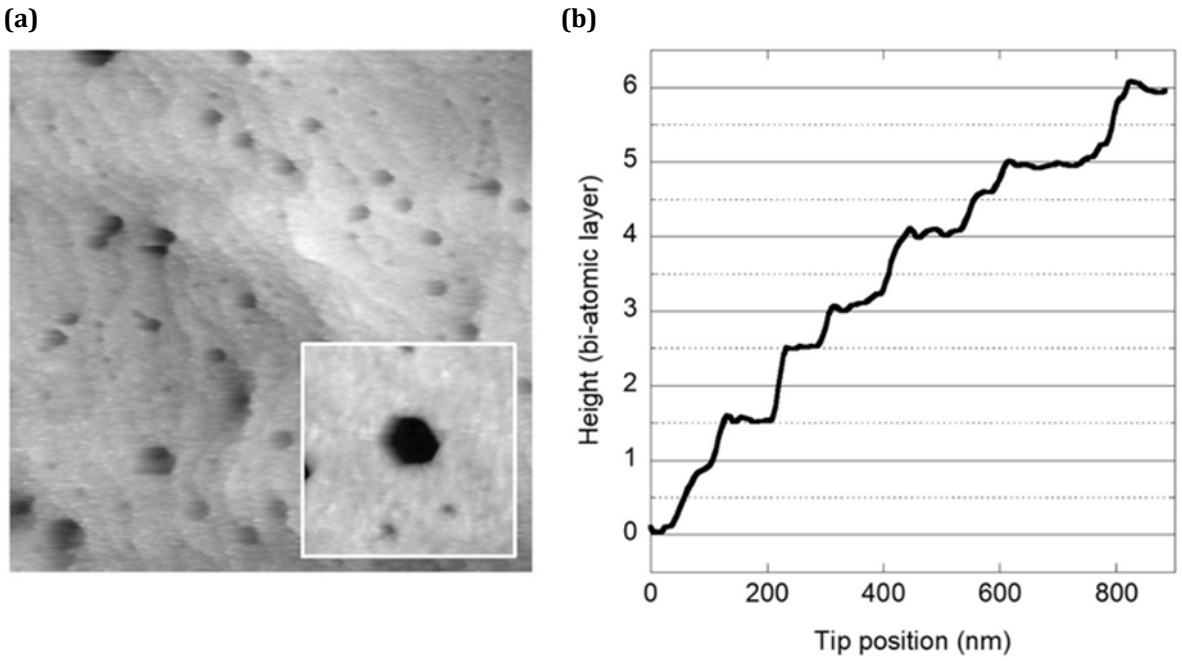

Figure 2.7: (a) 2.5 µm × 2.5 µm STM topography of a GaN surface. The inset shows a zoom on a 0.5 µm × 0.5 µm area around a hexagonal etch pit. **(b)** Surface profile showing terraces separated by bi- and mono-atomic steps [43].

2.2.2 STL in ultra-high vacuum

As we will see in detail in **Chapter 3 Results**, the Omicron CRYOSXM STM under ambient conditions was a suitable first candidate to study the disorder-induced localization effects in nitride semiconductors. Its operation in air makes it easy to access and manipulate the sample as well as the STM tip. However, operating an STM in air brings the disadvantage of surface contaminations. For example, the natural water film on the sample surface which could cause electro-chemical reactions (such as the formation of an oxide layer on the sample surface [66]) due to high current densities and high tunneling bias voltage necessary for STL measurements on nitrides. Operating the STL experiment under ultra-high vacuum (UHV) conditions would provide a better control of the surface and allow to extend the STL approach to other issues in semiconductor physics. This scenario is further discussed in **Chapter 5 Conclusion and perspectives.**

Consequently, we designed a new STL setup operating in UHV. The key figures for this experiment were set by the experience gained on the Omicron CRYOSXM setup. The light collection in transmission geometry provides a large aperture and high efficiency of the collection optics and leaves the space around the tip free. Therefore, we desire to keep the same geometry which led to

a small choice of commercially available STMs. Additionally, to the UHV condition and the light collection, the new STM setup should enable to perform temperature dependent measurements (cooling and heating) to study transport effects. Moreover, an optical access from the top to perform additional in-situ characterizations, and to improve the tip quality by in-situ sharpening techniques is necessary. Besides the hardware components, the software to drive this STM plays a considerable role since it needs to be adapted to the STL measurement procedure and synchronized with the spectroscopy setup.

Considering all the requirements above, we opted for the RHK Technology's UHV 300 Variable Temperature Ultra-High Vacuum Scanning Tunneling Microscope (VT UHV STM) with R9 electronics and customized adaptations. The sample holders in the RHK Beetle System naturally have an optical access from their backside and are, hence, well adapted for STL measurements in transmission geometry. Few adaptations still had to be carried out. First, a wider opening in the baseplate of the sample holder was drilled to allow a light collection with a larger aperture. Second, the pumping well below the chamber was removed and replaced by a view port which provides the optical access from outside the chamber to the back of the sample. Since the chamber was initially held by the pumping well, a specific fixation of the chamber to the floating support table was designed and the ion pump was mounted on a side free flange. Third, an optical breadboard was added below the chamber to fix the optical system for luminescence injection in the optical fiber. The final STL chamber is shown in the pictures of **Figure 2.8**. After baking the chamber, a base pressure of 3×10^{-10} mbar is currently reached.

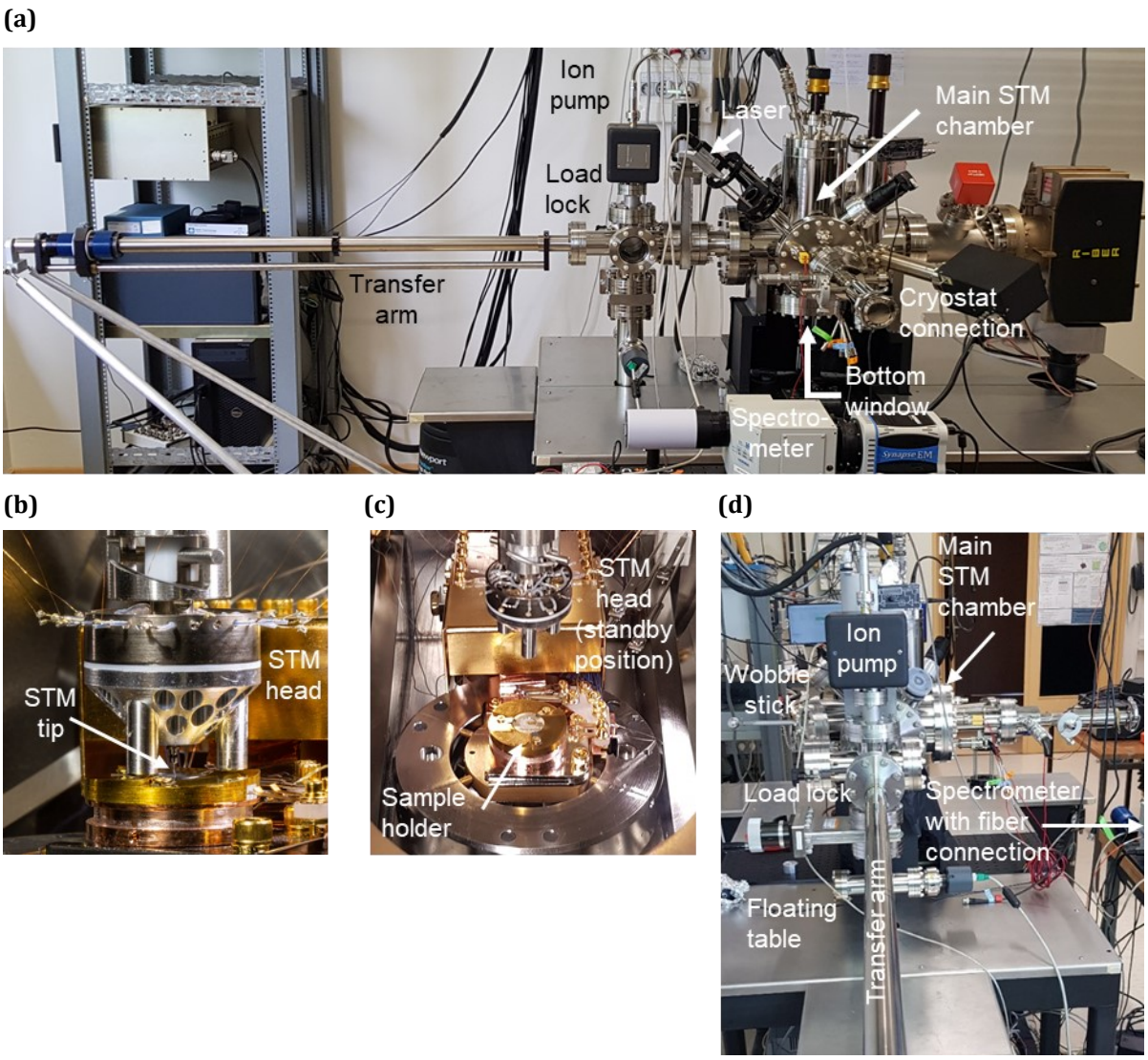

Figure 2.8: Pictures of customized RHK Technology's UHV 300 Variable Temperature Ultra-High Vacuum Scanning Tunneling Microscope, **(a)** view from the cryostat connection side on the main STM chamber, **(b)** STM head in scanning position on the sample holder inside the main chamber, **(c)** view on the STM head in standby position inside the main chamber, **(d)** view from the transfer line on the main chamber.

For the optical collection, we designed a lens support which fixes a lens inside the UHV system behind the sample with the option to add a screen to shade the lens during sample annealing at a later stage. **Figure 2.9** presents a cut through the technical drawing of the chamber showing the optical collection line and position of the lens as well as the final mounted result. For the light collection we chose an aspheric lens with an effective focal length of f_{eff} = 50 mm and 0.5 NA. This configuration enables us to focus the divergent emission from the sample directly to the entrance of an optical fiber outside the chamber. The position of the optical fiber outside the chamber can be adjusted in xyz-position to optimize the alignment.

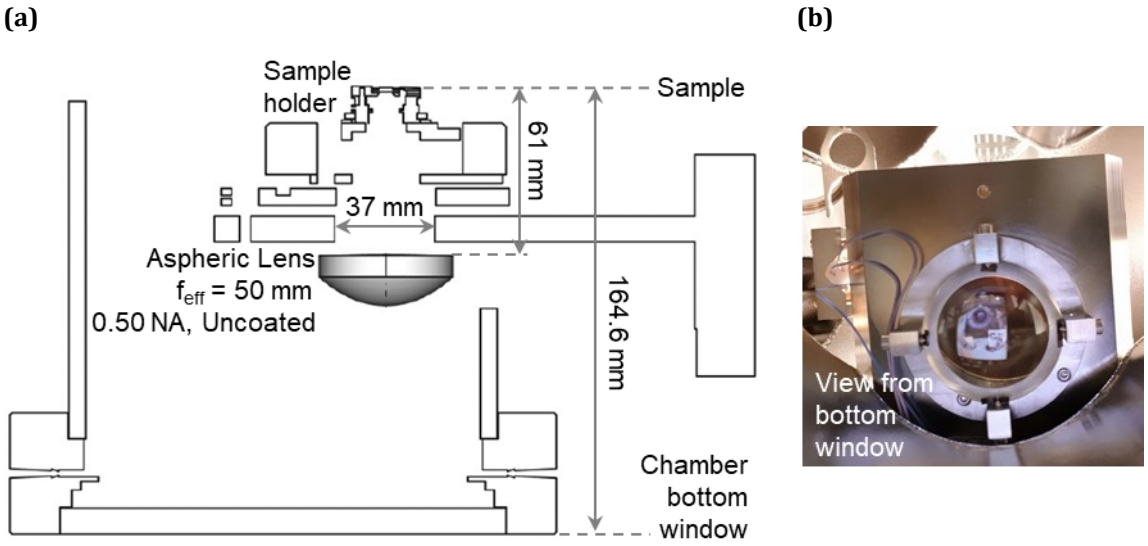

Figure 2.9: (a) Cut through the technical drawing of the STL chamber showing the optical access as well as lens and lens position. **(b)** Picture of the final mount of the lens inside the STL chamber as seen from the bottom window.

In addition, we designed an adaptation for a laser from one of the top window flanges of the STL chamber, as shown in **Figure 2.10 (a)**. The laser beam is focused on the sample surface in the area where the tip operates [**Figure 2.10 (b)**]. The photoluminescence spectrum is detected in transmission and optimized by adjusting the optical fiber position. The laser is incident on the sample surface with an angle of ~40° to minimize the collection of laser stray light in the fiber.

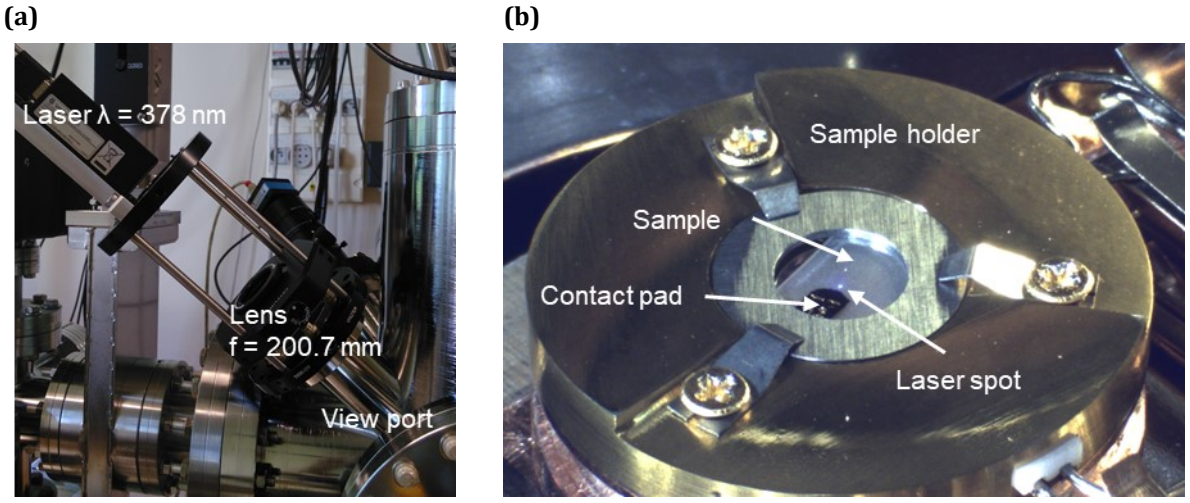

Figure 2.10: (a) Adaptation for in-situ photoluminescence characterization: focused laser light is injected through a view port onto the sample. **(b)** Focused laser spot on sample.

We will draw a comparison between the STL setup in ambient atmosphere and the STL setup under ultra-high vacuum in **Appendix B**.

2.3 Experimental procedure

2.3.1 STM tips

Preparing STM tips is commonly done by either a cut-and-pull technique or electrochemical etching. Both these techniques can be combined with further processing techniques to improve the tip's quality. The metals typically used are W, which is processed by electrochemical etching, or alloys such as Pt-Ir, which allow tip fabrication both by the cut-and-pull technique or electrochemical etching. W tips are affected by surface oxidation which makes them unusable after time when running STM experiment in ambient air. Pt-Ir is less affected by the formation of an oxide on its surface which makes it the preferred choice if working in ambient conditions. In the work at hand, we used only Pt-Ir tips obtained by the cut-and-pull technique from a 0.25 mm diameter wire. The cut-and-pull technique to make STM tips will be explained in the following.

As the name suggests, the cut-and-pull technique is based on a combination of cutting and pulling at the same time. The Pt-Ir wire is partially cut with a wire cutter. Simultaneously, the wire itself is pulled in opposite direction with a flat nose plier until the wire splits apart. This process is illustrated in **Figure 2.11**.

Figure 2.11: Cut-and-pull technique to prepare STM tips. Arrows illustrating the movement to be performed. The flat nose pliers pull back at the same time as the wire cutter cuts and pulls in the indicated direction.

A sharp apex is needed to obtain a local probe for high resolution tunneling injection of electrons. **Figure 2.12** shows optical microscopy and scanning electron microscopy (SEM) images of a typical tip obtained by the cut-and-pull technique. These rough examinations are, however, not sufficient to ensure the quality of the tip. Part of the tip conditioning is unavoidably empirical. For instance, the tip can be "sharpened" in-situ when performing STM measurements by fast and controlled hits against the surface. During these mild collisions with the surface the tip can pick up clusters from the surface and hence sharpen. This process, however, might also damage the tip [67].

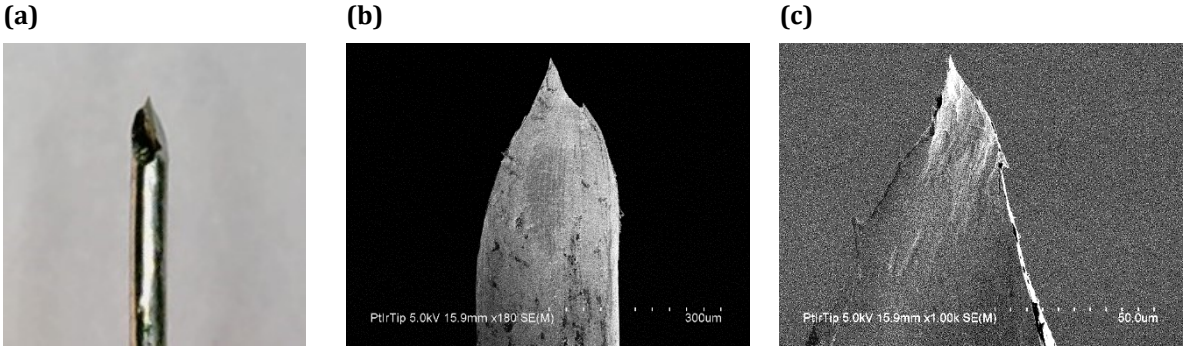

Figure 2.12: Pt-Ir STM tip made by the cut-and-pull technique. Images taken with an optical microscope **(a)** and taken via a scanning electron microscope **(b) – (c)**.

Finally, the actual quality of the tip is checked best by acquiring STM topography images. Two examples of the atomic resolution achieved with two different tips in our setups is shown in the STM topography of highly oriented pyrolytic graphite (HOPG) in **Figure 2.13**.

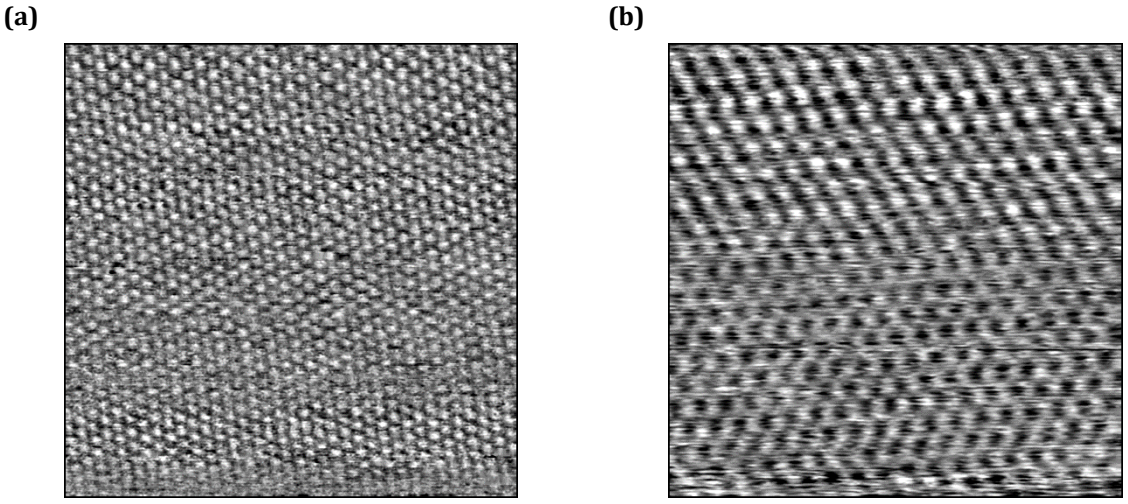

Figure 2.13: STM topography of HOPG recorded with 2 different tips revealing atomic resolution. **(a)** 7 nm × 7 nm, **(b)** 6 nm × 6 nm.

2.3.2 Taking an STL measurement

Once the STM tip is prepared, the sample is cleaned and contacted via the contact pad and one of the contact clips of the sample holder. The microscope head is inserted in the STM cryostat chamber or, respectively, the sample holder is inserted into the vacuum chamber of the RHK STL setup. The next step is the alignment of the tip relatively to the light collection setup used to perform the STL measurements. Due to potential drop on the surface of the sample, it has been proven beneficial to work as close as possible to the metal contact pad. Once the tip is positioned nearby the contact, the alignment is done by injecting the light of a halogen lamp through the collection fiber to illuminate the sample from the back through the substrate. The tip and light spot are then aligned to each other. A good alignment is achieved when the injected light reflects on the apex of the tip as shown in **Figure 2.14**.

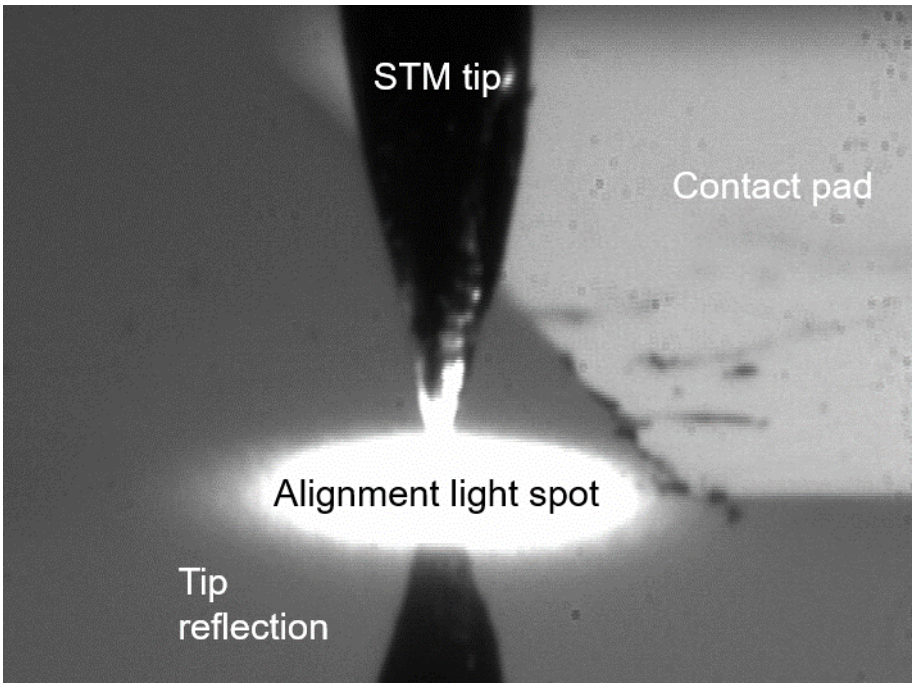

Figure 2.14: Alignment procedure of the tip centered on the light spot emerging on the sample surface illuminated through the substrate when injecting light into the optical fiber. Note that we place the tip close to the gold contact pad.

Before starting an STL study, the STM topography is measured to find an area of interest. For example, one with low defect density and an atomically flat terraces like those of the flat areas shown in **Figure 2.7**. Then, it is important to determine the values of the tunneling parameters: bias voltage and tunneling current. These values can vary from sample to sample but also on the same sample because of inhomogeneities in the surface condition or of the distance between the tip and the contact pad. To find the appropriate parameter ranges, the applied bias voltage and tunneling current are subsequently scanned while recording the STL spectra. Three characteristics have to be checked. First, the local electroluminescence spectrum should stand in the range of the beforehand recorded photoluminescence spectra. Second, the onset of the electroluminescence intensity should be reached when the applied tunneling bias voltage V_b brings the Fermi level of the metallic tip above the minimum of the semiconductor conduction band which occurs when $eV_b \approx E_g$. Luminescence signal appearing for lower tunneling bias might be due to inelastic tunneling process. Third, the variation of the tunneling electroluminescence intensity with bias voltage should follow a square root dependence above the threshold (comparable to ballistic electron emission microscopy experiments, see section **1.5**).

STL spectra can then be taken at a given tip position or along scans or maps. To perform line scans or maps the STM and the spectrometer must be synchronized. The synchronized measurement is ensured by hardware triggers and shared LabVIEW variables in both setups.

3 Results

In this chapter, we discuss the experimental results of scanning tunneling electroluminescence (STL) spectroscopy on a near-surface single quantum well (SQW) in an InGaN/GaN heterostructure. The emission line shape variations on a few nanometer scale as well as narrow emission lines stemming from single localized states are resolved. The experimental results confirm the predictions from the localization landscape (LL) theory and are, therefore, an experimental evidence of Anderson-like localization induced by the intrinsic alloy disorder. A dedicated data treatment procedure is applied to shed light on transport properties hidden in the line shape of the collected STL spectra. The findings are compared to a theoretical transport model.

3.1 Samples

To reach the required resolution to probe the localization regions by local electron injection, we use heterostructures with a single near-surface p-type InGaN/GaN QW.

3.1.1 Sample structure

The samples were grown in series by metalorganic chemical vapor deposition (MOCVD) on a 2-inch single-side polished sapphire substrate (0001) with a 0.2° miscut in an atmospheric pressure, horizontal flow reactor at the University of California in Santa Barbara by Nathan Young. The sample structure is shown in **Figure 3.1**. After a low temperature GaN nucleation layer, a 1 µm-thick unintentionally doped (UID) GaN buffer and a 1 µm-thick n-GaN ($[\mathrm{Si}] = 5 \times 10^{18}\mathrm{cm}^{-3}$) layer are grown. It is followed by a p-type GaN ($[\mathrm{Mg}] = 2 \times 10^{19}\mathrm{cm}^{-3}$) stack of 10 nm, 15 nm of $Al_{0.15}Ga_{0.85}N$ and 1 µm of p-GaN. Immediately preceding the single QW, a 100 nm of UID GaN layer is grown to prevent Mg poisoning of the emitting InGaN layer. The 3 nm UID QW layer of $In_{0.18}Ga_{0.82}N$ is then grown, followed by a 10 nm UID GaN barrier. Then, a p-GaN ($[\mathrm{Mg}] = 2 \times 10^{19}\mathrm{cm}^{-3}$) spacer layer is grown, covered by a 10 nm p+-GaN cap ($[\mathrm{Mg}] > 10^{20}\mathrm{cm}^{-3}$). A Pd/Au contact pad, processed on the highly doped p++-GaN top layer, provides an Ohmic contact to apply the tunneling bias between the scanning tunneling microscope (STM) tip and the sample [43]. The thickness of the p-GaN spacer layer is either 10 nm or 90 nm. These two different thicknesses allow to assess the effect of the distance between the injecting tip and the QW on the resolution. In the following, we refer to the respective samples as S10 and S90, corresponding to the p-GaN spacer layer thickness.

The band structure profiles in real space of the two samples are shown in **Figure 3.1 (b)** and **(c)**. They are calculated with the One-Dimensional Drift-diffusion Charge Control (1D DDCC) solver of Yuh-Renn Wu from the National Taiwan University [73]. This calculation shows that the band bending region (BBR) extends only over a few nanometers, i.e., less than the thickness of the top p++-GaN contact layer. This result indicates that the QW is located in the "flat-band region" and is hence populated with holes.

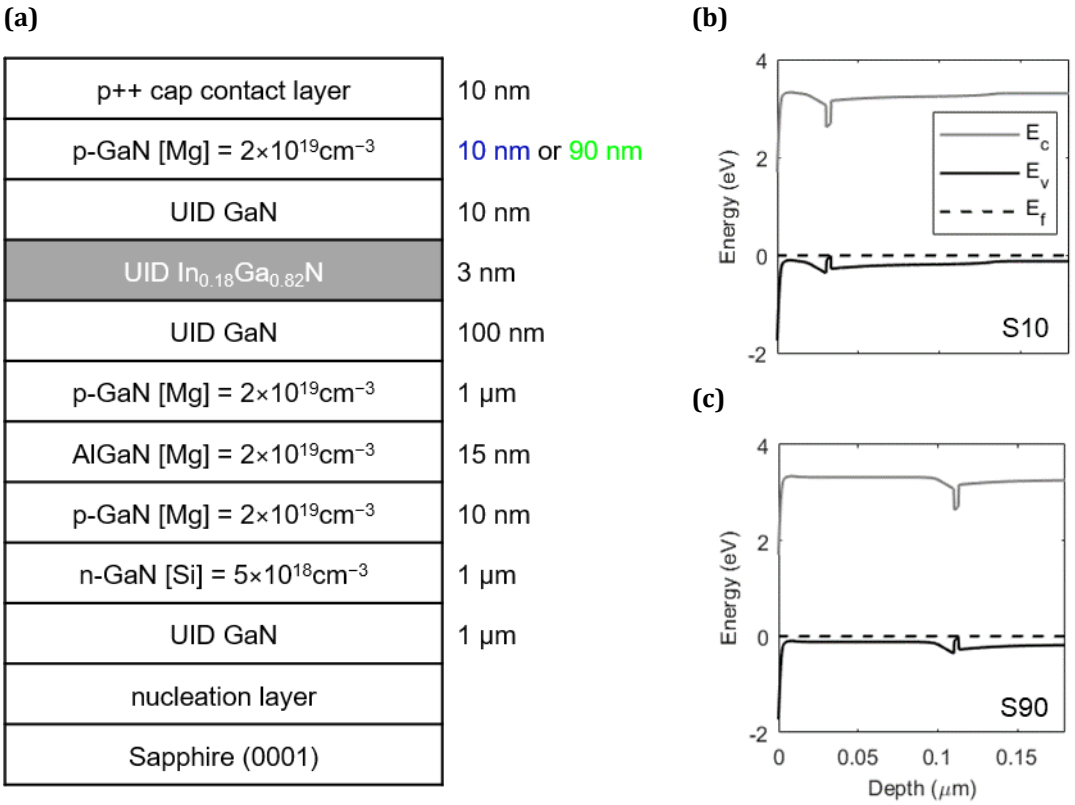

Figure 3.1: (a) Sample structure. Note that the InGaN QW is buried under a GaN layer of either 30 nm (S10) or 110 nm (S90) thickness. **(b) – (c)** Band profiles showing the conduction band E_c, the valence band E_v as well as the Fermi energy E_f of the S10 and S90 samples calculated with the 1D DDCC solver developed by Yuh-Renn Wu at the National Taiwan University [68].

3.1.2 Sample preparation

3.1.2.1 Cleaning

To ensure a clean surface of the samples for STL measurements, a two-step cleaning procedure is performed. First, to get rid of organic contamination, the sample is treated with piranha solution (H_2O_2:H_2SO_4 of ratio 1:3) for 60 s. Afterwards, the sample is rinsed first with milliQ water and then with ethanol, followed by isopropanol and finally dried [66]. In the second cleaning step, the sample is treated for 90 s with a HCl-isopropanol solution which removes the native oxide and passivates the surface [69,70]. Before drying, the sample is rinsed with isopropanol. This cleaning procedure has to be performed regularly especially when working in ambient conditions to ensure a comparable surface quality each time.

3.1.2.2 Contacts

Nitride samples are provided by our collaborators with a metallic contact pad processed on the p+-doped GaN surface. Due to the repeated cleaning of the samples before each experiment the original Pd/Au contacts on the sample surface degrade or even peel off. Therefore, they have to be renewed regularly. New 100 nm-thick Au contacts are evaporated under vacuum. These contacts might exhibit a slightly rectifying character.

3.1.3 Sample characterization

The photoluminescence spectra of the S10 and S90 sample are shown in **Figure 3.2**. The excitation wavelength is λ = 394 nm and the power is P ~100 mW. The optical detection setup is identical to the one used for our STL experiment (introduced in **Chapter 2 Experimental Method**). Both samples exhibit a blue emission, peaked at 2.75 eV and 2.80 eV for S90 and S10, respectively. This difference stems probably from a small deviation between the actual and nominal sample compositions. The full width at half maximum (FWHM) is approximately 150 meV for S90 and 180 meV for S10.

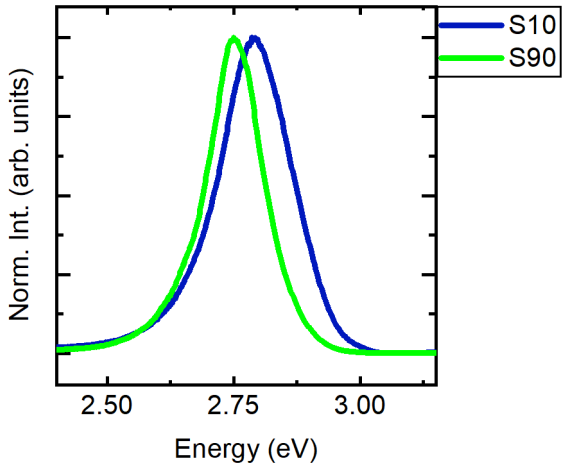

Figure 3.2: Normalized photoluminescence spectra of the S10 and S90 sample with an excitation wavelength of 394 nm (~3.14 eV) at a power of ~100 mW.

Scanning electron microscope (SEM) images of the S90 sample are shown in **Figure 3.3**. A contrast between different layers of the structure is observed due to changes in alloy composition or doping. In **Figure 3.3 (b)**, the 3 nm-thick InGaN QW layer located 110 nm below the surface appears as a dark line. We see dislocations propagating across the structure which emerge at the sample surface inducing the formation of V-pits.

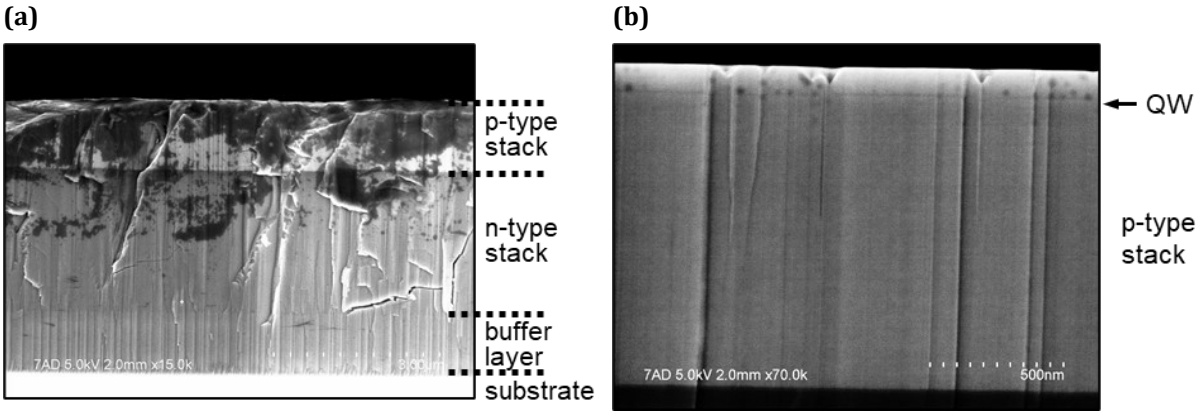

Figure 3.3: SEM images of S90 in cross section**. (a)** The contrast appears between the different layers of the structure. Dislocations propagating across the structure are observed. **(b)** A zoom on the p-type stack evidences the InGaN QW layer (dark line) and the V-pits characteristic of the dislocations emerging at the surface.

Figure 3.4 shows STM images measured on both the S10 and S90 sample surfaces on different positions and scales. The top p++-GaN surface exhibits ~150 nm wide atomically flat terraces separated by (bi-)atomic steps, which corresponds to the substrate miscut (see **Chapter 2**

Experimental Method). We observe hexagonal pits (with a density of ~10^9 cm^{-2}) characteristic of the dislocations emerging on the c-plane GaN surface. Different positions on the sample surface exhibit different morphologies. Before performing an STL measurement, we, therefore, search for a flat area without defects to avoid surface effects to influence our findings.

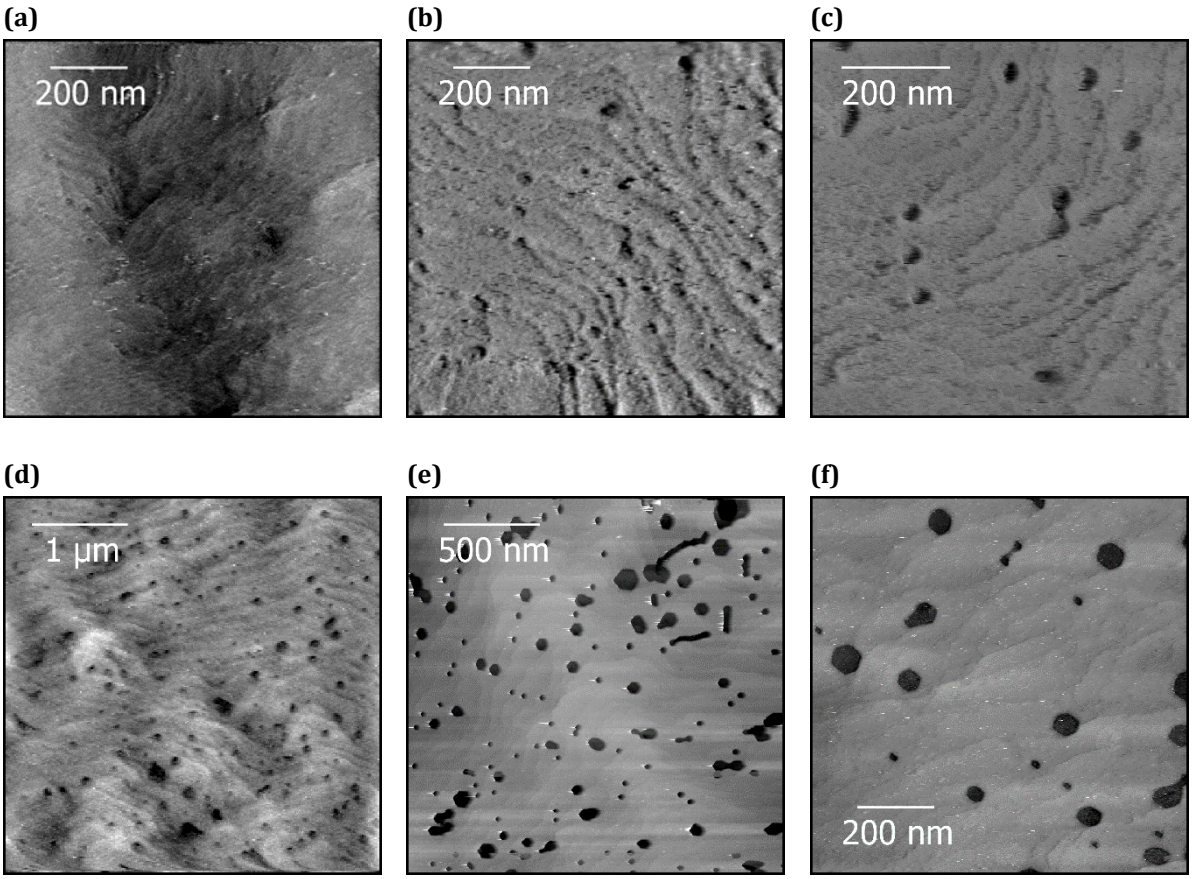

Figure 3.4: Topography with different gray scales for S10 **(a)**, **(b)** 1000 nm × 1000 nm **(c)** 700 nm × 700 nm; S90 **(d)** 4000 nm × 4000 nm **(e)** 2000 nm × 2000 nm **(f)** 1000 nm × 1000 nm.

To check the bandgap, the surface band bending amplitude as well as the conductivity of the sample, we systematically record scanning tunneling spectroscopy (STS) IV-curves. The applied tunneling bias voltage ramps back and forth between 3.0 V and -3.0 V for S10 and between 4.0 V and -4.0 V for S90. The measurement conditions for the two samples differ in loop gain as well as in tunneling current setpoint: 1 nA at 3 V for S10 and 25 nA at 4.0 V for S90. The obtained curves for S10 and S90 are plotted in linear and logarithmic (for the absolute values) scale in **Figure 3.5**. We indicate the bandgap estimated from the logarithmic plot of the IV-characteristics to be ~3.3 eV for S10 and ~3.4 eV for S90, close to the expected value of 3.45 eV.

For both samples, the positive current at positive bias is larger than the negative current at negative bias voltage. The former corresponds to electron injection from the tip into the sample, while the latter to electrons tunneling from occupied states of the sample into the STM tip. From these curves, the energy position of the top of the valence band at the surface can be estimated to be 1.9 eV below the Fermi level while it is about 0.2 eV in the bulk. This gives a value of the amplitude of the surface band bending region of about 1.7 eV.

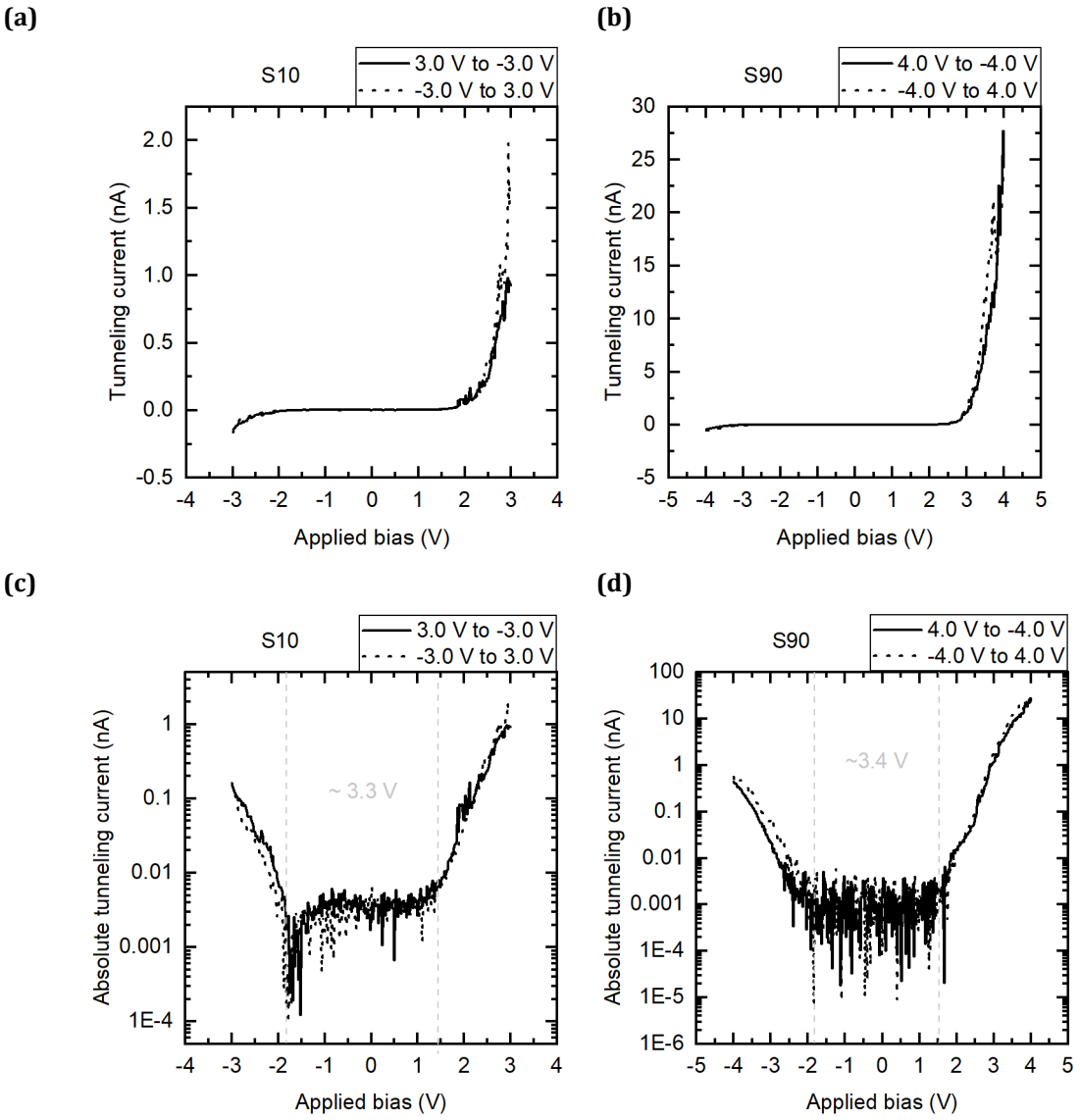

Figure 3.5: Scanning tunneling spectroscopy IV-curves recorded on **(a)** S10 and **(b)** S90 at 300 K in linear scale (top row) and the corresponding logarithmic plots of the absolute tunneling current in **(c)** for S10 and **(d)** for S90 (bottom row). The bias is applied to the sample while the tip is grounded.

3.2 Scanning tunneling electroluminescence spectroscopy

3.2.1 Electroluminescence tunneling injection spectroscopy

As schematized in **Figure 3.6 (a)**, when applying a large enough positive tunneling bias voltage V_b to the sample, electrons may be injected into the conduction band of the top GaN layer and transported to the InGaN QW. There, they can recombine radiatively with holes that populate the QW due to the surrounding p-doped layers. In **Figure 3.6 (b)**, we plot the spectrally integrated STL intensity measured on the S90 sample as a function of V_b. Similar variations are measured on S10 sample. The luminescence onset threshold is observed at $V_{th} \approx 3.6$ V. This value corresponds approximately to the energy separation of 3.25 eV between the Fermi level and the conduction band minimum in the p-GaN layer beyond the BBR. The slight difference can be attributed to a potential drop, either in the access resistance (between the injection area and the contact pad) or through the slightly rectifying contact. Beyond the threshold bias V_{th}, the luminescence intensity

increases quadratically in $(V_b - V_{th})$ [57] until it reaches a plateau beyond 4.5 V. This saturation might be due to electron injection into upper conduction valleys or to other processes which would prevent hot electrons from radiatively recombining in the InGaN QW [71,72].

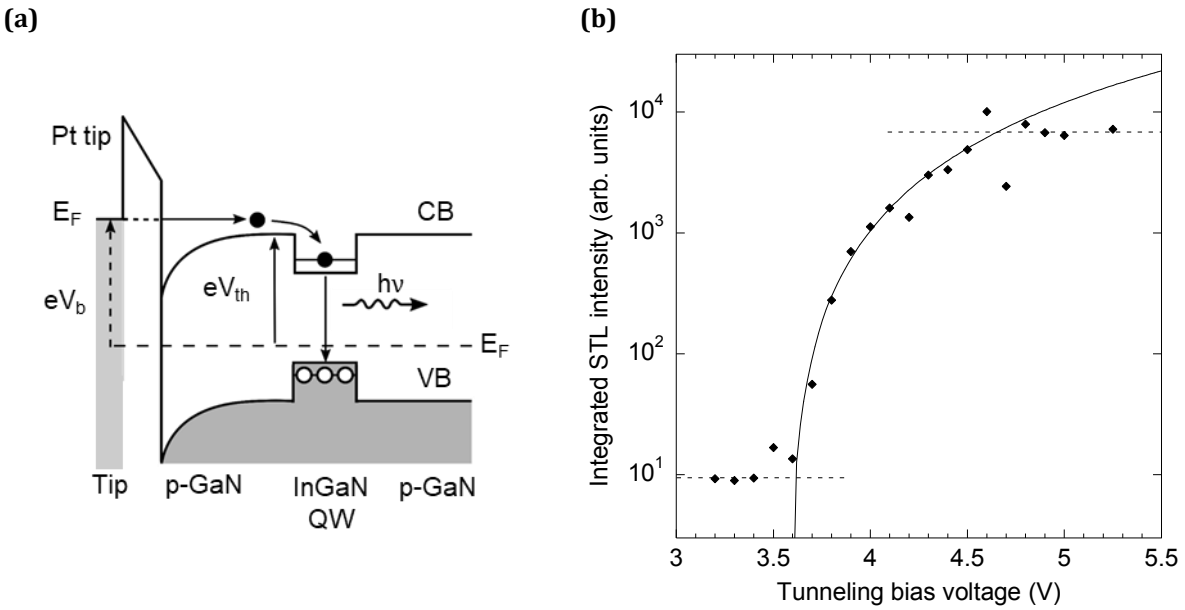

Figure 3.6: (a) Schematics of the tunneling injection of electrons in the conduction band and of their recombination in the QW of the sample structure shown in **Figure 3.1**. **(b)** Spectrally integrated luminescence intensity measured on S90 as a function of V_b for a constant tunneling current of 20 nA. The solid line is the fit of the experimental points using the function $(V_b - V_{th})^2$ with $V_{th} \approx 3.6$ V.

3.2.2 Electroluminescence spectroscopy under local tunneling electron injection

A representative set of local tunneling electroluminescence spectra is shown in **Figure 3.7**. These spectra are measured on the S10 (blue curves) and S90 (green curves) sample under local electron injection in various tunneling conditions (current and bias voltage) and on various locations on the sample surfaces. The spectra recorded at 2 nA tunneling current have an optical resolution of 35 meV whereas the optical resolution of the spectra recorded at 20 nA is 26 meV.

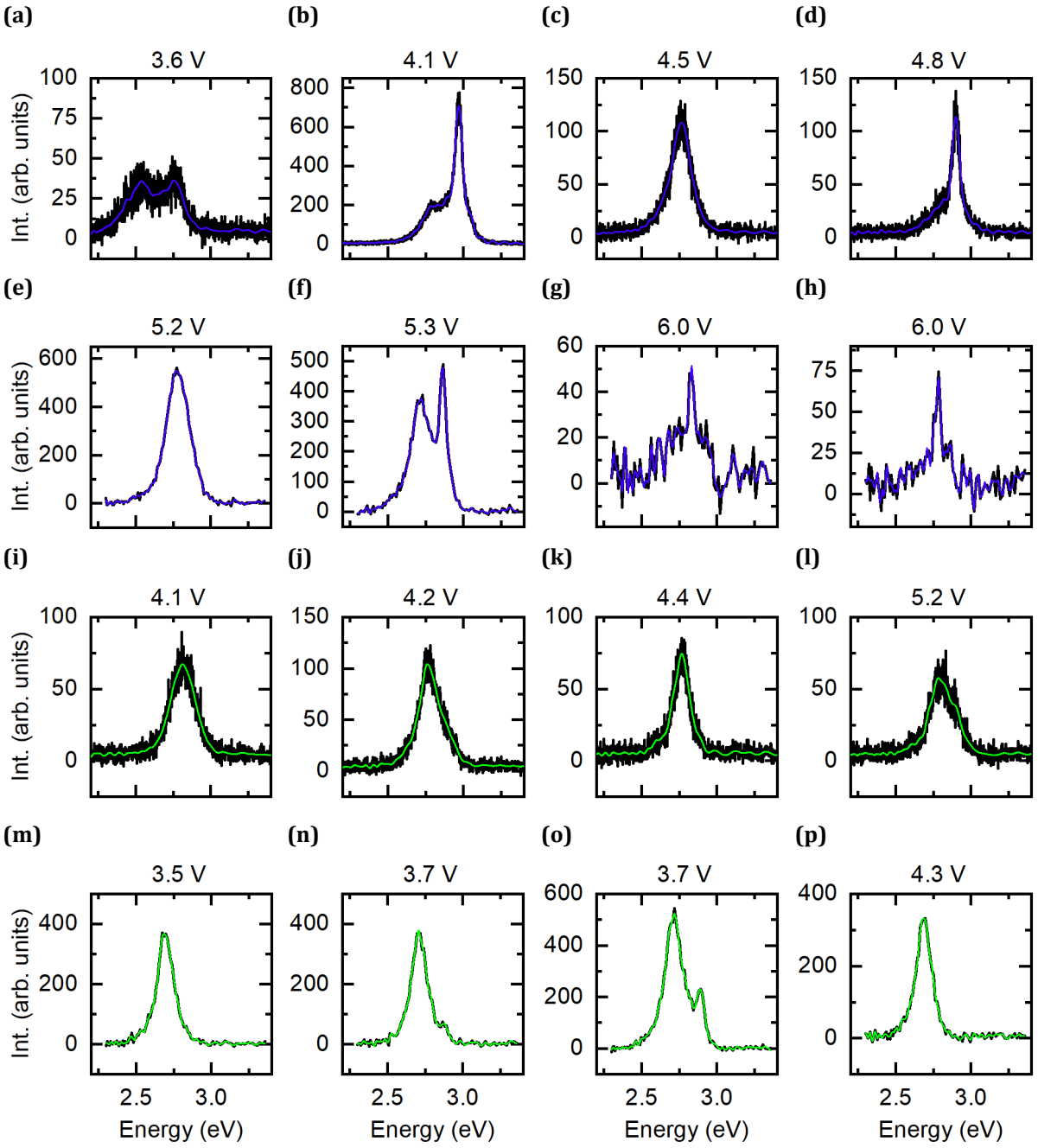

Figure 3.7: Local tunneling electroluminescence spectra measured under local electron injection on **(a) – (h)** S10 sample at **(a) – (d)** 2nA and **(e) – (h)** 20 nA, and on **(i) – (p)** S90 sample at **(i) – (l)** 2 nA and **(m) – (p)** 20 nA. The applied tunneling bias voltage is indicated on top of each spectrum. The black curves are the background-corrected raw data. The colored curves are the spectra obtained after the smoothening procedure explained in the Appendix A.

For each sample, the first row of spectra corresponds to a tunneling current of 2 nA, while the second row corresponds to a tunneling current of 20 nA. The tunneling bias is indicated in each plot. The spectra are displayed with increasing voltage from left to right. The acquisition times for each spectrum are 10 s for S10 at 2 nA and 2 s at 20 nA; 5 s for S90 at 2 nA and 2 s at 20 nA.

From these measurements, we can draw four main conclusions. First, the STL spectra peak at an energy close to the emission of the InGaN QW measured by PL. Second, while the PL exhibits a broad spectrum which does not depend strongly on the area on the sample, the STL spectra exhibit a variety of shapes from narrow lines to broad emission bands with eventually separated multiple

contributions. Third, the peak energy fluctuates within a range comparable to the width of the PL spectrum. Fourth, there is no obvious correlation between the line shape and the tunneling conditions (current, bias voltage).

These observations indicate that the local tunneling electroluminescence spectra provides signatures of the local properties of the QW. To demonstrate that these properties are related to the quantum alloy disorder, the changes in the tunneling electroluminescence spectrum must be measured and analyzed at the scale of the composition fluctuations.

3.2.3 Line scans

The straightforward approach to evidence changes in the electronic processes in the QW at the scale of the composition fluctuations is to perform a two-dimensional spectroscopic mapping of the QW by STL. However, this is a very demanding experiment particularly in terms of STM stability. Indeed, recording a single tunneling electroluminescence spectrum requires an acquisition time of about 10 s. According to the LL simulations, the typical size of the localization regions induced by the compositional disorder is of the order of 5 nm. Probing an area comparable to the ultimate optical far-field microscopy resolution ($\lambda/2 \sim 250$ nm in the blue spectral range), would require scanning the surface for approximately 25000 s (about 7 hours) to record 2500 spectra (one in every 5 nm × 5 nm area). This requirement is beyond the capabilities of our experimental STL setup (and probably of most local probe instruments). Thus, we here restrict our measurement procedure to the acquisition of line scans. These line scans consist in moving the STM tip on a straight line by steps of 5 nm and taking the emitted tunneling electroluminescence spectrum at each position between two scanning steps. This procedure allows to probe local fluctuations of the QW emission at the scale of a few nanometers over typical distances of several tens or hundreds of nanometers in a reasonable acquisition time (~500 s) compared to the stability of the STM setup at ambient conditions.

Figure 3.8 shows examples of parts of such line scans measured on the S10 sample in different areas and with different bias voltages but with the same tunneling current of 2 nA. In all these line scans, significant changes in the emission line shape, peak position and intensity are observed at the scale of the 5 nm scanning step. Moreover, in some cases narrow emission lines are resolved as in **Figure 3.8 (d)**, highlighted in blue.

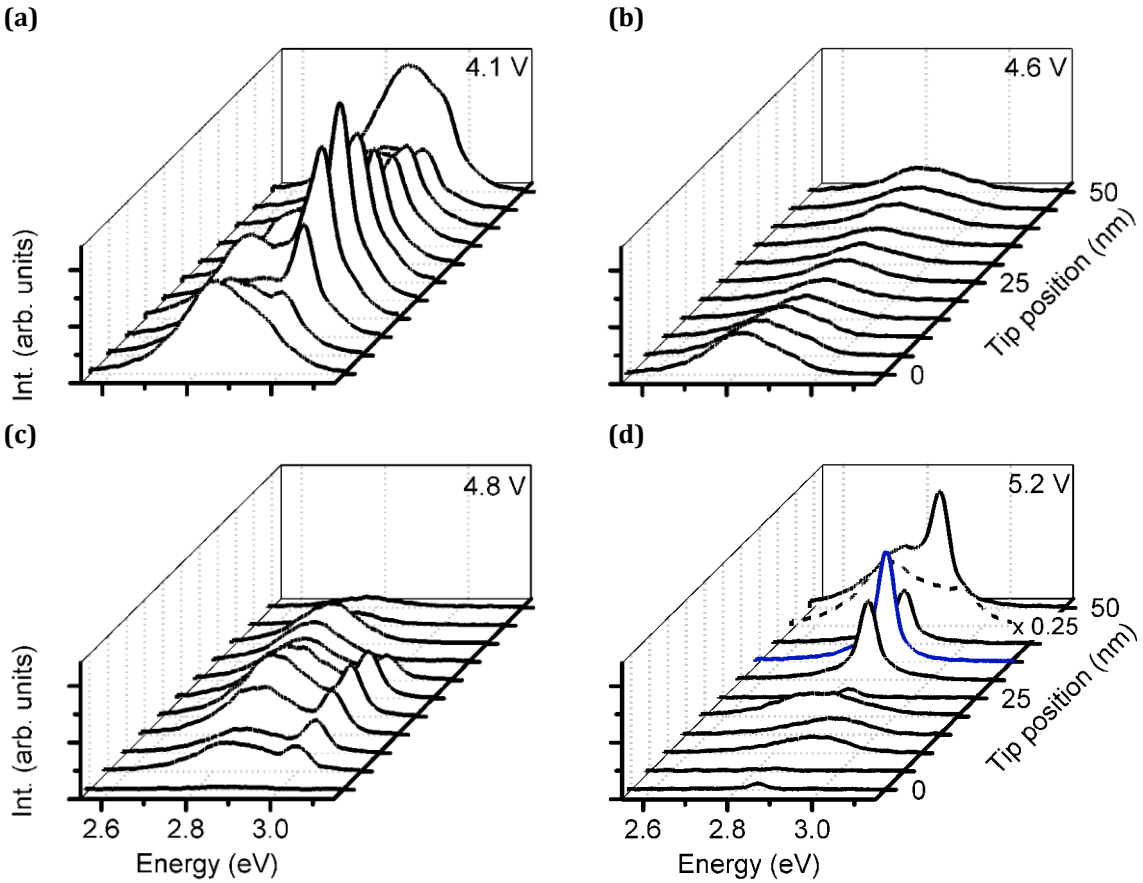

Figure 3.8: Line scans measured on S10 sample with 2 nA injection current and tunneling bias: **(a)** 4.8 V, **(b)** 4.6 V, **(c)** 4.8 V, and **(d)** 5.2 V. The graphs are plotted on the same intensity scale. The narrowest emission line is highlighted in blue in **(d).**

This narrow emission line is reproduced in **Figure 3.9**. The intensity of this line increases by an order of magnitude over 10 nm, from the position 20 nm to the position 30 nm.

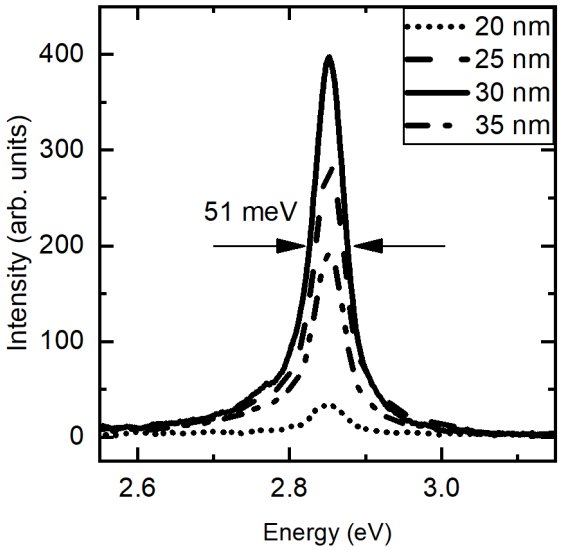

Figure 3.9: Evolution of the measured narrow emission line (taken from **Figure 3.8** at different positions of the line scan). The FWHM of this emission line is 51 meV which corresponds to 36 meV when taking into account the spectrometer resolution.

Beyond the position 30 nm the intensity of this narrow emission line drops and the line shape changes significantly at 35 nm. The narrow line measured at the position 30 nm shows a FWHM of ~51 meV, which corresponds to an actual FWHM of ~36 meV when accounting for the 35 meV resolution of the optical spectroscopy setup. This line width is, thus, comparable to the 36 meV FWHM of the emission of a single GaN quantum dot measured at room temperature [54].

As further discussed in section **3.4**, we conclude that these narrow emission lines are the signature of electron recombination from single localized states. The attenuation of this narrow contribution over a scale of 5 to 10 nm indicates a characteristic size of the localized state of the order of a few nanometer. This size coincides with the one expected for disorder-induced localization regions. The short attenuation length also suggests that carrier transport is limited to few localized states.

As a reminder, the results shown here are collected from a sample with a near-surface single QW with about 30 nm thick cap layers (S10). The spatial resolution of the STL measurements should strongly depend on the distance crossed by the carriers from the BBR to the QW. Thus, we expect significant differences between the S10 and S90 sample, since the latter has a larger cap GaN stack thickness of in total 110 nm.

In **Figure 3.10**, we compare the variation of the STL spectra recorded on the S10 and S90 sample during a 250 nm-long line scan with 5 nm step size. The tunneling conditions are 4.1 V and 2 nA. As already observed in **Figure 3.8**, the STL spectra of S10 are characterized by significant fluctuations in intensity, peak position and line shape from multiple contributions, including narrow emission lines. The sum of all the spectra collected during this line scan [shown in (**Figure 3.10 (c)**] gives a FWHM of about 280 meV, even broader than the photoluminescence spectrum in **Figure 3.2**. This observation reveals the contribution from multiple states. In contrast, the spectra recorded on the S90 sample with the same scanning and tunneling parameters do not exhibit significant changes in intensity, line shape or peak position. Moreover, narrow emission lines are not observed. This outcome is consistent with previous experimental results reported in the literature [62,63] and with our assumption: resolution at the scale of a few nanometer cannot be obtained on a sample with a thick cap layer on top of the QW. The injected electrons spread during the transport from the BBR to the QW over on area which is much larger than the typical size of the localization regions induced by the alloy disorder. Thus, many localization regions are injected at once and the spectrum measured at a given tip position corresponds to the sum of all these contributions. As a consequence, the sum (**Figure 3.10**) of all the spectra along this line scan is very similar to each single spectrum and exhibits a featureless line shape of 200 meV FWHM comparable to the photoluminescence spectrum plotted in **Figure 3.2**.

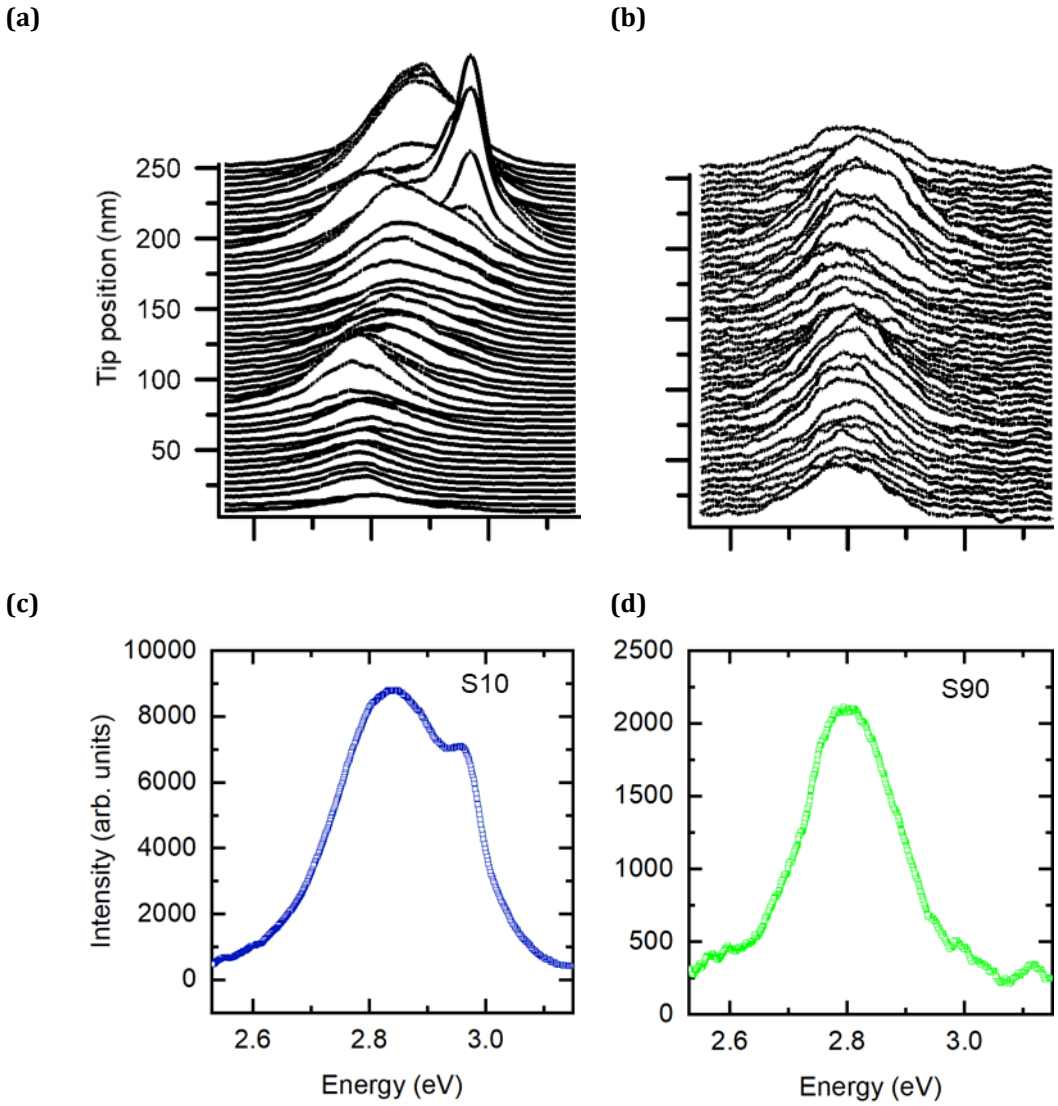

Figure 3.10: Line scan on **(a)** S10 and **(b)** S90 showing the line shape evolution along 250 nm with a step width of 5 nm between the different spectra. **(c)** and **(d)** respective sums of the spectra of the line scans for S10 and S90 shown above.

3.2.4 Comparison of STL measurements with LL theory simulations

One of the characteristics of the local electroluminescence spectra is their peak energy. We thus analyze the spectra of six different line scans taken at different positions of the surface of both samples. The histograms of **Figure 3.11 (a)** represent the distributions of the energy of the highest intensity peak collected from spectra for samples S10 (blue histogram) and S90 (green histogram). It is evident that the S90 sample has a much narrower peak energy distribution.

Using the LL theory, the potential landscape is calculated for electrons and holes over a 30 nm × 30 nm area of a simulated InGaN/GaN QW structure with random In distribution and an average In content comparable to the one of our samples. From these calculations we deduce the local effective bandgaps in the localization regions. The distribution of local effective bandgaps determined over ten different simulations are plotted in the histogram of **Figure 3.11 (b)**. This distribution exhibits wings that extend over roughly 250 meV, a range comparable to the spread of the peak emission energies of S10 sample. In contrast, the distribution of the peak emission energy of the S90 sample is much narrower since each local electroluminescence spectrum is already an average due to the summed emission from many regions.

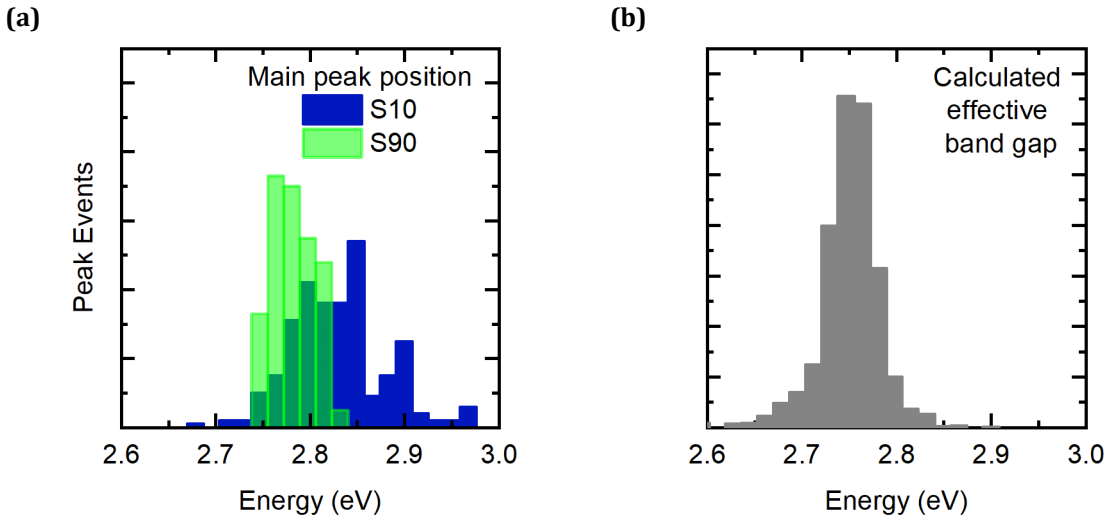

Figure 3.11: (a) Histogram of the main STL peak position of six different line scans recorded at different positions at the surface of the sample. **(b)** Histogram of the local bandgap from the effective bandgap calculated by the LL theory.

The fluctuations of the local effective bandgap calculated by the landscape theory, when accounting for the intrinsic compositional disorder of the InGaN ternary alloy, are thus consistent with the fluctuations of the peak energy of the STL spectrum measured on the S10 sample. Although a direct relationship between these two quantities cannot be straightforwardly established, it is a further indication that the spatial variations over a few nanometers of the STL spectrum originate from the localization effect induced by the ternary alloy disorder. We, therefore, need a more elaborated way to describe the experimentally observed spectra as well as a theoretical model of those.

3.3 Analysis of STL spectra line shape

It is clear from the line scans presented in the previous section that the local electroluminescence spectra carry more information than the peak position. It is also evident that even in spectra or line scans which do not exhibit remarkable features (including those measured on the S90 sample), fluctuations in the intensity, line shape and peak position are in fact present. To extract more information on the local properties of the QW, we developed a procedure to treat the spectra line shape, deduce characteristic quantities and analyze their spatial fluctuations.

The need of a dedicated data treatment for STL spectra is justified by the large variety of the observed line shapes, as discussed in the previous section (see for example the spectra variety in **Figure 3.7**). The line shapes vary from single narrow emission lines, to significantly asymmetric broad emission bands and eventually exhibit separated multiple contributions. It is clear that the line shape and width cannot be explained by the usual phenomena related to carrier lifetime and thermal motion. We have thus developed a reliable data treatment which allows to extract the integrated intensity, the peak energy as well as the low-energy half width at half maximum, W_{LE}, and the high-energy half width at half maximum, W_{HE}. The W_{LE} and W_{HE} will allow us to reveal and analyze the asymmetry of the line shape which is characteristic for the different contributions from the localization regions that are probed with the local electron injection. The data treatment includes the removal of artefacts, the background correction and a smoothing procedure based on the filtering of high frequency contributions in the spectra Fourier transform. The whole data

treatment is described in **Appendix A**. In the following, we discuss the analysis of spectra which have all been treated through this procedure.

In **Figure 3.12**, we exemplify on selected spectra the relevant quantities that will be considered. The peak energy, E_P, is taken on the main contribution of each local STL spectrum. Then, we extract the energies E_{LE} and E_{HE} which correspond to the energy positions of the two extreme points of the spectrum at half of the peak intensity. The uncertainty on the determination of these energies is related to the spectrum acquisition sampling. The half widths at half maximum at low and high energy are then respectively equal to $W_{LE} = E_P - E_{LE}$ and $W_{HE} = E_{HE} - E_P$. Finally, the integral intensity is the sum over all the counts of the spectrum.

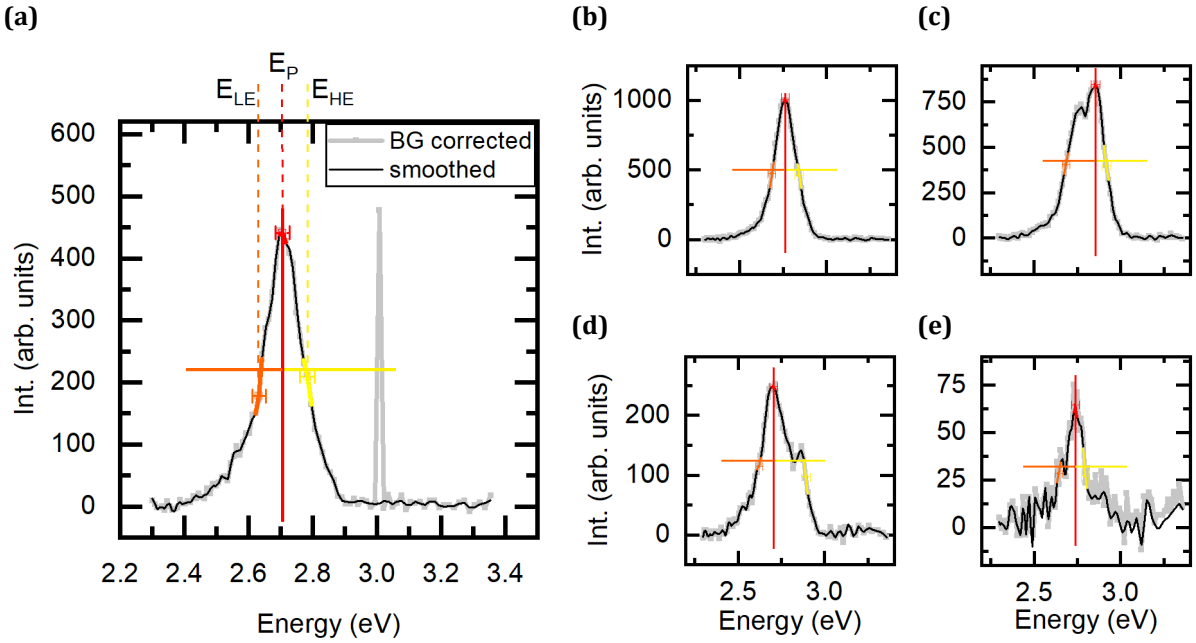

Figure 3.12: (a) Illustration of the data analysis applied to an STL spectrum (see **Appendix A**). The quantities extracted from this analysis are E_P = 2.706 ± 0.022 eV, W_{HE} = 78 ± 23 meV, W_{LE} = 73 ± 20 meV. **(b-e)** Same analysis applied to a selection of spectra with different line shapes; (b) E_P = 2.761 ± 0.023 eV, W_{HE} = 81 ± 24 meV, W_{LE} = 77 ± 21 meV; **(c)** E_P = 2.855 ± 0.024 eV, W_{HE} = 62 ± 25 meV, W_{LE} = 170 ± 21 meV; **(d)** E_P = 2.706 ± 0.022 eV, W_{HE} = 185 ± 25 meV, W_{LE} = 83 ± 20 meV; **(e)** E_P = 2.739 ± 0.022 eV, W_{HE} = 57 ± 23 meV, W_{LE} = 96 ± 21 meV.

3.3.1 Analysis of line scans at low tunneling current (2 nA)

Following the procedure described above, we analyzed the spectra of the line scans shown in **Figure 3.13 (a)** and **(c)**, recorded on the S10 and S90 samples at applied bias voltage of 4.3 V and injected tunneling current of 2 nA. The corresponding spatial variations of W_{HE}, W_{LE}, E_P and of the integrated intensity are plotted in **Figure 3.13 (b)** and, respectively, **(d)**. We can draw three general observations. First, spatial variations of W_{HE}, W_{LE}, E_P and of the integrated intensity are observed on the scale of 5 nm. This length scale corresponds to the expected characteristic size of the localization regions induced by alloy disorder. Second, the spatial fluctuations of W_{HE}, W_{LE} and E_P are significantly weaker on S90 sample than on S10 sample. This behavior is to be expected since, as we already discussed, each local tunneling electroluminescence spectrum measured on the S90 sample is the sum of the contributions of many localization regions. On the contrary, the number of localization regions probed at once in the case of the S10 sample should be small. Third, a strong positive correlation clearly emerges between W_{LE} and E_P while a negative correlation is observed between W_{HE} and E_P. It is remarkable that these correlations are observed on both

samples although the STL resolution is expected to be much larger on S90 sample. Despite that the observation of the emission from single localized states is very improbable for the S90 sample, STL spectroscopy still provides information on the potential fluctuations in the QW at the scale of the expected disorder-induced localization.

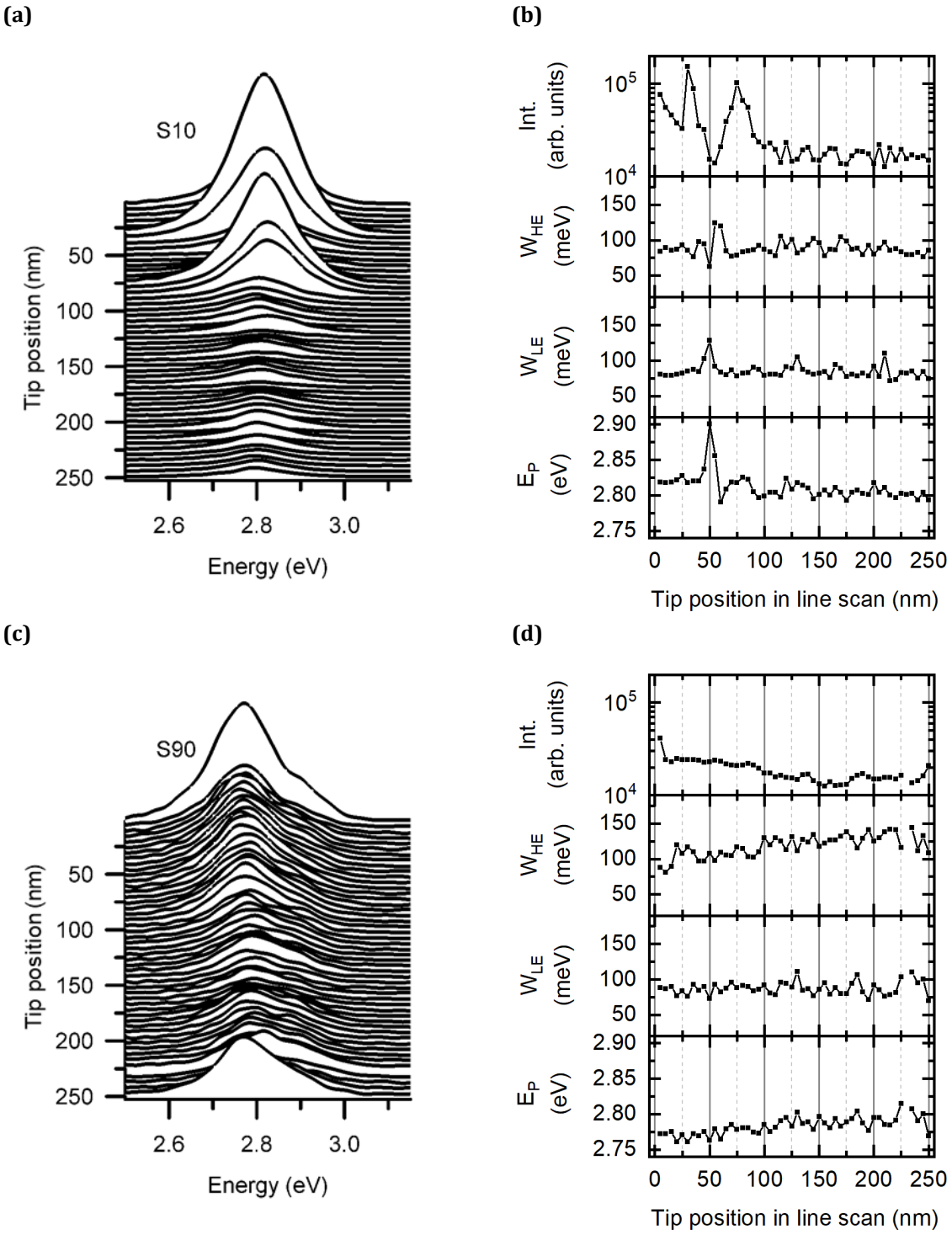

Figure 3.13: Line scans measured at an injection current of 2 nA on S10 **(a)** – **(b)** and S90 **(c)** – **(d)** at a bias of 4.2 V. The spectra are taken with a spacing of 5 nm on line scans of length 250 nm. **(a)** (respectively **(c)**) Spectra of the line scan, and **(b)** (respectively **(d)**) data treatment of those spectra for S10 (respectively S90).

These correlations are systematically observed on a wide range of applied bias voltages. **Figure 3.14** shows the results of the analysis of line scans for applied biases ranging from 3.9 V to 5.2 V with 2 nA tunneling current on the S10 and S90 sample, respectively. More than a thousand spectra are analyzed for each sample.

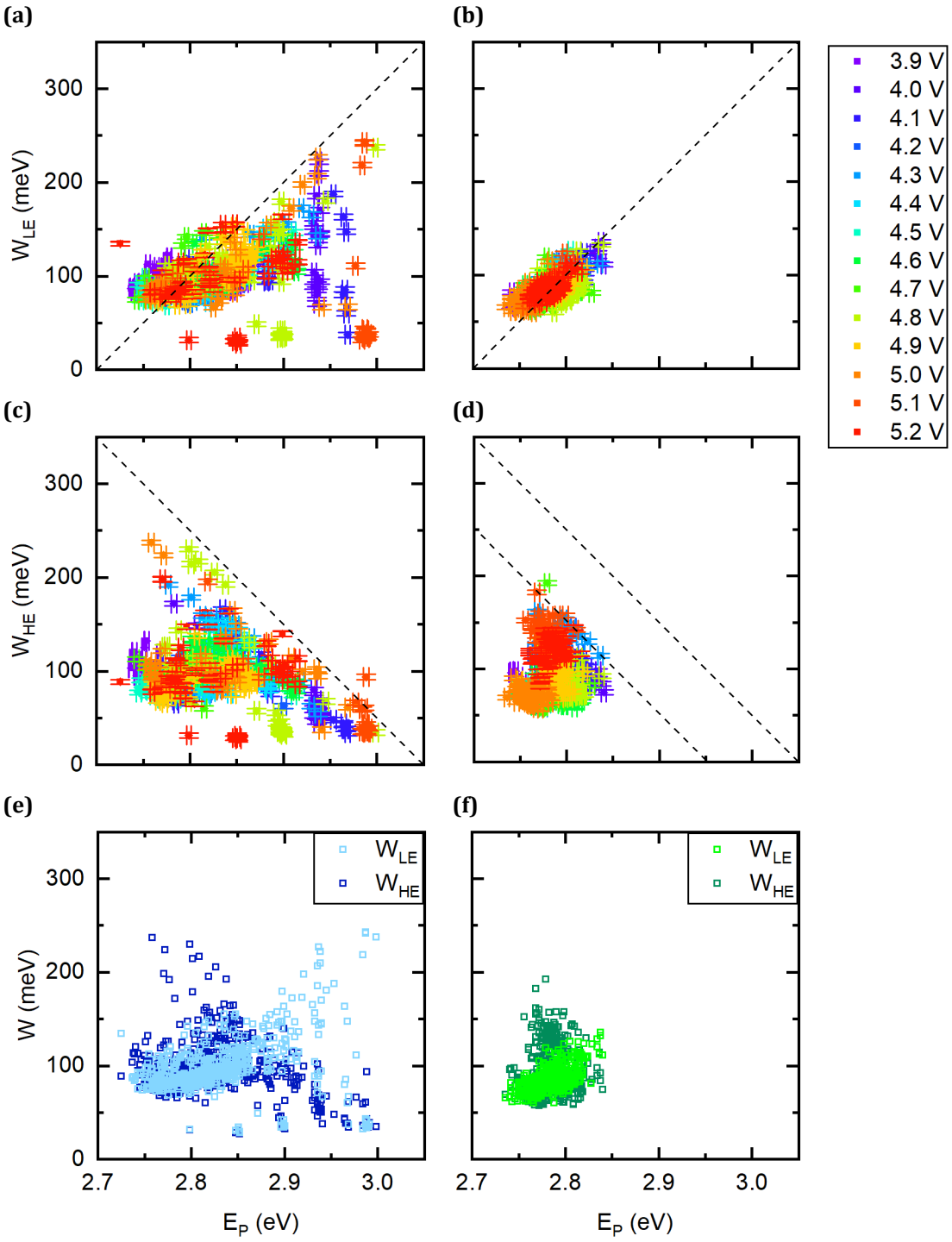

Figure 3.14: Variation of W_{LE} and W_{HE} at low injected current of 2 nA against E_P for line scans recorded on **(a – c)** S10 and **(d – f)** S90 samples with applied bias varying from 3.9 V to 5.2 V at 2 nA. In **(e)** and **(f)** all data of W_{LE} (light colors) and W_{HE} (dark colors) are superimposed. The dashed lines have a slope of 1 in **(a)** and **(b)** and a slope of -1 in **(c)** and **(d)**.

The variation of W_{LE} and W_{HE} is plotted against E_P. Each data point corresponds to one spectrum of a line scan. In the **Figure 3.14 (a)**, **(b)**, **(d)** and **(e)**, all the data points are plotted with the same

color scheme: the color is different for each line scan, i.e., for each bias voltage indicated in the legend. The statistical analysis of the whole set of line scans recorded on the S10 and S90 samples confirms the main observations deduced from the plots in **Figure 3.13** showing the spatial variation of E_P, W_{LE} and W_{HE} along a single line scan.

The range over which the values of E_P, W_{LE} and W_{HE} are spread is significantly weaker on the S90 sample than on the S10 one. The value of E_P fluctuates over 260 meV for the S10 sample and over 110 meV for S90 sample. These ranges are comparable to the extension of the histograms of the peak position in the preliminary data treatment (**Figure 3.11**). Similarly, the fluctuations of W_{LE} extend over 170 meV (210 meV when counting the extreme points outside the main data accumulation) for the S10 sample and over 80 meV for the S90 sample. The W_{HE} stretches over 220 meV for the S10 and 150 meV for the S90. These observations confirm once again that the STL measurements performed on the S90 sample with a thicker cap layer on top of the QW average over many more localization regions than those performed on the S10 sample.

A clear positive correlation is observed on both samples between E_P and W_{LE} (the dashed lines in **Figure 3.14 (a)** and **(d)** have a slope of 1), while a slightly negative correlation is observed between E_P and W_{HE} (the dashed lines in **(b)** and **(e)** have a slope -1). Hence, a high peak energy corresponds to a broadening towards low energy while a low peak energy corresponds to a broadening towards high energy. We will further discuss these correlations on the basis of a qualitative model that considers energy relaxation of the injected electrons and transport between localized states in section **3.4**.

As described in **Appendix A**, the correlation can be characterized by the Pearson coefficient r, which is 1 for a total positive linear correlation (respectively -1 for a total negative linear correlation) and 0 for no linear correlation. Values greater than 0.05 (respectively smaller than -0.05) are considered significantly nonzero. The values of r calculated for E_P and W_{LE} on the S10 and S90 samples are:

$$r_{S10,LE,2\ nA} = 0.2939,$$

$$r_{S90,LE,2\ nA} = 0.6373.$$

These values confirm a positive correlation. The correlation coefficient for S90 is stronger due to the lack of extreme values outside the main accumulation of data points originating from, for example, single localized state emission.
The values of the Pearson correlation coefficient calculated for E_P and W_{HE} on the data measured on S10 and S90 samples are:

$$r_{S10,HE,2\ nA} = -0.3389,$$

$$r_{S90,HE,2\ nA} = 0.1193.$$

A strong concentration of data points is observed at low energies with a cut-off to higher energies along a line of slope -1, clearly seen for the S10 sample. For S10, the shape of the data cloud indicates a slightly negative linear correlation confirmed by the value of r. For S90, the general shape of the data cloud looks similar but extends over a narrower energy range. In contrast a positive correlation is retrieved by the value of r.

3.3.2 Analysis of line scans at high tunneling current (20 nA)

To investigate the dependence of electron-hole recombination from localized states as a function of the injected carrier density, we performed similar experiments with a higher tunneling current of 20 nA and applied tunneling bias voltage ranging from 3.0 V to 6.0 V.

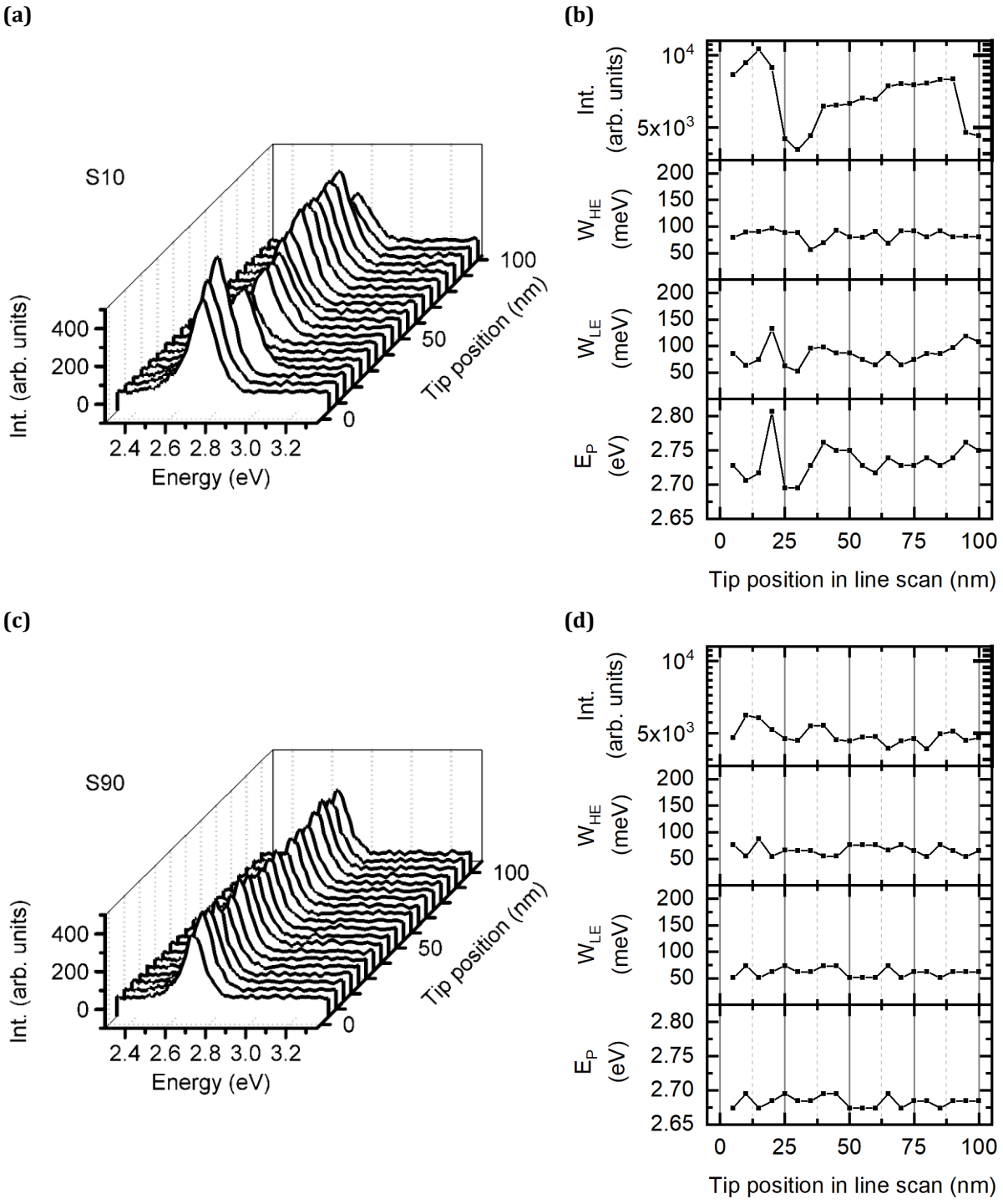

Figure 3.15: Line scans measured at a tunneling current of 20 nA on S10 **(a) – (b)** and S90 **(c) – (d)** at a bias of 4.3 V. Spectra are taken with a spacing of 5 nm. **(a)** (respectively **(c)**) Spectra of the line scan. **(b)** (respectively **(d)**) data treatment of these line scan spectra for S10 (respectively S90).

Typical spectra acquired at 20 nA on the S10 and S90 sample are shown in **Figure 3.7 (e)** to **(h)** and **(m)** to **(p)** respectively. A part of a line scan and its analysis is shown in **Figure 3.15 (a)**, **(b)** for the S10 and **(c)**, **(d)** for the S90 sample, respectively. Once again, fluctuations at the scale of 5 nm, the scanning step, are observed on W_{HE}, W_{LE}, E_P and the integrated intensity.

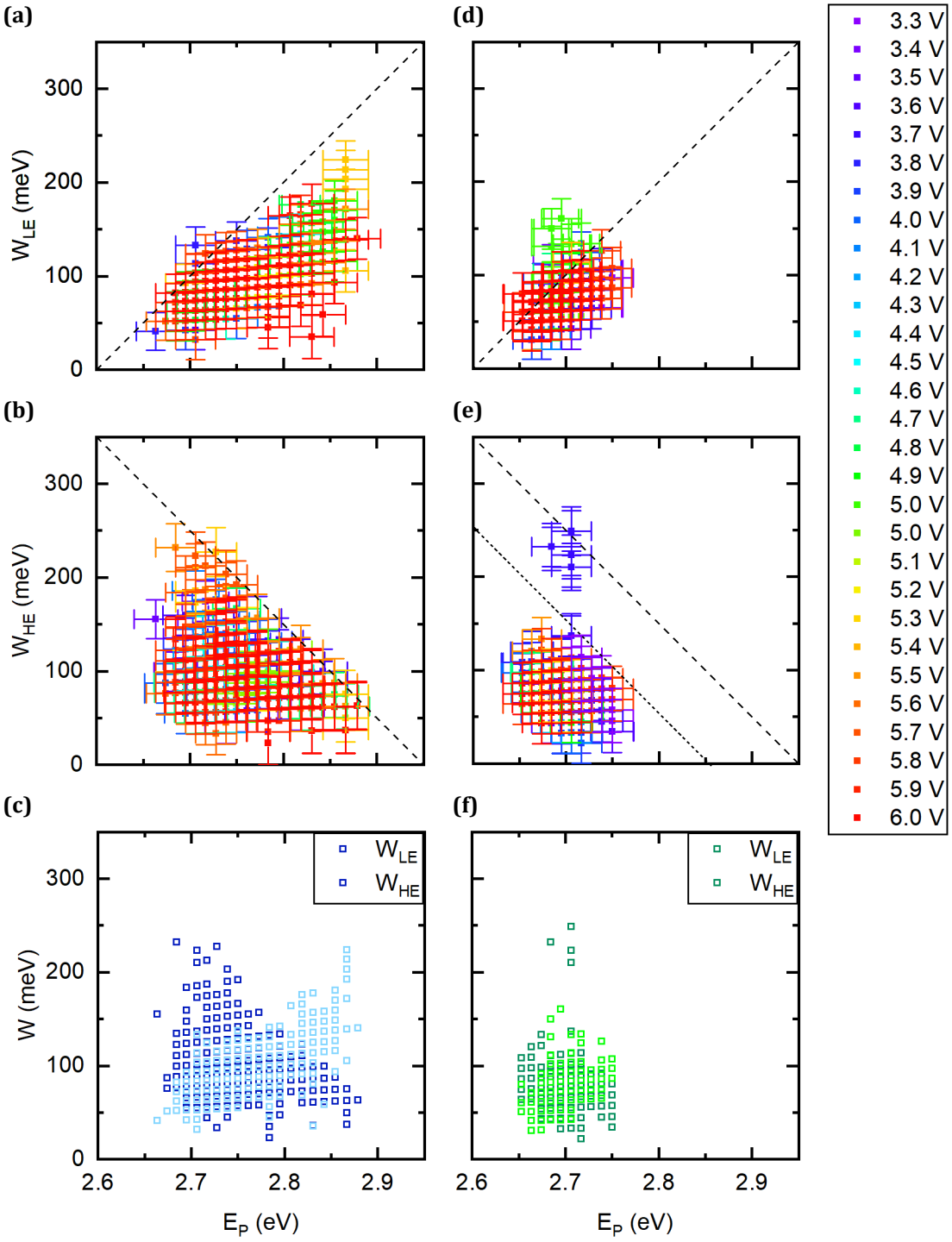

Figure 3.16: Variations of W_{LE} and W_{HE} against E_P for line scans recorded on **(a) – (c)** S10 and **(d) – (f)** the S90 samples with applied bias varying from 3.3 V to 6.0 V at 20 nA injected current. In **(c)** and **(f)** all data of W_{LE} (light colors) and W_{HE} (dark colors) are superimposed. The dashed lines have a slope 1 in **(a)** and **(d)** and a slope -1 in **(b)** and **(e)**.

These fluctuations are larger on the S10 sample than on the S90 sample. It is also worth to point out that the correlations seen at 2 nA are still observable in this dataset at 20 nA of injected current. The positive correlation between W_{LE} and E_P is particularly striking.

The systematic data analysis described above is applied to a whole dataset of line scans recorded at different bias voltages and different positions on both samples. **Figure 3.16** shows the values of W_{LE} and W_{HE} as a function of E_P.

We note a red-shift of about 100 meV of the whole dataset of S10 compared to the dataset taken at 2 nA. This shift could be due to an extrinsic shift in In concentration or to an effect of the tunneling current itself. The width of the energy range of representation of the datasets is nonetheless kept identical compared to the one of **Figure 3.14**.

Despite the quantitative differences, the data clouds exhibit a very similar distribution at 20 nA injected current to that at 2 nA, especially for the S10 sample. The values of E_P, W_{LE} and W_{HE} are spread over about 210 meV.

The Pearson correlation coefficient of S10 sample, for W_{LE} and W_{HE} against E_P are:

$$r_{S10,LE,20\,nA} = 0.7671,$$

$$r_{S10,HE,\,20\,nA} = -0.0507.$$

The strength of the positive linear correlation of E_P and W_{LE} for S10 is therefore much stronger than at 2 nA. For W_{HE} against E_P, however, only a weak negative correlation coefficient at the level of significance is retrieved which could be due to the off-axis data points at lower W_{HE} (50 meV to 120 meV) and E_P (2.65 eV to 2.8 eV).

The results of the data treatment for S90 shown in **Figure 3.16 (d-f)** reveal a more concentrated dataset for both W_{LE} and W_{HE} versus E_P. The values of E_P are spread only over 90 meV, while those of W_{LE} and W_{HE} are spread over 130 meV and 110 meV, respectively (excluding the extreme outlying points). Nonetheless, the Pearson correlation coefficient still shows a positive correlation between W_{LE} and E_P and a negative correlation for W_{HE} and E_P:

$$r_{S90,LE,20\,nA} = 0.4830$$

$$r_{S90,HE,\,20\,nA} = -0.1894\,.$$

3.4 A model accounting for energy relaxation and transport

The correlation observed between the values of E_P and those of W_{LE} and W_{HE} implies that spectra with high peak energies E_P are broadened towards the low energy side, while spectra with low peak energies E_P are slightly broadened towards the high energy side. This latter characteristic is less pronounced since the plot of W_{HE} against E_P shows a concentration of data points towards low energies and a cut-off to higher energies. We conjecture that this behavior is a signature of energy relaxation and in-plane transport in the QW before electrons recombine with holes.

Assuming the local injection proven by the emission of single localized states, two different scenarios are possible. On the one hand, if the carrier is injected inside a region with high eigenenergy, it may recombine in this region but has also a probability to transfer to lower energy regions and recombine there. This leads to a broadening in the spectra towards the low energy side. On the other hand, if the injected region has a low eigenenergy compared to its surrounding, the electrons will preferentially relax their excess energy in that region before recombining and

will have a smaller probability to transfer to and recombine in regions of higher eigenenergy. These dynamics lead to sharper low energy side of the spectra with a slight high energy broadening. A sketch of this behavior is shown in **Figure 3.17**.

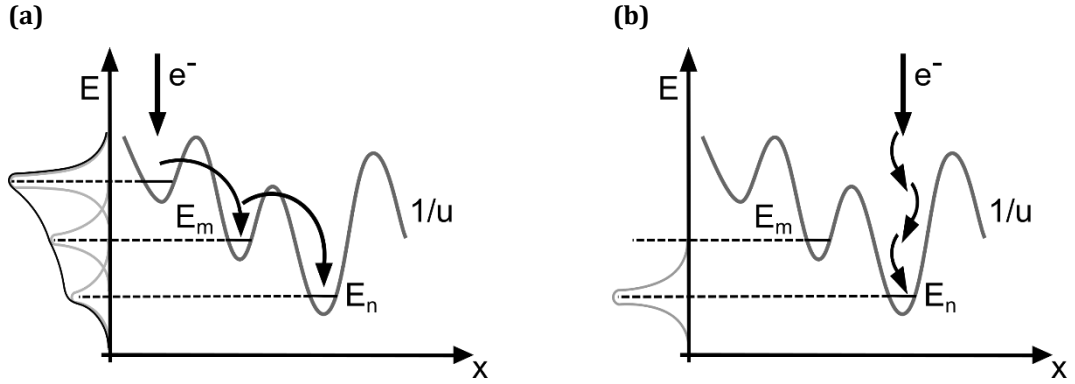

Figure 3.17: Sketch of the in-plane transport of electron injected in the effective potential 1/u of the LL theory before recombining for **(a)** a high energy region and **(b)** a low energy region.

The transport from one region to another is done via phonon-assisted tunneling or hopping. The emission spectrum itself is peaked at the local effective bandgap of the localization region with an intrinsic broadening of a few tens of meV at 300 K (as reported for GaN quantum dots [54]). The recorded spectrum at one position is therefore a convolution of the contributions of all the connected regions weighted by the probability of transferring from one region to another.

To capture this carrier transport behavior, Jean-Marie Lentali introduces, in his dissertation "Carrier Localization in Nitride-Based Semiconductor Alloys", a model based on the master equation formalism with time-evolution of the occupation f_n of the electronic state $|n>$ in an effective potential map from the LL theory [44]:

$$\frac{\partial f_n}{\partial t} = \sum_{n \neq m, electrons} (f_m(1-f_n)\Gamma_{mn} - f_n(1-f_m)\Gamma_{nm}) - f_n \sum_{k, holes} \beta_{nk} f_k^h,$$

where Γ_{mn} is the probability to transfer from region m to n. The second sum contains a sink term corresponding to the recombination between the electron state n with all possible overlapping hole states k. It is defined as:

$$\beta_{nk} = \frac{e^2 n\left(E_n^e + E_k^h + E_g\right)}{m_0^1 c^2 \hbar^2 \epsilon_0} I_{n,k} |p_{cv}|^2,$$

with $I_{n,k}$ being the overlap between the states n and k, E_n^e the energy of the electron state, E_k^h of the hole state and E_g the local bandgap. The simulated spectra of the in-plane transport and carrier recombination are shown in **Figure 3.18** for 2 different injection regions. In **Figure 3.18 (a)** and **(c),** the single contributions of the localization regions to which the electrons are transfer to are plotted. In **(b)** and **(d),** we show the respective sum of the single contributions. These theoretical results reproduce well the observed asymmetric broadening towards the low energy side of the experimental spectra.

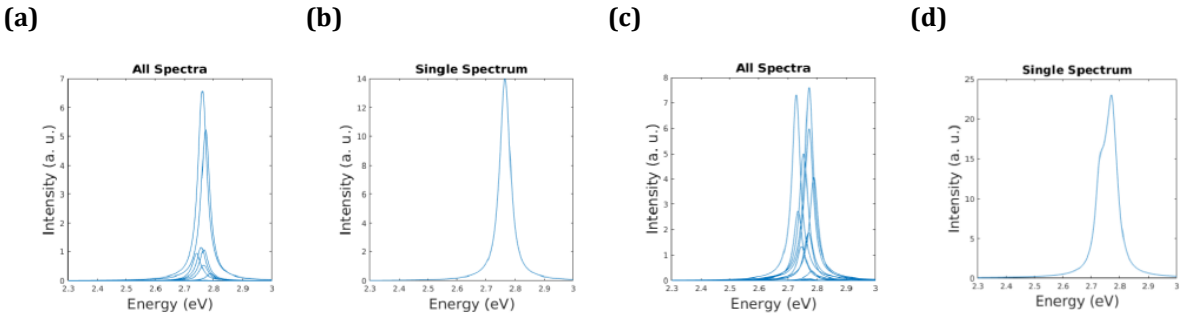

Figure 3.18: Preprint version from [44] of simulated recombination **(a)** (respectively **(c)**) individual contributions from localized states, **(b)** (respectively **(d)**) corresponding total emission spectrum (=single spectrum).

3.5 Dependence of the local STL spectrum on tunneling parameters

Here above, we have shown that the STL spectrum exhibits fluctuations at the scale of a few nanometers which are consistent with the expected carrier localization effects induced by the intrinsic compositional disorder of the ternary alloy QW. The characteristic features of the emission from localized states (single state emission, correlations between peak energy and line shape) are observed in all the explored experimental conditions: different injection layer thickness (10 nm and 90 nm), tunneling bias and current. The impact of the localization effects may change with the above parameters but the qualitative trends remain similar.
It is, however, interesting to investigate the influence of the experimental conditions on a given local tunneling electroluminescence spectrum. We have thus performed an experiment which consists in keeping the position of tip constant and recording the local tunneling electroluminescence spectrum while varying the injection parameters. In detail, we varied the tunneling bias at constant tunneling current (**Figure 3.19**) and the tunneling current at constant tunneling bias (**Figure 3.20**) at the same injection position. The measurements were performed on the S10 sample. For each set of tunneling parameters (bias, current), the spectrum is recorded at least three times to assure the reliability of each parameter set. Moreover, the measurements for a given set of parameters (5.0 V, 16 nA) are repeated at three different steps of the experiment to control the stability and reproducibility of the experiment. The corresponding spectra are plotted in blue. The fact that the line shape of these spectra is recovered throughout the measurement is a good indication for the stability of our setup.

Figure 3.19 shows a sequence of spectra recorded with a fixed tunneling current of 16 nA while decreasing the tunneling voltage from 5.0 V to 4.0 V, in steps of 0.1 V. For all voltages, the spectra exhibit a broad emission band peaked at 2.7 eV and a narrow line peaked at 2.85 eV, tagged by a vertical dashed line. Above 4.3 V, the peak intensity of the narrow high-energy line is larger than the one of the broad low-energy emission band. Below 4.3 V, the intensity of the narrow high-energy line diminishes relative to the broad band emission intensity. When increasing the bias up to 5.0 V again, the high-energy narrow line does not recover its initial intensity. This change in the relative intensity of the two contributions might be due to a change in the injection conditions or to minimal change in the tip position.

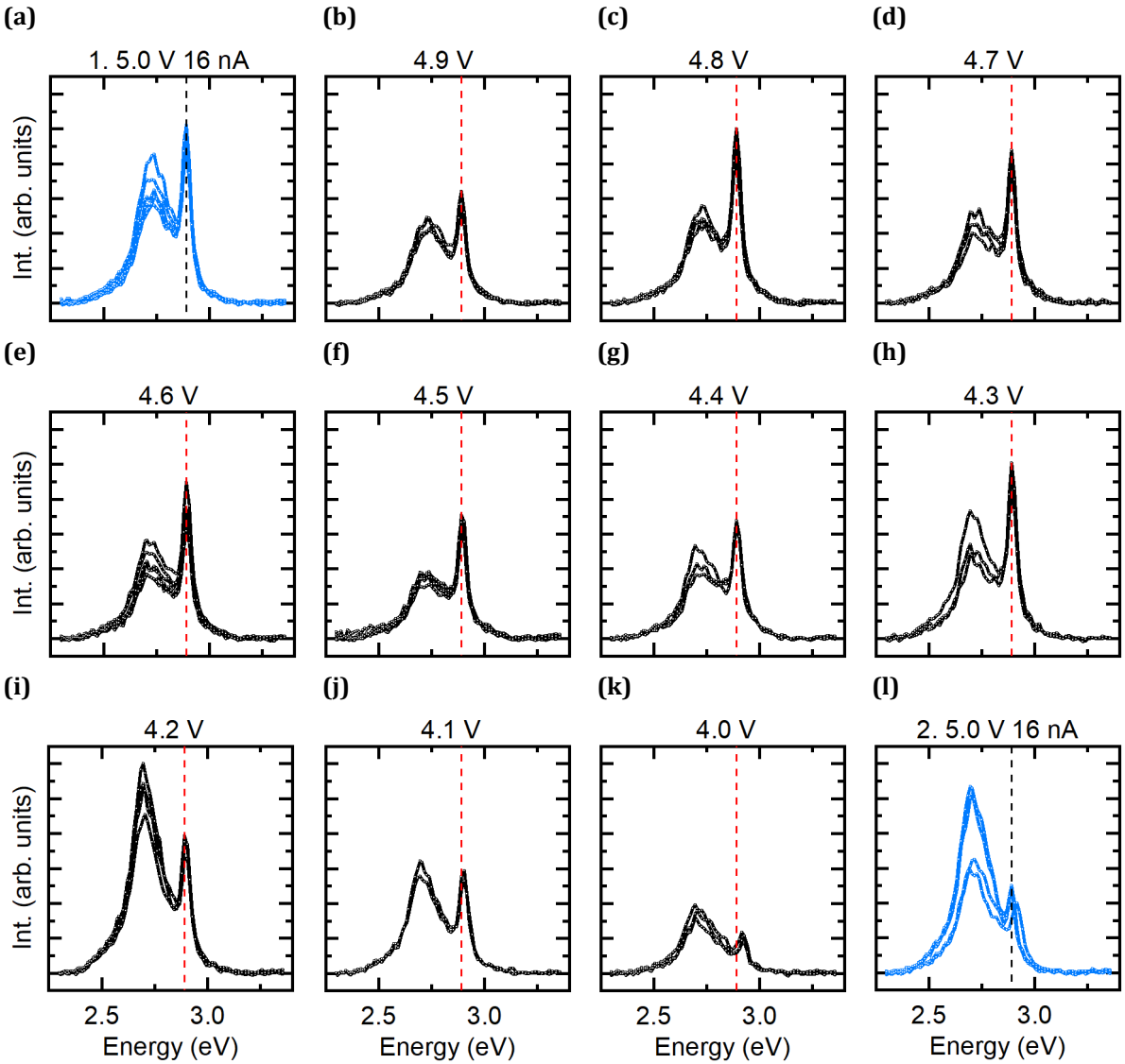

Figure 3.19: Local tunneling electroluminescence spectra recorded at the same tip position and tunneling current of 16 nA, for decreasing values of the tunneling bias from 5.0 V to 4.0 V, in steps of 0.1 V. On each graph, a vertical dashed line singles out a narrow peak appearing on the high energy side of the spectrum.

Figure 3.20 shows the spectra recorded at the same tip position and 5.0 V tunneling bias for different values of the tunneling current, increasing by a factor of 2 from 1 nA up to 32 nA. At low current, only the broad low-energy emission band is observed. The narrow high-energy line starts to show up only at the quite large injected current of 8 nA. At 16 nA, its intensity recovers a similar value relative to the broad low-energy band that was observed at the end of the bias variation sequence of **Figure 3.19**. At 32 nA, the spectrum intensity increases but the relative intensity of the low- and high-energy contributions remains similar to the one at 16 nA. This is confirmed by the data analysis of the local tunneling electroluminescence spectra shown in **Figure 3.21**. In contrast with the variation of the relative intensity of the two contributions observed when varying the tunneling bias voltage, the disappearance of the narrow high-energy lines at low current indicates a change in the electronic process dynamics, depending on the current density.

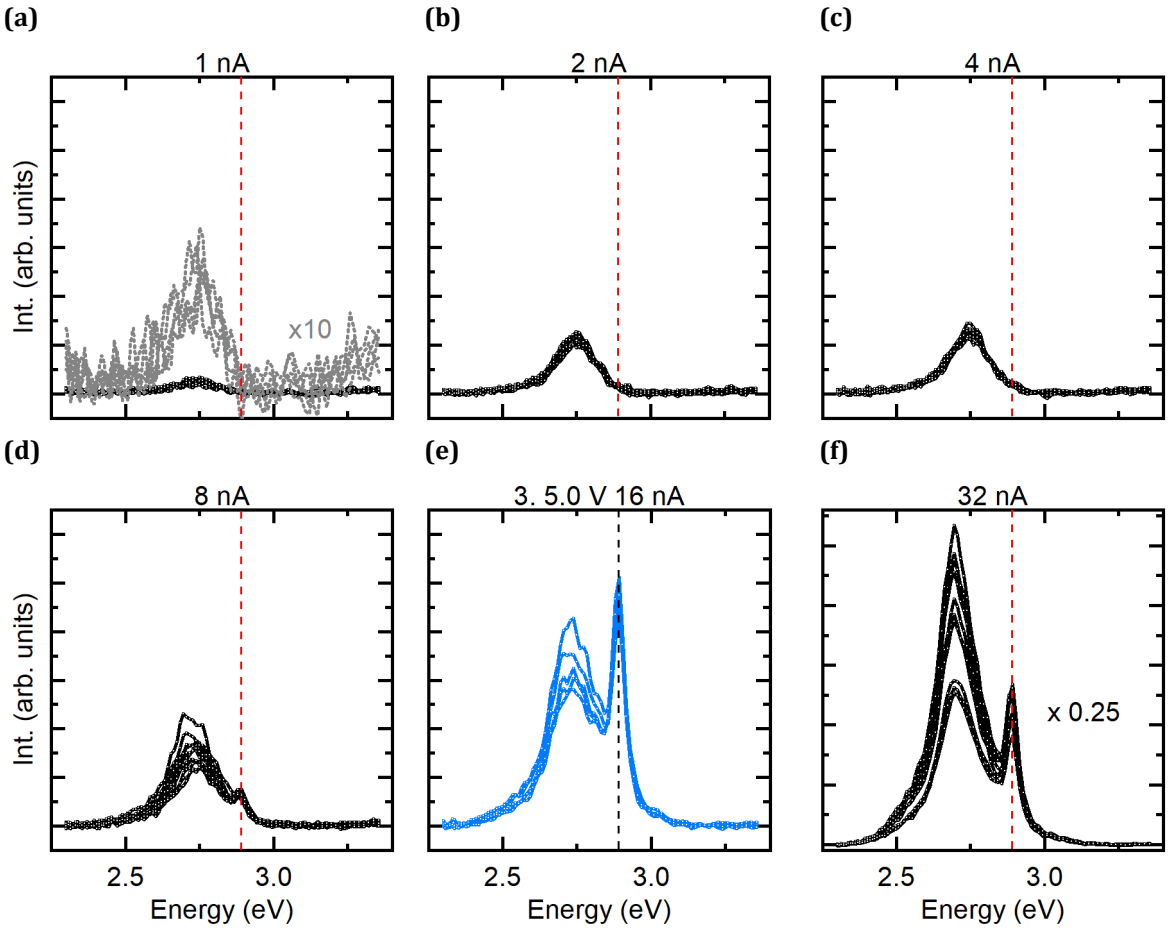

Figure 3.20: Variation of the local tunneling electroluminescence spectrum as a function of the tunneling current injected at the same tip position with constant tunneling bias voltage of 5.0 V. The narrow high-energy peak is tagged by a vertical dashed line.

Furthermore, we can extract at least to different regimes of injection from the data analysis in **Figure 3.21**, one regime at tunneling current below 8 nA and the other above 8 nA. In these regimes the FWHM and the integrated STL luminescence intensity exhibit strong changes and the separated high energy contribution is observed. The appearance of the separated high energy contribution could be an effect of carrier crowding and repulsive carrier behavior inducing a bottleneck to transfer to localization regions with lower eigenenergy. Repulsive carrier behaviors are also seen by Aleksiejūnas et al. [73] in non-monotonous changes of the diffusivity with increasing photoexcitation. There they argue that this is the signature of efficient hole transport via percolation paths arising from the compositional disorder and that the decreased diffusivity with excitation can reflect the effect of Coulomb blockade of these paths.

To identify the exact underlying mechanism in our system, we are currently working on a theoretical model to describe the perpendicular transport as a function of the tunneling bias and tunneling current. Via this model, we would like to find a description of the carrier density and energy of the electrons that reach the QW.

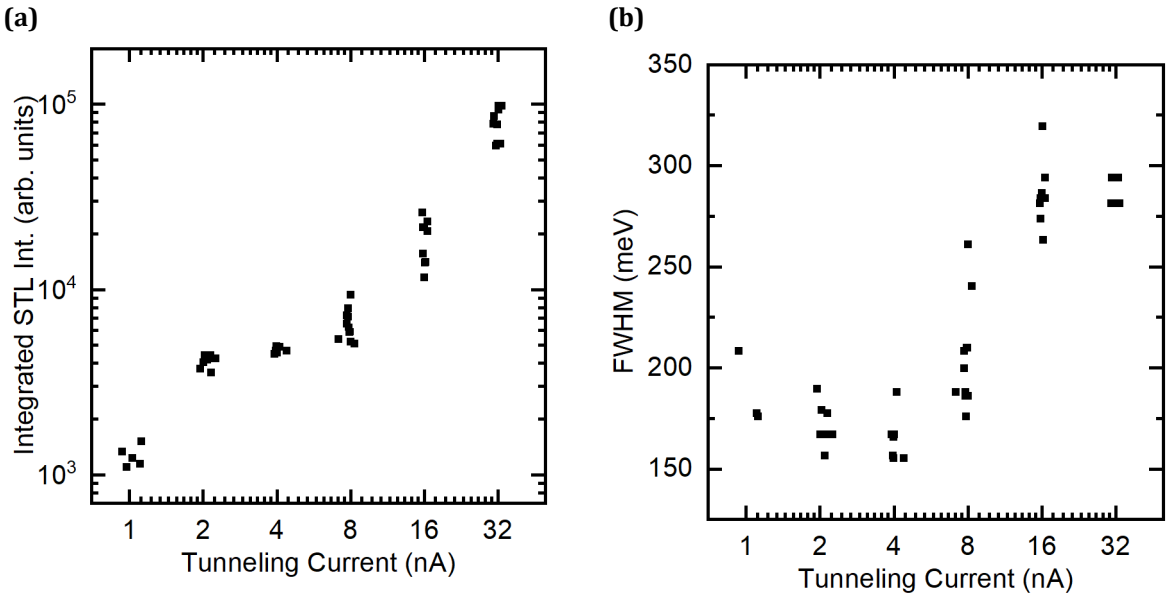

Figure 3.21: Data analysis of the current dependence at one spot spectra shown in **Figure 3.20**. **(a)** Integrated STL intensity against tunneling current. **(b)** FWHM against tunneling current.

3.6 Further investigations on single localized state emission

Throughout the measurements on the S10 sample with different conditions, e.g., tunneling current and tunneling bias (see above), we have observed emission from single localized states. The results shown in this section were obtained on the S10 sample with a spectral resolution of 26 meV. A selection of such spectra exhibiting single state emission peaks is shown in **Figure 3.22**.

In all of the experiments that we performed, we observed mainly two instances of such single localized state emission. First, an isolated narrow peak at high energy with a separated broader emission at lower energy. This emission line width is frequently observed. A selection of such spectra is shown in **Figure 3.22 (a) – (c)**. Notable, is the high intensity of the observed spectra. Second, a main narrow emission line with at least one contribution at lower intensity. These contributions can also exhibit narrow line widths. A selection of such spectra is shown in **Figure 3.22 (d) – (i)**.

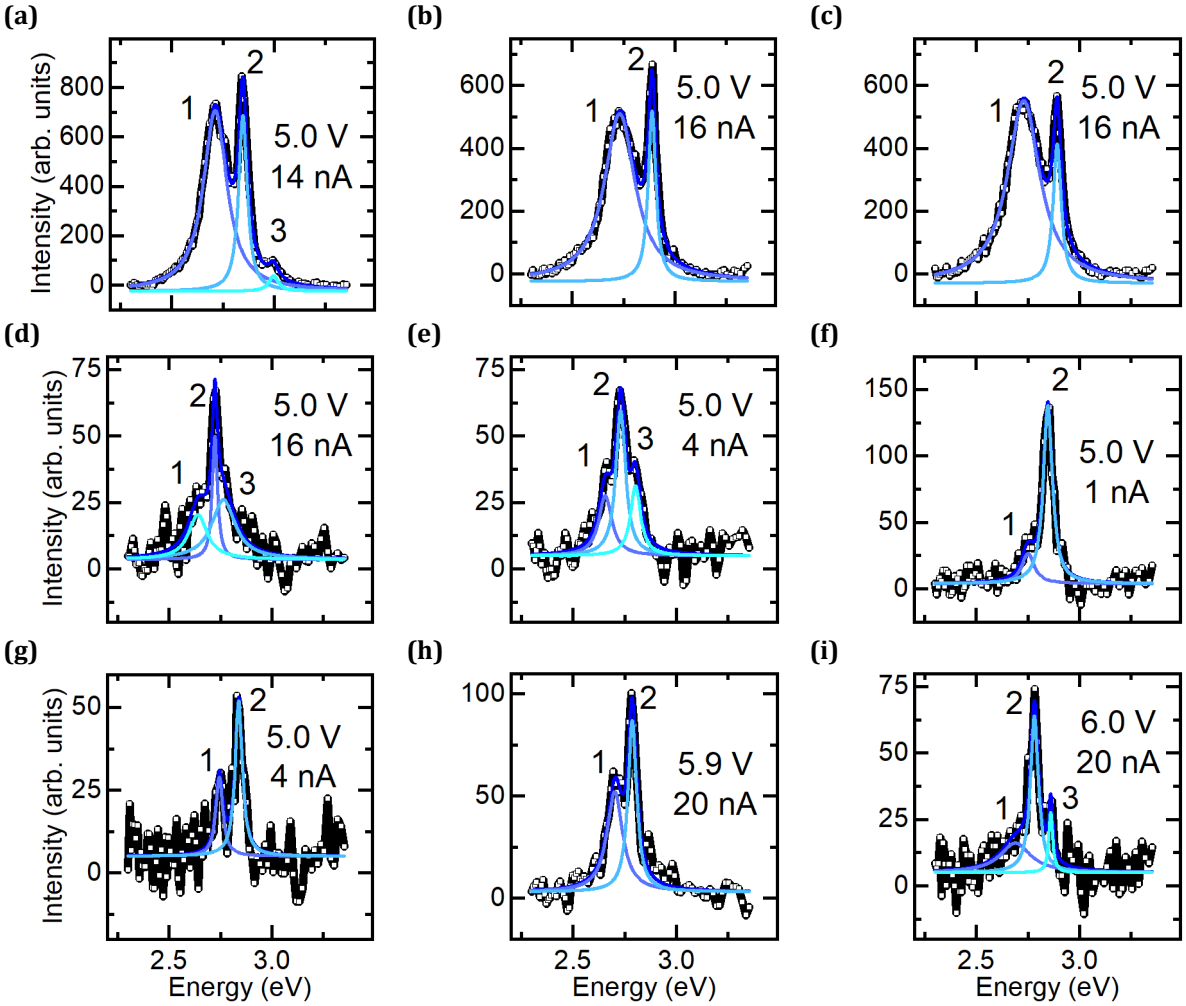

Figure 3.22: Selection of spectra with narrow emission peak from different measurement sets on the S10 sample. **(a) – (c)** Isolated narrow high energy peak separated from a broad low energy emission band. **(d) – (f)** Main narrow emission line with at least one (narrow) contribution at lower intensity.

To reveal the different contributions of these emission spectra, a multiple-peak Lorentzian fit is performed on each spectrum. The details of each fit can be found in **Table 3.1**. The absolute FWHM is derived from the Fourier transform approach taking into account the dispersion of the spectrometer (= 7 nm/mm), the slit width (= 600 µm) and the resolution [74].

Table 3.1: Parameters of the multi peak Lorentzian fit of the spectra shown in **Figure 3.22** and derived absolute FWHM.

Graph label	Peak No	E_P (eV)	Measured FWHM (eV)	Derived FWHM (meV)	Area (arb. units)	Offset (arb. units)
(a)	1	2.712 ± 0.001	0.141 ± 0.003	138.1	161.2 ± 3.2	-24.4 ± 3.1
	2	2.848 ± 0.001	0.050 ± 0.001	42.9	56.0 ± 1.6	
	3	2.998 ± 0.005	0.055 ± 0.018	49.0	5.4 ± 1.4	
(b)	1	2.731 ± 0.001	0.181 ± 0.004	179.4	152.0 ± 3.5	-23.9 ± 2.8
	2	2.888 ± 0.001	0.045 ± 0.002	36.1	37.8 ± 1.3	
(c)	1	2.729 ± 0.001	0.192 ± 0.004	190.2	175.0 ± 3.5	-29.5 ± 2.7
	2	2.892 ± 0.001	0.047 ± 0.002	39.7	33.0 ± 1.3	
(d)	1	2.640 ± 0.016	0.110 ± 0.048	106.7	2.9 ± 2.0	3.6 ± 1.2
	2	2.723 ± 0.002	0.030 ± 0.015	15.6	2.2 ± 1.5	
	3	2.765 ± 0.041	0.138 ± 0.062	135.4	4.9 ± 4.0	
(e)	1	2.656 ± 0.008	0.078 ± 0.024	73.6	2.8 ± 0.9	4.9± 0.7
	2	2.731 ± 0.003	0.057 ± 0.012	50.4	4.9± 1.2	
	3	2.803 ± 0.005	0.060 ± 0.018	54	2.5 ± 0.8	
(f)	1	2.751 ± 0.008	0.073 ± 0.029	67.9	2.6 ± 0.9	3.9 ± 1.0
	2	2.847 ± 0.001	0.053 ± 0.004	45.8	11.1 ± 0.7	
(g)	1	2.745 ± 0.004	0.041 ± 0.013	31.7	1.5 ± 0.4	5.1 ± 0.7
	2	2.839 ± 0.002	0.042 ± 0.007	32.9	3.1 ± 0.4	
(h)	1	2.702 ± 0.003	0.092 ± 0.012	88.5	7.1 ± 0.9	3.1 ± 0.7
	2	2.786 ± 0.001	0.050 ± 0.005	42.9	6.6 ± 0.6	
(i)	1	2.689 ± 0.037	0.178 ± 0.103	176.3	3.1± 2.2	5.0 ± 1.2
	2	2.781 ± 0.002	0.047 ± 0.009	38.9	4.3 ± 0.9	
	3	2.861 ± 0.003	0.023 ± 0.014		0.8 ± 0.3	

The spectrum shown in **Figure 3.22 (h)** is especially striking, where both emission peaks (separated by 94 meV) exhibit a line widths comparable to the emission from nitride quantum dots [54]. We observed a similar behavior in a current dependent measurement on a fixed local

injection area (**Figure 3.23**). In this measurement we altered the tunneling current from **(b)** 8 nA to **(c)** 16 nA to **(d)** 32 nA.

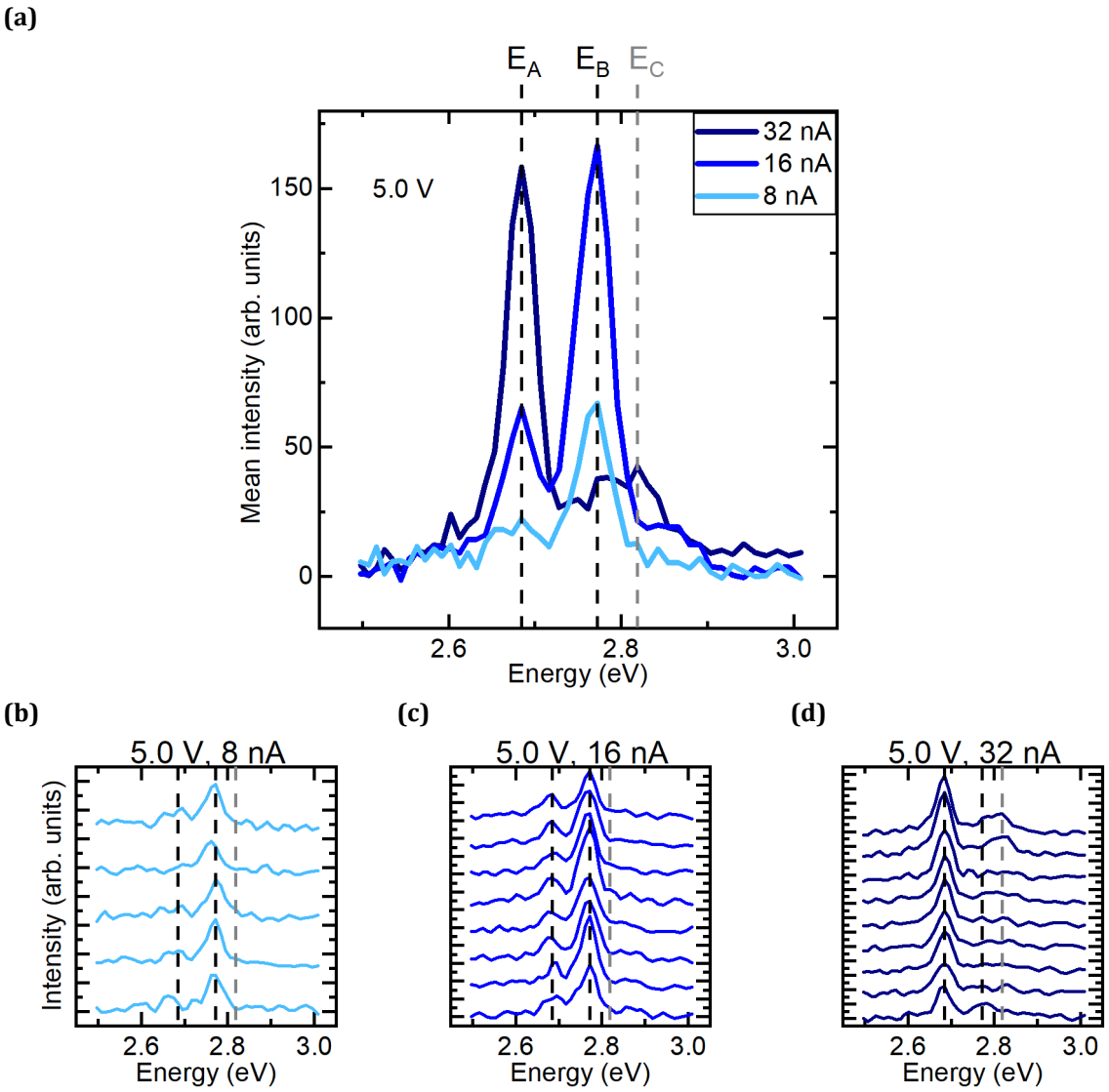

Figure 3.23: (a) Averaged STL emission spectra of the spectra shown in **(b) – (d)** at 5.0 V with 8 nA, 16 nA and 32 nA. Position of peak energy marked and labeled E_A = 2.684 eV, E_B = 2.772 eV, E_C = 2.819eV.

Changing the tunneling current from 8 nA to 16 nA, we observe no change in the main peak emission (position E_B) and the satellite peak (position E_A) energy. Only the intensity between the two emission peaks changes between 8 nA and 16 nA tunneling current. Applying, however, 32 nA the main emission shifts to lower energy. In fact, it switches exactly to position E_A which was observed as a low intensity peak before. The emission spectra at 32 nA also show a second peak labeled C at an energy E_C slightly higher than E_B seen for 8 nA and 16 nA. We analyzed the spectra of this data set with our dedicated data treatment (see **Appendix A**) and plot the results in **Figure 3.23**. Note that, not all peaks exhibit an intensity higher than threshold of 40 counts. These peaks are therefore not captured by the analysis.

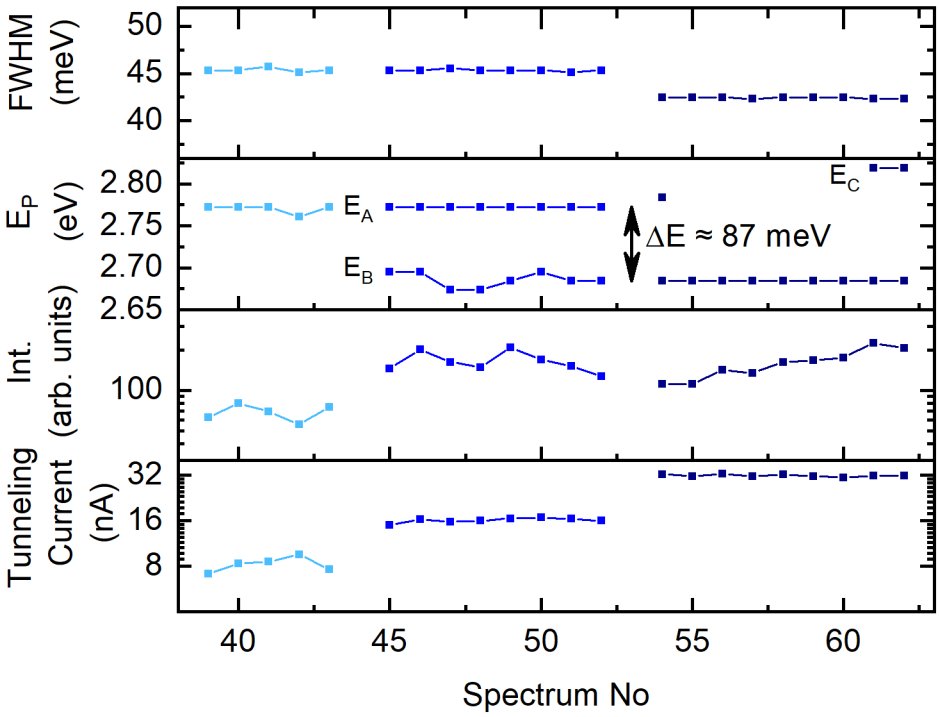

Figure 3.24: Evaluation of the emission spectra shown in **Figure 3.23** in tunneling current, Intensity (Int.), peak energy (E_P) and FWHM (W_{LE}+W_{HE}) from data treatment explained in **Appendix A**.

The main peak E_P shifts by ~87 meV from 2.772 eV to 2.819 eV when changing the tunneling current from 16 nA to 32 nA. The FWHM, however, is not affected. The measured FWHM is in between 43 meV to 46 meV. Therefore, the actual FWHM (accounting for the spectral resolution) is between 34 meV and 38 meV. Hence, both emissions at the different tunneling currents stem from a single localized state(s). The origin of these remarkable emission spectra is, however, up to debate. It could emerge from:

a) *two* neighboring highly isolated states due to a rare configuration of the effective confining potential,
   or
b) *one* state exhibiting a bi-exciton behavior.

In case a), it could be that the emissions from these two neighboring highly isolated states are correlated to each other by level repulsion / level crossing. In such a configuration quantum mechanics prevents the spatial overlap of localized eigenstates to be close to each other in energy and leads to splitting in (many) quasi-degenerate states [75,76]. To confirm this prediction a statistical analysis using an auto-correlation function as in Intoni et al. [75,76] could be used. This endeavor would, however, need a much larger amount of data.

The case b) of bi-excitons (or even multi-excitons) would be a bound state of two (respectively multiple) electron–hole pairs [77]. This phenomenon would be a many body localization effect. To confirm this hypothesis we would need to perform photon correlation measurements and low temperature measurements to reduce the transport via phonons on such emission spectra [78].

3.7 Conclusion and discussion

Summarizing the findings above, STL has shown to be a novel approach to probe the effects of localization stemming from the disorder of alloy atoms. The evidence of single localized state emission at room temperature shown in **Figure 3.8 (d)** and **Figure 3.9** is particularly striking. The resolved narrow emission line is as narrow as the emission from III-nitrides quantum dotes at the same temperature [54]. The signature of the single state emission vanishes over a distance of 10 nm. This length is an indication of the main transport process inside the QW before recombining and implies a carrier lifetime in the QW of the same order of the transfer time between localized states. David et al. measured a total lifetime in InGaN QWs of about 300 ps [79], which is the same order of magnitude of transfer time in between neighboring localized states by phonon-assisted tunneling deduced from GaAs coupled QWs [80,81]. The diffusion length inside InGaN QWs measured via other techniques, e.g., micro-photoluminescence seems contrary at first sight [82,83]. These techniques, however, do not have access to the intrinsic disorder inside the QW and, therefore, probe transport phenomena on much larger scales. Nevertheless, in GaAs QWs the coexistence between diffusing and non-diffusing transport behavior due to interface disorder could be already be shown [84].

In the following back-of-the-envelope calculation, we estimate the carrier density of injected electrons via:

$$\rho_{inj} = \frac{j \cdot \tau}{e^-}.$$

With the current density being $j = \frac{I}{\pi \cdot r^2}$, an estimated broadening of the radius of the injection cone by r = 5 nm, I = 2 nA (respectively 20 nA) and lifetime $\tau = 10^{-10}$s (discussed above), we obtain:

$$\rho_{inj} \approx 1.5 \times 10^{12}\mathrm{cm}^{-2},$$

for 2 nA, and

$$\rho_{inj} \approx 1.5 \times 10^{13}\mathrm{cm}^{-2},$$

for 20 nA. This density of the injected electrons is comparable to the estimation of localized states:

$$\rho = \frac{1}{(5\mathrm{nm})^2} \approx 4 \times 10^{12}\mathrm{cm}^{-2}.$$

Assuming that all the injected electrons reach the QW, at 2 nA tunneling current every state is populated by about 1 electron whereas by more than one at higher tunneling current.

The emitted luminescence spectra along a line scan reveal a significant variation of the line shape on the step size of 5 nm on S10 at 2 nA.
Smaller changes in the peak position E_P, W_{LE} and W_{HE} can also be observed at higher tunneling current and on the S90 sample. Using a dedicated data treatment, a positive linear correlation for W_{LE} versus E_P and negative linear correlation for W_{HE} versus E_P is observed. The mechanism of this correlation is explained via a transport model between nearby localized states. The same mechanism also indicates the coexistence of localized and delocalized state emission.

Nevertheless, we are able to observe disorder induced localization effects also from summed emission spectra thanks to our dedicated data treatment.

We analyze the applied bias voltage and tunneling current influence on the emission spectrum and find that only the change of tunneling current significantly impacts the line shape. This behavior could be ascribed to a change in carrier dynamics, e.g., Coulomb blockade.

The further study of single localized state emission suggests an even more complex behaviors as level repulsion or many-body effect.

We, therefore, suggest supplemental measurements of the carrier dynamics on different sample structure and at different temperature.

4 Preliminary results on future research directions

In this chapter, we present preliminary results on different subjects related to localization effects in nitrides and their study by STL. We look into:

- *samples containing two QWs at different depths below the surface to probe the perpendicular transport of injected electrons towards the QWs and to evaluate the dependency of the STL resolution on the distance of the QW to the surface;*

- *low temperature effects since temperature is expected to impact transport through phonon-assisted hopping between localized states and recombination through non-radiative processes;*

- *samples produced within academic and industrial facilities since an optimized industrial growth process should provide the highest material quality;*

- *n-type samples to probe the localization of holes which is stronger than the one of electrons, according to theoretical predictions.*

4.1 DQW structures for the study of perpendicular transport and STL resolution

To study perpendicular transport and STL resolution we chose a double quantum well (DQW) structure. The detailed sample structure is shown in **Figure 4.1 (a)**. It was grown by metalorganic chemical vapor deposition (MOCVD) on a patterned sapphire (0001) substrate at the facilities of the University of California in Santa Barbara by Abdullah Alhassan. The first InGaN QW (referred to as QW1 in the following) is separated from the surface by a GaN three-layer stack with a total thickness of 30 nm, consisting of an unintentionally doped (UID) spacer, a p-doped layer and a p+-overdoped cap. QW1 is separated from the deeper QW (referred to as QW2 in the following) by an UID 100 nm GaN spacer layer. The two QWs have different In concentrations: 18% for QW1 and 25% for QW2. Their emission spectra are thus expected to be separated by about 200 meV at 2.7 eV for QW1 and 2.5 eV for QW2.

The results presented in the following were performed on the Omicron CRYOSXM setup in ambient conditions. The spectrometer resolution is set to 26 meV.

The PL spectrum recorded in-situ with a laser excitation wavelength of λ = 373 nm is shown in **Figure 4.1 (b)**. Although the compositions of the two QWs are nominally chosen to be different, their emission peaks are significantly overlapping. The integrated intensities of their emission peaks differ by about a factor two. If we assume that they absorb about the same amount of light, their radiative recombination efficiencies are similar. A high energy tail which is not seen in the STL spectrum is observed. This tail could, therefore, be an artefact of the PL excitation optics.

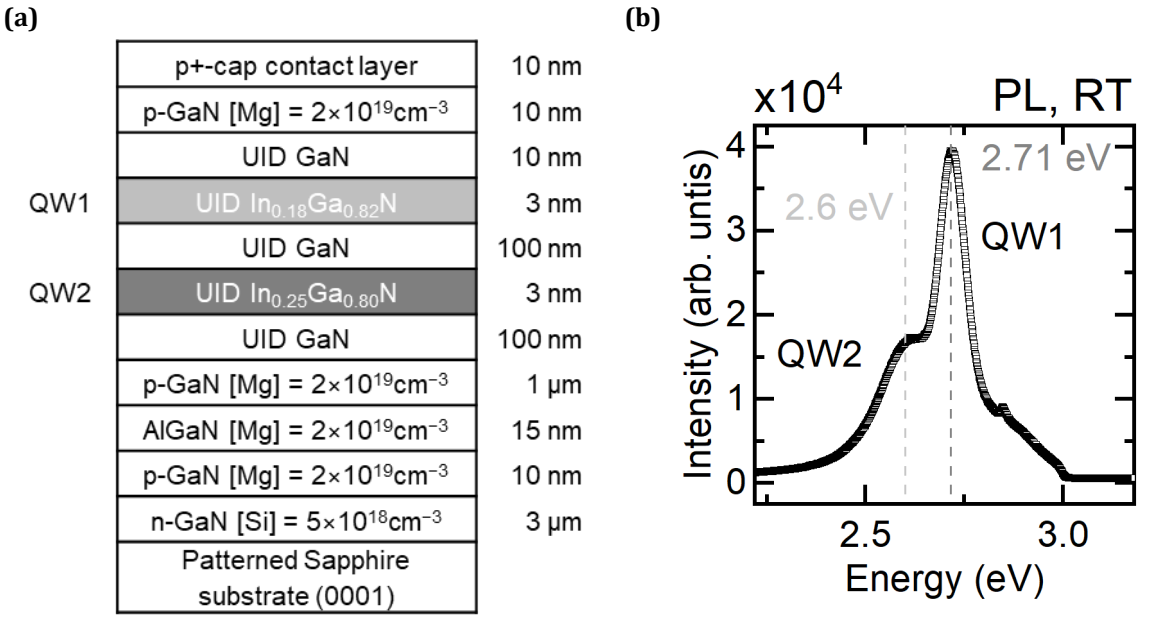

Figure 4.1: (a) Structure of the DQW sample. **(b)** PL spectrum of DQW sample recorded at 300 K with an excitation at λ=373 nm of about 5 mW.

The STL line scan presented shows moderate spatial fluctuations in the DQW spectra (**Figure 4.2**).

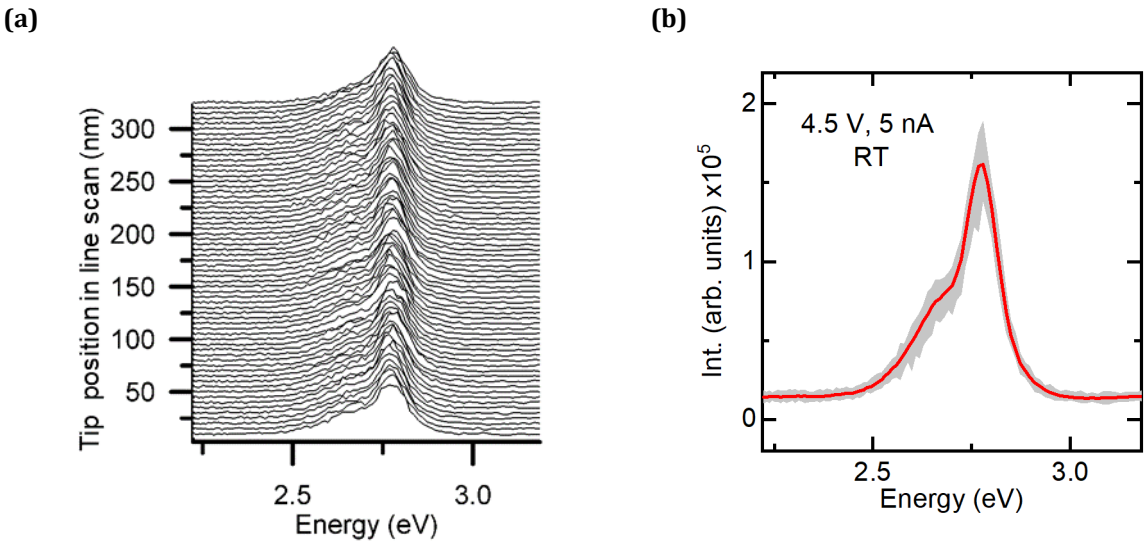

Figure 4.2: (a) STL line scan at room temperature (RT). **(b)** Average spectrum over the line scan spectra (red line) and envelope of maximum and minimum values along the line scan (gray envelope).

Still, the overlap of the two QW spectra prevents to observe the changes in the line shape of each QW emission independently as in the single QW samples S10 and S90 (see **Chapter 3 Results**). A

raw deconvolution of the two contributions can, however, be performed and shows that their relative integrated intensities are close to those of the PL spectrum. This behavior may give some indications of the perpendicular transport through the structure. First, the electron capture efficiency in QW1 is rather low, which is coherent with what is expected on the electrical injection of carriers in MQW LEDs. Second, the electron transport through the 100 nm-thick UID layer is quite efficient and a significant number of electrons reaches QW2. However, we would like to stress that the injection of minority carriers is not equivalent to exciting optically electron-hole pairs directly in the QWs as in PL experiments. Hence, this interpretation has to be carefully evaluated further. Nonetheless, it is a good indication that the DQW approach is relevant to study perpendicular transport. STL resolution should also be provided if the composition of the QWs are different enough to allow separation of the two emission lines. Moreover, the same approach could further be used to study transport and recombination in MQW structures.

4.2 Low temperature STL measurements

STL measurements at low temperature are a cornerstone to study the emission from localized states, in-plane transport by phonon-assisted hopping and perpendicular transport in disordered alloys. Our STL setups enable to work at temperatures down to ~4 K. Here below, we describe the first low temperature STL measurements on the DQW structure described above (see section **4.1**).

The sample is cooled by liquid nitrogen in the Oxford flow chamber of the Omicron CRYOSXM STL setup. The temperature of the exchange gas is controlled via an Oxford ITC temperature controller, that gives access to intermediate temperatures between room temperature (RT) and the liquid cryogen temperature. We performed measurements at five different temperatures: 294 K (RT), 200 K, 175 K, 150 K and 100 K. We acquire at each temperature step, the PL spectrum as well as an STL line scan with tunneling bias of 5.0 V and current of 5 nA. The results are shown in **Figure 4.3**.

The PL spectra of the two QWs are only well separated at 100 K. They are peaked at 2.55 eV for QW1 and 2.70 eV for QW2. Their separation of about 150 meV is slightly smaller than expected from their nominal In concentration. When decreasing the temperature, the emission intensity of QW1 and QW2 increases by about a factor of 4 and 10, respectively. At 100 K, their intensities are comparable and their FWHM are of roughly 55 meV and 80 meV, respectively. A shoulder on the low energy side of the QW2 spectrum is observed.

As for PL spectra, the different contributions in the STL spectra are better resolved at low temperature, including the low energy shoulder on the QW2 peak. We highlight that the line scans show only little spatial fluctuations and that the STL spectra are systematically blue shifted by about 60 meV compared to the PL spectra. In contrast with the PL spectrum, the intensity of the contribution of QW1 to the STL spectrum increases by about a factor of 10 when decreasing the temperature. The intensity of the QW2 line, however, increases by only a factor of 2. The observation of a supplementary intermediate contribution which is not seen in the PL spectrum is remarkable. Indeed, we observe the appearance of several contributions with significant changes in their relative intensities with injected current and tunneling bias. Nevertheless, the interpretation of the change in the STL line shape of the DQW structure at low temperature is not straightforward and requires a more detailed study to extract information on the electronic processes in this structure.

The goal of these experiments was to study perpendicular transport, STL resolution as a function of QW depth, efficiency of carrier capture and recombination in multiple QW structures. Although these preliminary measurements did not allow us to extract quantitative information on these objectives, we showed that STL studies at low temperature with p-doped nitrides are possible. Commonly, the resistivity of too lightly p-doped GaN rises at low temperatures in a way that makes STM measurements very difficult if not impossible [85]. To that respect, the overdoped p+-GaN cap layer is probably a key feature.

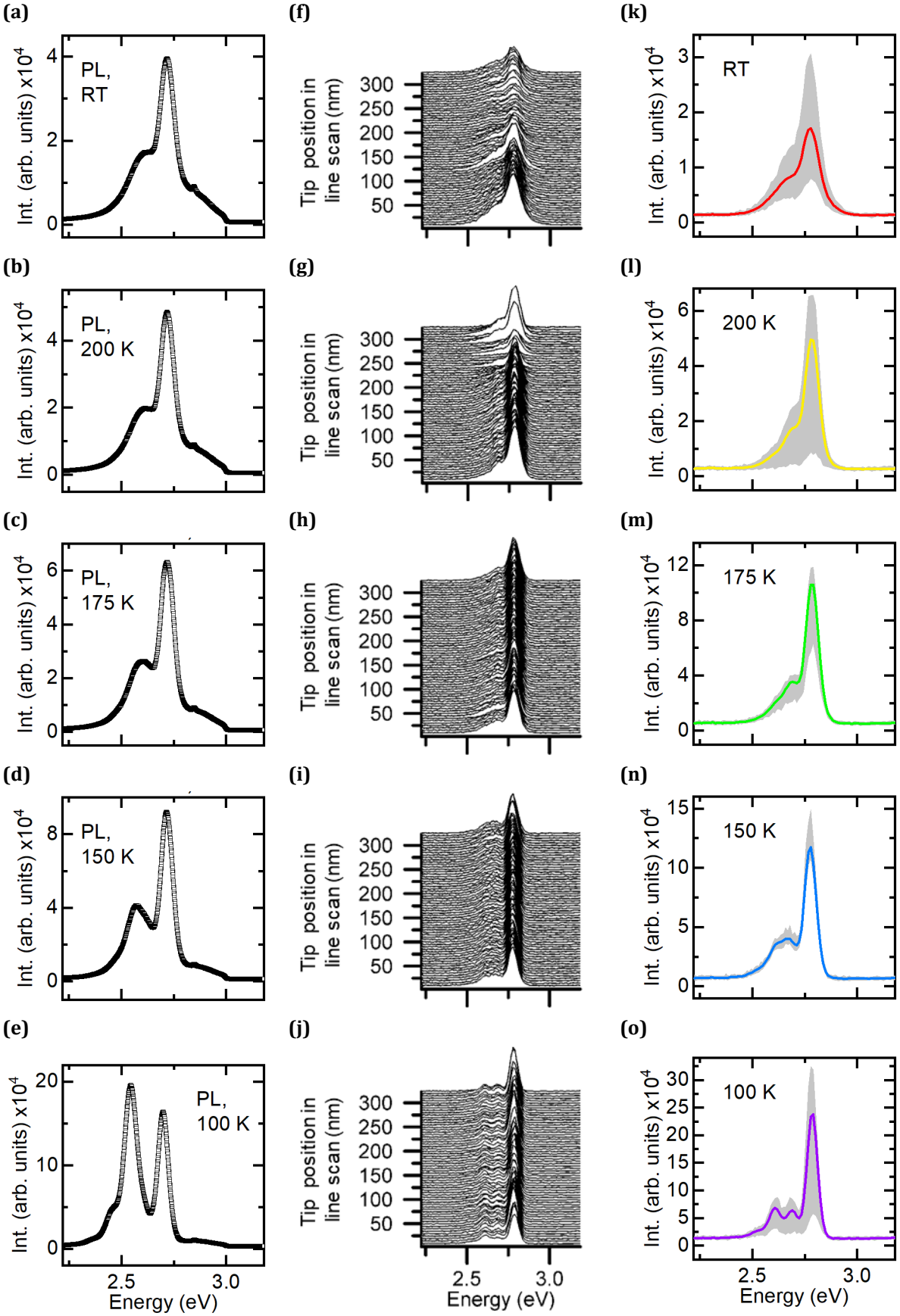

Figure 4.3: Summary of temperature dependent DQW: **(a) – (e)** PL spectra**, (f) – (j)** STL line scan and **(k) – (o)** average value of spectrum in envelope of mean and maximum values at the respective temperature steps of RT, 200 K, 175 K 150 K, 100K.

4.3 Localization effects in nitride heterostructures of industrial standard

Compared to samples fabricated within an academic setting, heterostructures grown in industrial facilities generally have a higher quality due to highly optimized growth processes developed for industrial applications. We received a p-type sample similar to our S10 reference sample grown under industrial standards at Soraa Inc. by Aurélien David's team.

4.3.1 Sample structure and characterization

The sample was grown by MOCVD on a GaN substrate with a roughened backside. First, a 1 µm-thick n-GaN layer with [Si] = $3 \times 10^8 cm^{-3}$ is grown, followed by a n-type superlattice of 70 periods with the same doping and an average In concentration of 2.8%. This specific structure ensures lower defect density, hence a higher quality of the sample. The following p-type stack on top of these layers is almost identical to the structure of the S10 sample (see **Chapter 3.1.1**). The only difference is the In content and the QW thickness which are here 11% and 4 nm, respectively. The full structure of the sample is shown in **Figure 4.4 (a)**.

Before inserting the sample into the UHV STL setup, it was cleaned and passivated as described in **Chapter 3.1.2**. To contact the sample, a 100 nm-thick Au contact was evaporated through a mask on the surface.

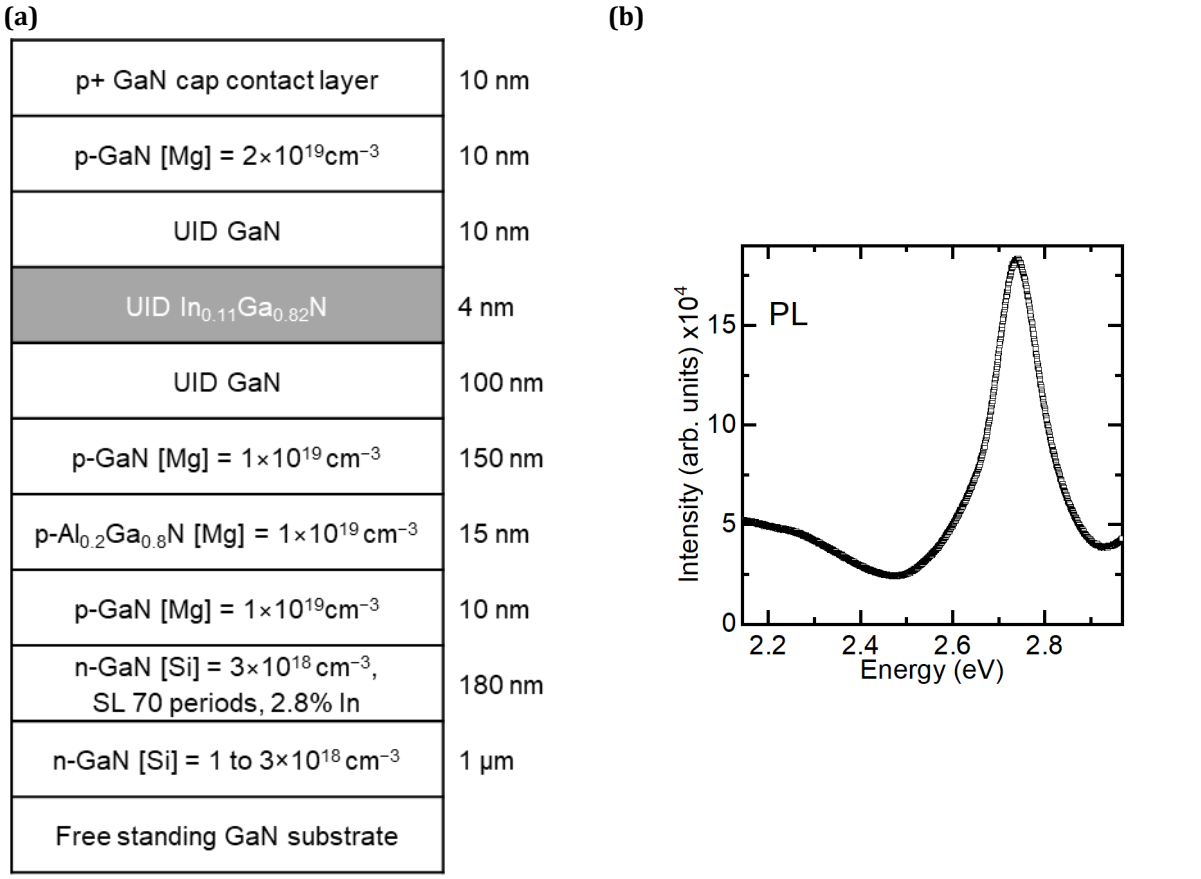

Figure 4.4: p-type SQW InGaN/GaN grown under industrial standard at Soraa Inc. by Aurélien David's team, **(a)** samples structure, **(b)** PL spectrum recorded in-situ under laser excitation with a power of 15 mW and wavelength λ = 378 nm.

Inside the chamber the PL spectrum of the sample was recorded with an excitation laser beam of 15 mW power and wavelength λ= 378 nm. The resulting PL spectrum is shown in **Figure 4.4 (b)**. The emission peak is centered at 2.74 eV. Next to the QW peak, on the low energy side, we observe yellow emission band from deep recombination centers. On the high energy side, we see a parasitic artefact of the excitation. The emission is lower in energy than expected for an alloy of 11 % In content. It is, however, comparable to similar LED structure from the same grower, with 4 nm-thick QWs and slightly higher In concentration of 11.8%, emitting at 470 nm (~2.64 eV) [86]. High resolution X-ray diffraction (HRXRD) measurements confirm the sample structure and approximate In content of 11%. The HRXRD spectrum and data analysis are shown in **Appendix C**.

Scanning tunneling spectroscopy (STS) shows the usual dependency on applied bias voltage and tunneling current evidencing the top GaN layer bandgap (**Figure 4.5**).

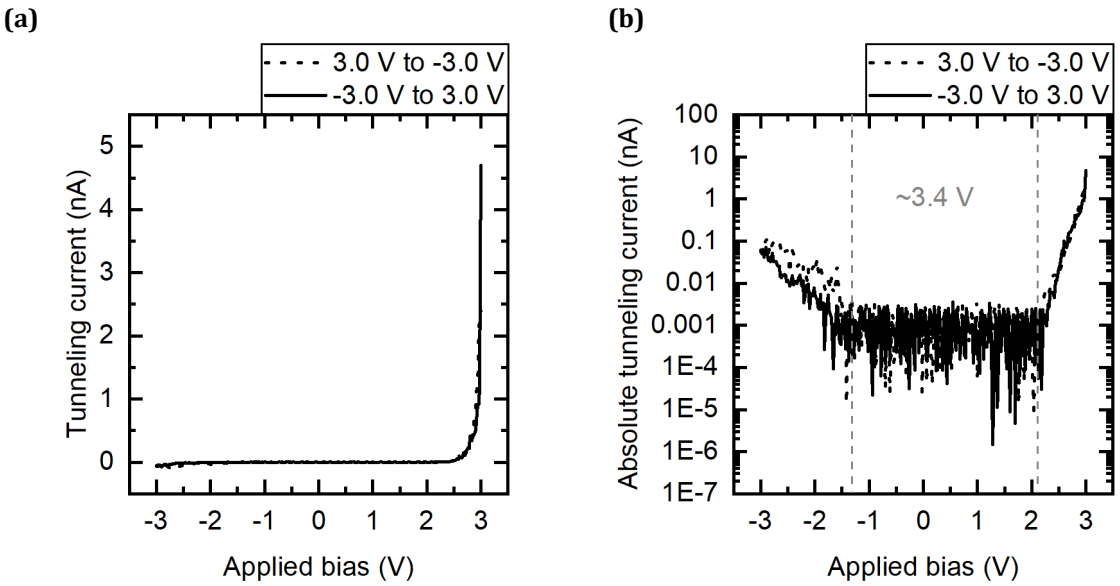

Figure 4.5: STS-IV characteristics of p-type SQW InGaN/GaN grown under industrial standard at Soraa Inc. from 3.0 V to -3.0 V (dotted line) and -3.0 V to 3.0 V (solid line) plotted in **(a)** linear scale, and **(b)** logarithmic scale.

The STM images of the sample surface (**Figure 4.6**) show bi-atomic steps separating 50 nm-wide terraces. This data was recorded with tunneling bias and current of 3.0 V and 1 nA, respectively. A slope-corrected profile (corresponding to the line labeled A on the image) is shown in **(b)** and reveals the atomic step structure with 50 nm-wide terraces. The defect density is very low. A zoom on a V-pit is shown in **(d)**.

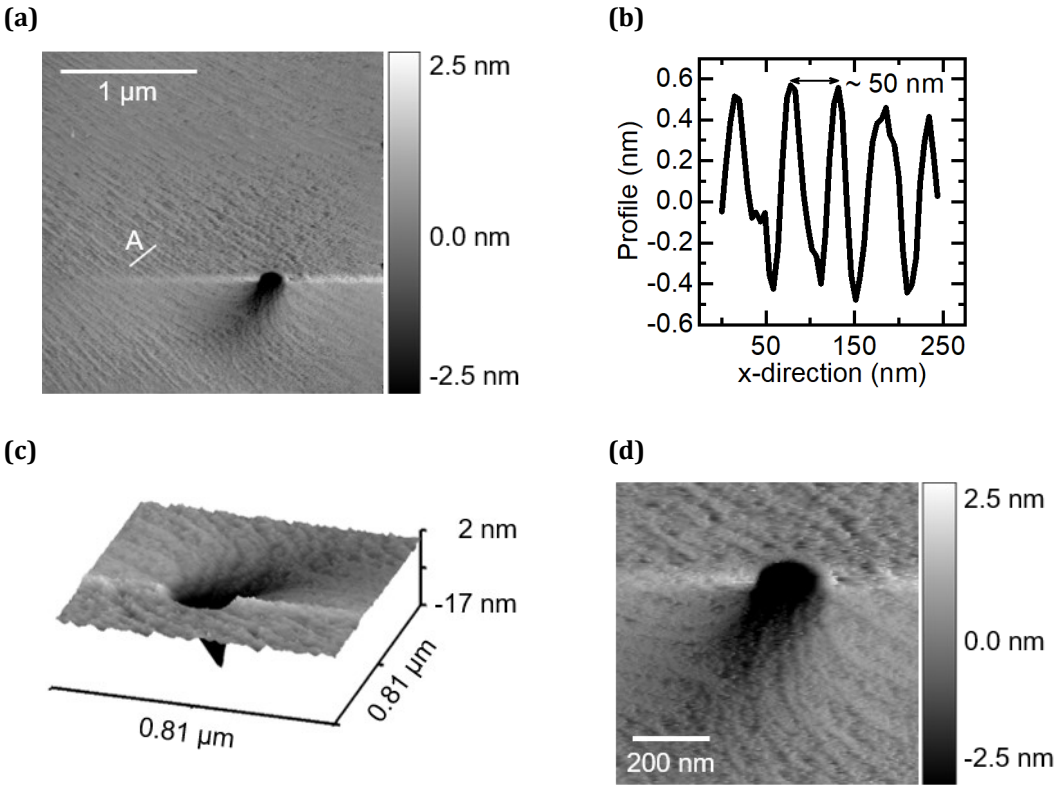

Figure 4.6: (a) Topography of the p-type sample at 3.0 V and 1 nA, **(b)** profile of the line marked A on the topography, **(c)** 3D representation of the observed pit in the topography image, **(d)** zoom of the area around the pit

The variation of the integrated luminescence intensity as a function of tunneling bias is shown in **Figure 4.7**, for different injected current.

The general trend is similar to the one observed in our other samples S10 and S90 (**Chapter 3.2.1**) except that the onset appears at significantly lower bias. The threshold injection energy is even slightly lower than the expected difference between the p-GaN conduction band minimum and the Fermi level and only slightly higher than the transition energy in the QW. This behavior is comparable to those in LEDs and hints to a different perpendicular transport mechanism. The same is observed for different tunneling currents.

The current-normalized integrated STL intensity curves show all the same variation except for 2 nA injected current. The intensity reaches a plateau for a bias voltage that exceeds the STL threshold by about 1 V. This might be related to electron transport in the first side valley of the conduction band. At a tunneling current of 2 nA, the STL intensity saturates just beyond the threshold and then slightly decreases. The reason behind this behavior could be a different injection or transport regime at low current density.

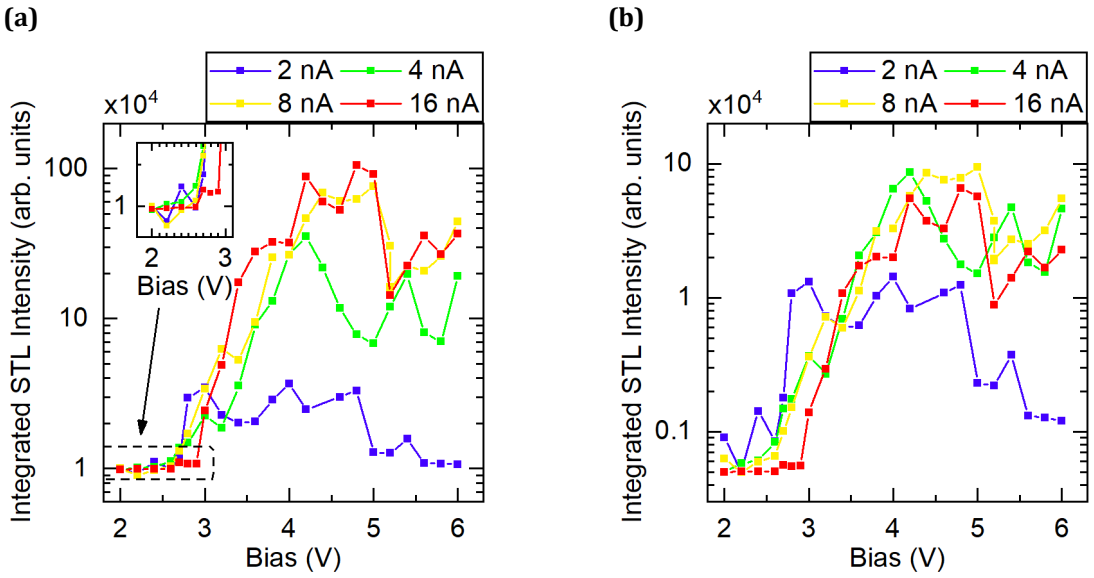

Figure 4.7: Integrated STL intensity against the applied bias voltage at different tunneling currents: **(a)** raw data and **(b)** current-normalized data.

4.3.2 STL spectroscopy

The effect of screwing dislocations on the IQE of nitride LEDs are a controversially debated topic (see **Chapter 1.2**). The high spatial resolution and local probe of STL might be a promising approach to probe those defects and settle this discussion.

We perform a line scan with 4 nm step size across the V-pit shown in **Figure 4.6**. The results of this line scan are plotted in **Figure 4.8**. We observe variations in the intensity. In particular, the emission intensity decreases significantly when the tip drops deeply into the V-pit. The corresponding position range is marked in gray on the profile of the pit in **Figure 4.8 (b)** and delimited by black spectra in **(c)**. Although one might conclude that emission is less efficient in V-pits, the emission decrease might be due to the changed injection on the tilted surface of the V-pit and/or to the subsequent transport.
Apart from the intensity fluctuations, we observe weak fluctuations of the spectra line shape at the scale of the scanning step as shown in **Figure 4.8 (d)**. For instance, the peak energy fluctuates by less than 10 meV over the entire line scan which is less than what is expected for alloy disorder-induced localization effects in InGaN QWs. As for the S10 and S90 in **Chapter 3**, we can deduce a positive linear correlation between the peak energy E_P and the low-energy half width at half maximum W_{LE} and a negative linear correlation between E_P and the high-energy half width at half maximum W_{HE} with a Pearson correlation factor (see **Appendix A**) of:

$$r_{Soraa,LE,line} = 0.3230,$$

and respectively,

$$r_{Soraa,HE,line} = -0.6171.$$

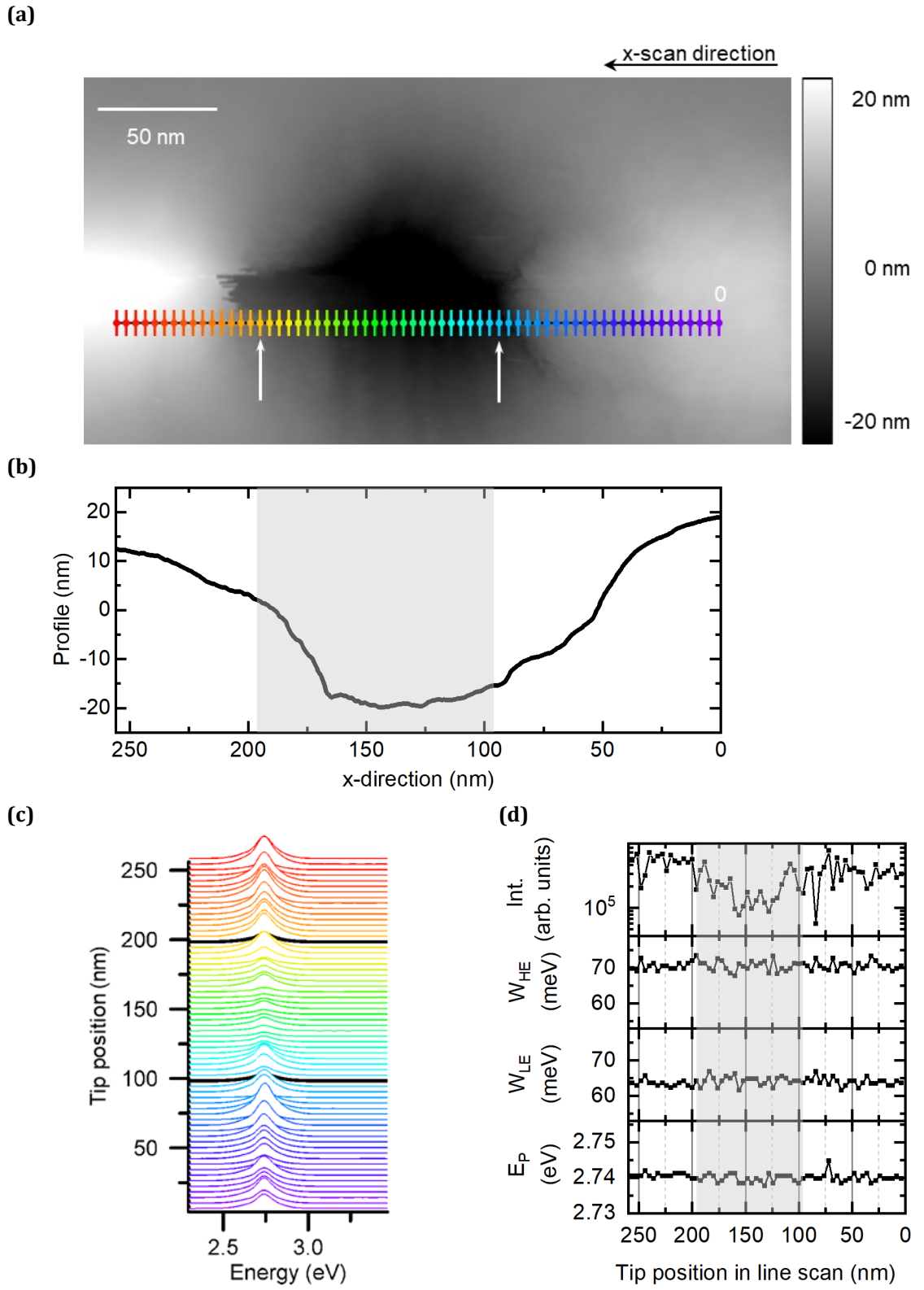

Figure 4.8: (a) STM topography image in the vicinity of a V-pit. Line scan direction and positions of the recorded spectra along the line scan are indicated. The tunneling bias and current are 4.5 V and 16 nA. **(b)** Profile of the V-pit. **(c)** Spectrum evolution along the line scan. Spectra colors correspond to the color scale of the tip position indicated in **(a)**. Black spectra correspond to the position indicated by arrows on the pit edges. **(d)** Data analysis of the spectra shape as described in **Appendix A**.

Additionally, we performed 2D STL maps on an area of 64 nm × 64 nm exhibiting a flat topography (out of the V-pit). The tunneling bias and current are 4.5 V and 4 nA. Spectra are recorded with 4 nm spacing. The results are shown in **Figure 4.9**. Here again, the intensity fluctuations are large as can be seen in **Figure 4.9 (a)** and **(b)**. In contrast, fluctuations in the peak energy E_P are rather small (~ 10 meV) when compared to those observed on S10 sample in **Chapter 3**. However, they are highly correlated with the fluctuations of W_{LE} and W_{HE} as shown in **Figure 4.9 (c).** The values of the Pearson correlation factor between E_P and W_{LE} and between E_P and W_{HE}, respectively, are:

$$r_{Soraa,LE,map} = 0.7535,$$

and:

$$r_{Soraa,HE,map} = -0.6799,$$

for E_P against W_{HE}.

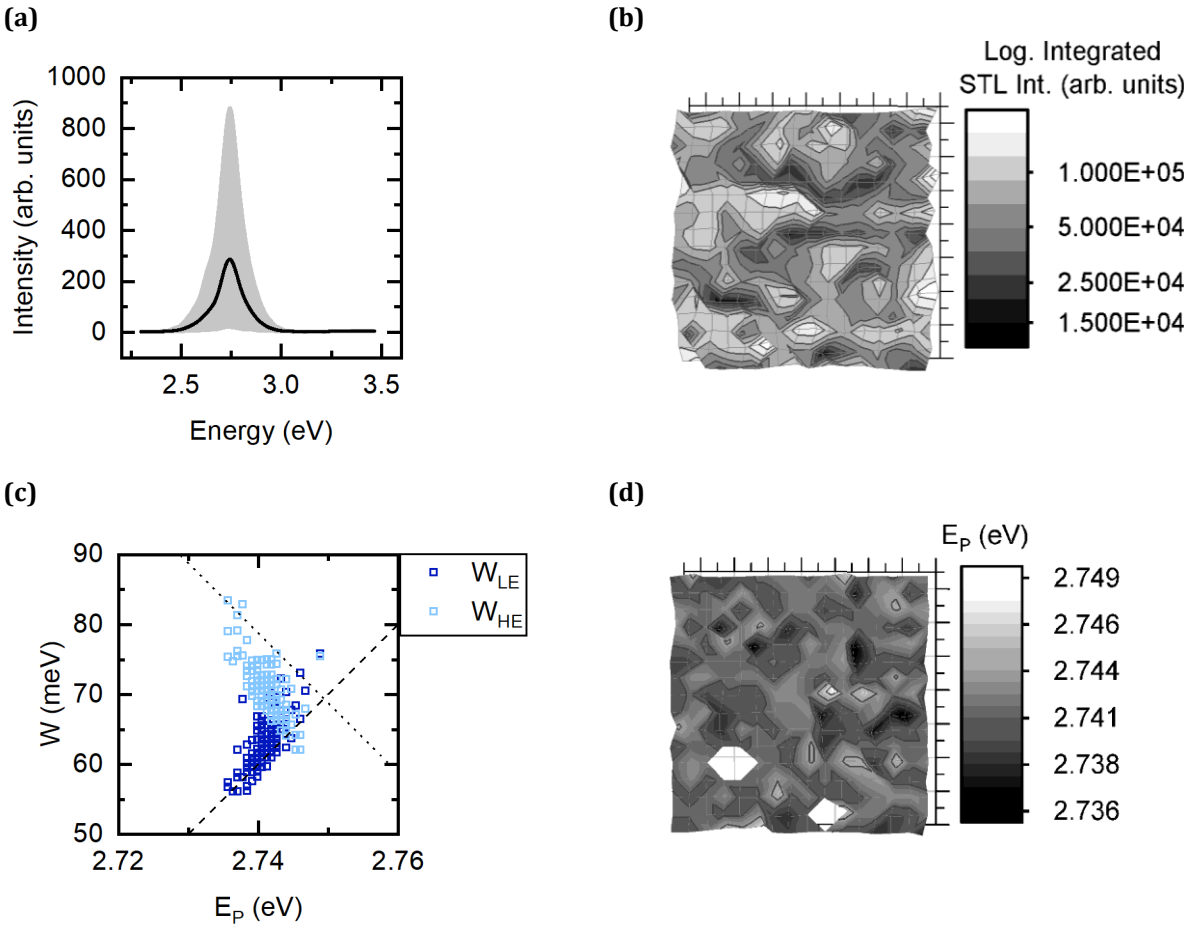

Figure 4.9: 64 nm × 64 nm STL map measurement on a flat area of the Soraa Inc. sample surface. The tunneling bias and current are 4.5 V and 4 nA. The spectra are recorded at the nodes of a grid of 4 nm mesh size. **(a)** Averaged spectrum over the map. The gray envelope is delimited by the minimum and maximum intensity for each emission energy. **(b)** Integrated STL intensity map in logarithmic scale **(c)** Peak energy against W_{LE} and W_{HE} deduced after the data treatment of the map spectra (as described in **Appendix A**). Dashed line has a slope of 1 whereas the dotted line has a slope of -1. **(d)** E_P map.

The map of E_P, shown in **Figure 4.9 (d)**, exhibits fluctuations at a scale comparable to the characteristic size of the localization regions seen in the potential maps calculated with the LL

theory. The overall weaker fluctuations in the STL line shape observed on this sample from Soraa Inc. compared to the S10 sample of equivalent structure might be due to a change in the in-plane transport. Lower potential fluctuations induced by the alloy disorder of lower In concentration might explain this behavior. Alternatively, it might be caused by the higher growth quality of these samples which favors longer diffusion length and electron spreading in the GaN cap layers. To gain a better understanding of the underlying cause, however, further experiments beyond these preliminary results are necessary.

4.4 STL on n-type nitride heterostructures: localization of holes

Theory predicts that holes are even more strongly localized than electrons due to the potential fluctuations induced by alloy disorder [53]. To study hole localization with STL, n-type structures are required. Nevertheless, tunneling injection and transport of hot holes is a challenging issue. We intend to perform STL measurements on two types of samples: a n-doped DQW structure similar to the p-doped DQW structure presented in section **4.1** and **4.2**, and a n-doped SQW sample grown at Soraa Inc., identical to the p-doped sample studied in the previous section **4.3**. For these two samples, no STL signal was detectable. In both samples, the distance between the surface and the (first) QW is 30 nm. Our assumption is that this distance is too large for injected holes to reach the QW and recombine radiatively. Despite the higher sample quality due to growth under industrial standards in the SQW sample from Soraa Inc.

A new SQW n-type sample structure in which the QW is closer to the surface [**Figure 4.10 (a)**] was thus grown via MOCVD by Yi Chao Chow at the University of California in Santa Barbara. The QW has a nominal In content of 14%. On top of the QW, an UID n-type GaN layer of only 12 nm thickness was grown. Below the QW, a 50 nm-thick UID doped GaN, followed by an UID InGaN/GaN superlattice of 20 repetitions with InGaN wells of 5% In content, of thickness of ~2 nm and 4.4 nm-thick GaN barriers. This stack was grown on a n-GaN buffer layer of 4 µm deposited on a double side polished sapphire substrate. To apply the tunneling bias potential to the lightly n-doped UID GaN cap layer, a specific Ti/Au (30/500 nm) contact schematized in **Figure 4.10 (b)** was grown and patterned on the sample surface.

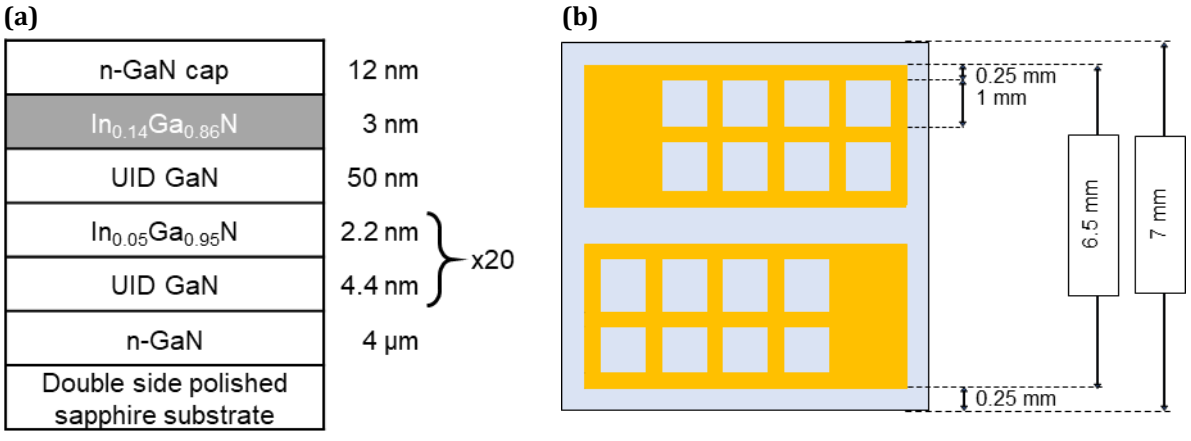

Figure 4.10: (a) Schematics of the single QW n-type InGaN/GaN heterostructure with a smaller cap layer. **(b)** Ti/Au contact patterned on the n-type InGaN/GaN heterostructure.

After cleaning, the sample was inserted in the chamber of the UHV STL with a pressure of 3×10^{-8} mbar. The PL spectrum of the sample recorded in-situ is shown in **Figure 4.11**.

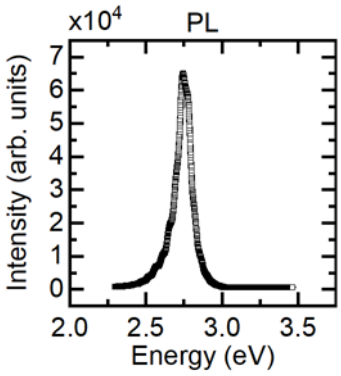

Figure 4.11: In-situ PL spectrum of the n-type sample recorded with ~15 mW incident power and 378 nm excitation wavelength.

The surface topography obtained by STM, shown in **Figure 4.12 (a)**, agrees well with the beforehand taken atomic force microscopy measurement by the grower. It exhibits the usual atomic step structure with pits emerging from dislocations. Continuous scanning over the same area, however, leads to a drastic change in the surface topography images of **Figure 4.12 (d)** and **(e)**, as well as in the STS-characteristics shown in **Figure 4.12 (b) – (c)** and **(f) – (g)**.

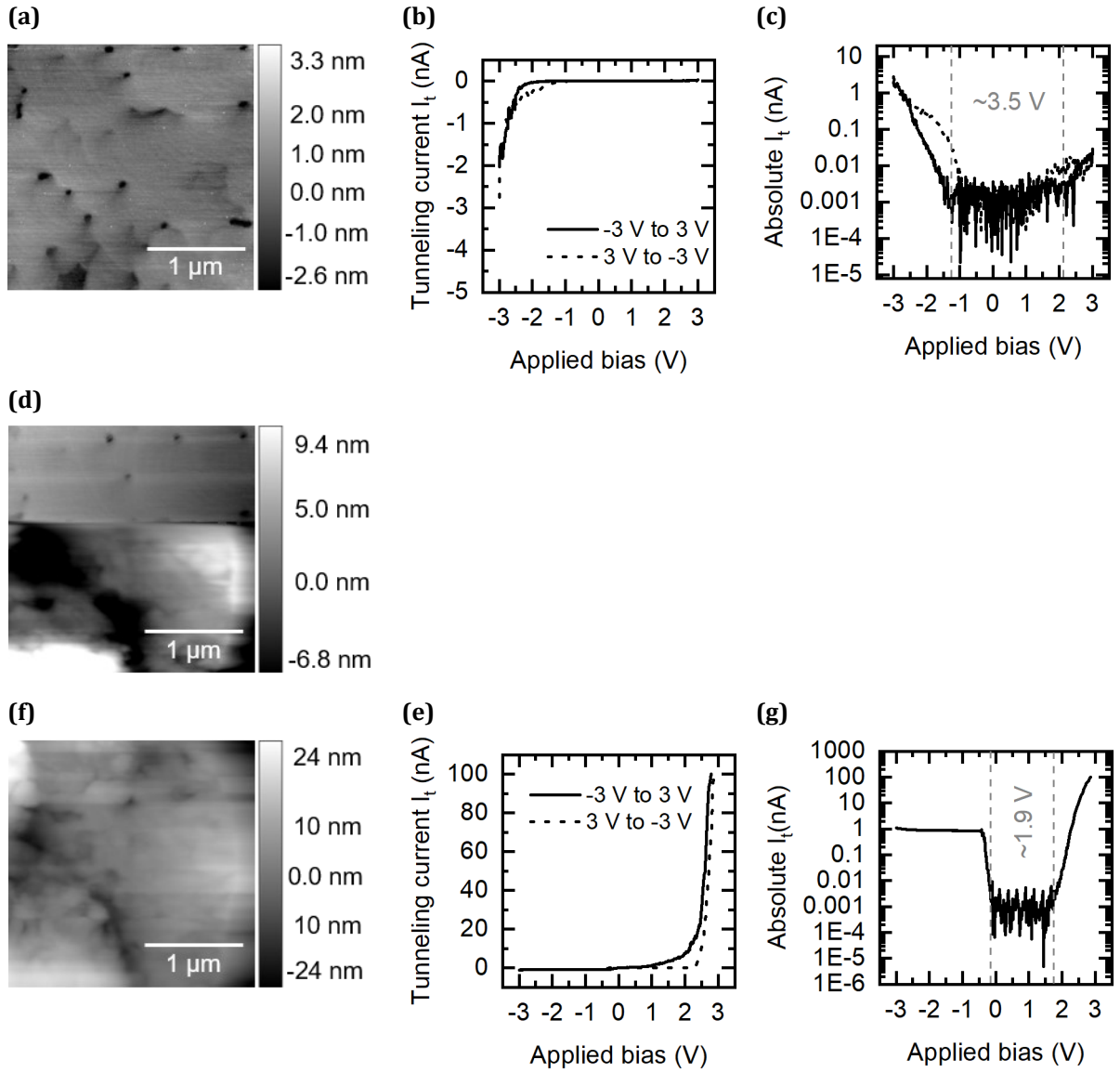

Figure 4.12: Topography of the n-type sample at -2.8 V and -1 nA **(a)** without charge accumulation with corresponding IV-characteristic **(b)** in linear scale and in logarithmic scale **(c)**. **(d)** Topography image of the same area with sudden switch in the surface due to charge accumulation and **(e)** fully charged surface of the same area. IV-characteristic of charge accumulation in **(f)** in linear scale and **(g)** in logarithmic scale.

These changes in the topography and STS-characteristics are the results of accumulated charges. This charge accumulation might origin from the low doping of the sample. It can be cured by shining light to create photocarriers. However, shining light with above bandgap light excitation on the sample is not compatible with STL measurements since the photoluminescence signal is much larger than the STL signal. Nevertheless, it is possible to measure the STL signal by performing STL measurements in the dark and shining light between STL measurements to remove the accumulated charges. The STL spectra obtained by this sequence of measurements and lighting are shown in **Figure 4.13**. The measurements were performed inside and outside a pit. We stress that with the negative bias potential applied to the tunneling junction, holes are injected in the GaN valence band and their recombination in the InGaN QW is detected.

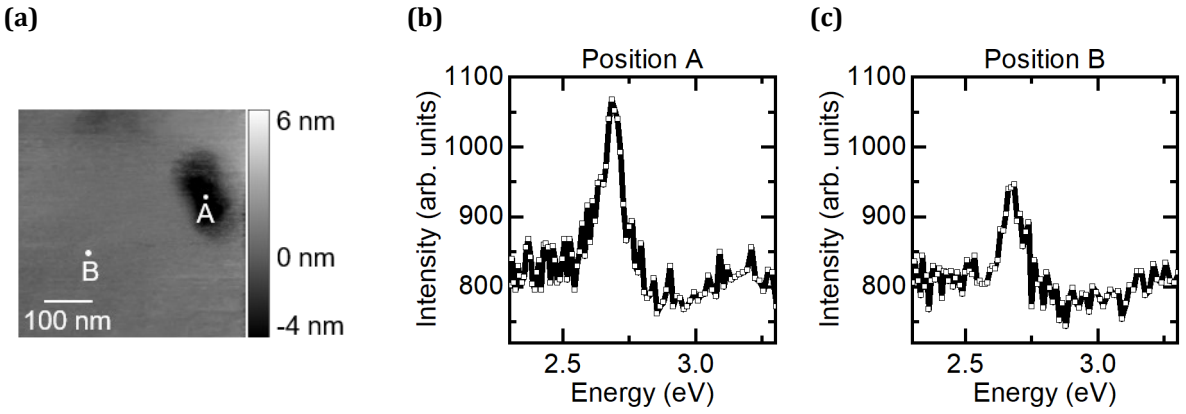

Figure 4.13: (a) STM topography of n-type sample measured under illumination in the vicinity of a pit. **(b)** and **(c)** STL spectra without background correction taken at -10 V and -16 nA, respectively, at position A, inside pit, and position B, outside pit.

These preliminary results are encouraging. Still, the values of the tunneling bias and current used here to obtain a rather low STL signal are very high. Therefore, the study of holes localization in InGaN/GaN heterostructures will require to grow samples with higher n-type doping in order to be able to perform STL measurements in acceptable conditions.

5 Conclusion and perspectives

In this thesis we have investigated disorder-induced localization effects in nitride semiconductor compounds and devices. This disorder in nitride ternary alloys is an intrinsic material characteristic stemming from the random distribution of atoms on the crystal lattice. The corresponding fluctuations of composition are responsible for potential fluctuations at a characteristic scale of a few nanometers which induce localization effects which are suspected to have a major impact on the performances of nitride-based LEDs.

The experimental investigation of alloy disorder effects is not trivial since the typical disorder length scale is in the nanometer range. Previous attempts to measure this intrinsic material were only able to probe larger fluctuations, e.g., extrinsic properties originating from growth inhomogeneities [45,48,87–90]. We use scanning tunneling electroluminescence (STL) on a near-surface single Gan/InGaN/GaN QW heterostructure to locally probe the electronic processes at the scale of the InGaN alloy disorder.

We observe narrow emission lines characteristic of emission from single localized states. The emission from these single localized state decreases with tip position over distances of about 10 nm. This decay is compatible with an in-plane transport scheme based on hopping between localized states of the disordered potential. Furthermore, in specific cases, the variation of single state emission as a function of the tunneling injection conditions (bias and current), reveals phenomena which might be related to Coulomb blockade, quantum mechanical level repulsion or bi-exciton emission.

In addition to the direct observation of single localized state emission, fluctuations in the line shape of the local electroluminescence spectrum as a function of the tip position are observed at a scale of a few nanometers which is characteristic feature of the alloy disorder.

These experimental results are in good agreement with the so-called localization landscape theory [40–42] which provides an effective confining potential map for the carriers (holes as well as electrons) exhibiting localization regions on the scale of 5 nm.

Furthermore, we also present preliminary results on ongoing investigations of several key issues. We show that the problem of perpendicular transport and STL resolution can be addressed by studying DQW structures.
Temperature is a key parameter to probe electronic processes, in particular in the presence of localization. However, performing electroluminescence measurements in nitrides at low temperatures is challenging due to the poor conductivity of the p-type materials. We present some preliminary results which show that STL measurements can be performed at low temperature to probe locally the transport and recombination processes.

Besides our studies on p-type structures, we investigate n-doped GaN/InGaN/GaN heterostructures to address the problem of localization of holes which is predicted to be even stronger than for electrons [53]. We are able to demonstrate hole injection and recombination in a lightly n-doped SQW structure. However, further investigations should be performed on n-type structures with higher cap layer doping.

Beyond the work presented in this manuscript, there are still many open questions and issues related to alloy disorder effects in nitride materials and devices. One of these issues is the investigation of how the disorder-induced localization effects build up and whether it is a transition from a regime of weak localization to strong localization. To tackle these questions, a study of InGaN/GaN structures in the low alloying range must be studied. This is the objective of an ongoing project.

Furthermore, ternary alloys such as AlGaN are also used as barriers in nitride devices. These barriers are, thus, also affected by compositional disorder which should induce localization effects and/or percolation paths. **Figure 5.1** shows the results of an APT reconstruction and concentration profile of a GaN/AlN/AlGaN structure.

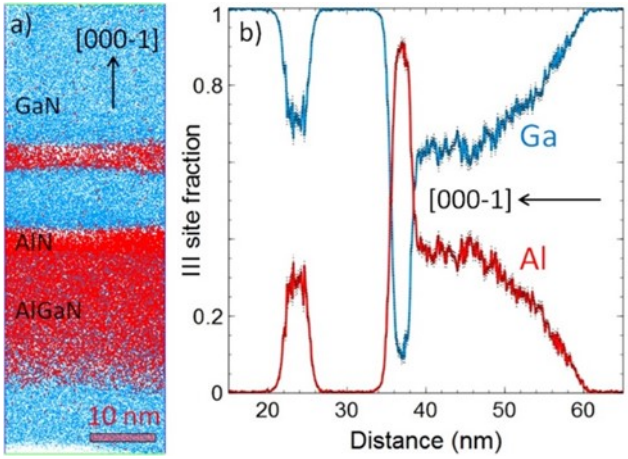

Figure 5.1: (a) 3D reconstruction from APT of GaN/AlN/AlGaN heterostructure and (b) respective 1D Ga and Al concentration profiles (measured in III-N ratio, e.g., Ga-N, Al-N). Reprint from [11].

An understanding of the impact of disorder on the barrier efficiency is thus needed. STL is a very well-suited tool to study perpendicular transport through a near-surface AlGaN barriers. A schematic of the experiment that we plan to perform as well as of the relevant sample structure is shown in **Figure 5.2**. In this structure, the InGaN QW below the barrier is used as a detector of the electron transmitted through the barrier. This experiment should allow to map the barrier transmission at the nanometric scale as a function of the injected electron energy.

(a)

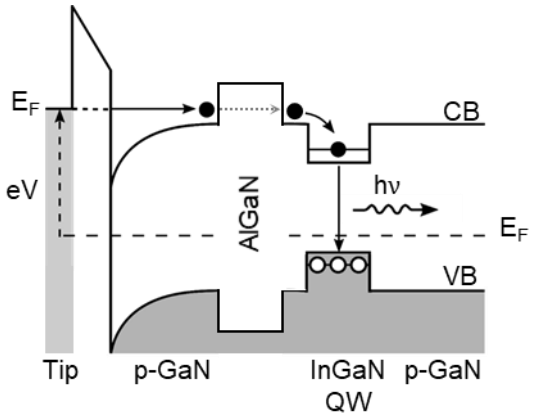

(b)

p+ cap contact layer	10 nm
p-AlGaN	10 nm
p-GaN	90 nm
UID GaN	10 nm
UID $In_{0.11}Ga_{0.89}N$	3 nm
UID GaN	100 nm
p-GaN	1 µm
p-AlGaN	15 nm
p-GaN	10 nm
n-GaN	1 µm
UID GaN	2 µm
nucleation layer	
Patterned Sapphire (0001)	

Figure 5.2: Schematic drawing to study the disorder in AlGaN barriers, **(a)** experimental procedure, **(b)** sample structure.

Although STL is an appropriate choice to have access to the electronic processes at the relevant nanometer scale, it misses a direct sensitivity to the actual local composition. This could be achieved by the related technique of scanning transmission electron microscopy (STEM). Indeed, recent developments have enabled to work with extremely small electron probes and to combine STEM with cathodoluminescence (CL) and Electron Energy Loss Spectroscopy (EELS). This technique delivers spatially correlated information on the light emission properties and the chemical composition [91]. Using both STL and CL-STEM-EELS on the same sample structure should allow to get a greater insight on the impact of the nitride ternary alloy disorder on the electron processes.

Along with the probing of localization effects in nitride materials, STL is also widely used to study emission from molecules adsorbed on surfaces [59] or excitonic luminescence in 2D semiconductors with an access to defect-induced localized emission [60]. Exciton and spin dynamics in semiconductors (including 2D materials) is one of the domains of expertise of our research group (Electrons-Photons-Surfaces) at the Laboratoire de Physique de la Matière Condensée. It is thus natural that future work in these domains will be carried out with our STL setups. We are currently implementing sample and tip preparation tools in our UHV STL setup. In particular, the fabrication of magnetic STM tips combined with the detection of polarized luminescence will give access to spin processes at the relevant scale to study for instance spin-dependent recombination near localized paramagnetic centers in III-V semiconductors.

A. Procedure for STL data analysis

A.1 Data treatment of STL spectra

In **Figure A.1 (a)** we show the example of a raw STL spectrum with a large background noise and a cosmic ray artefact. In **Figure A.1 (b)** we try to describe the spectrum with only thermal broadening, e.g., Gaussian, in **Figure A.1 (c)** with only lifetime broadening via a Lorentzian-fit, and in **Figure A.1 (d)** with a combination of both via a Voigt-fit.

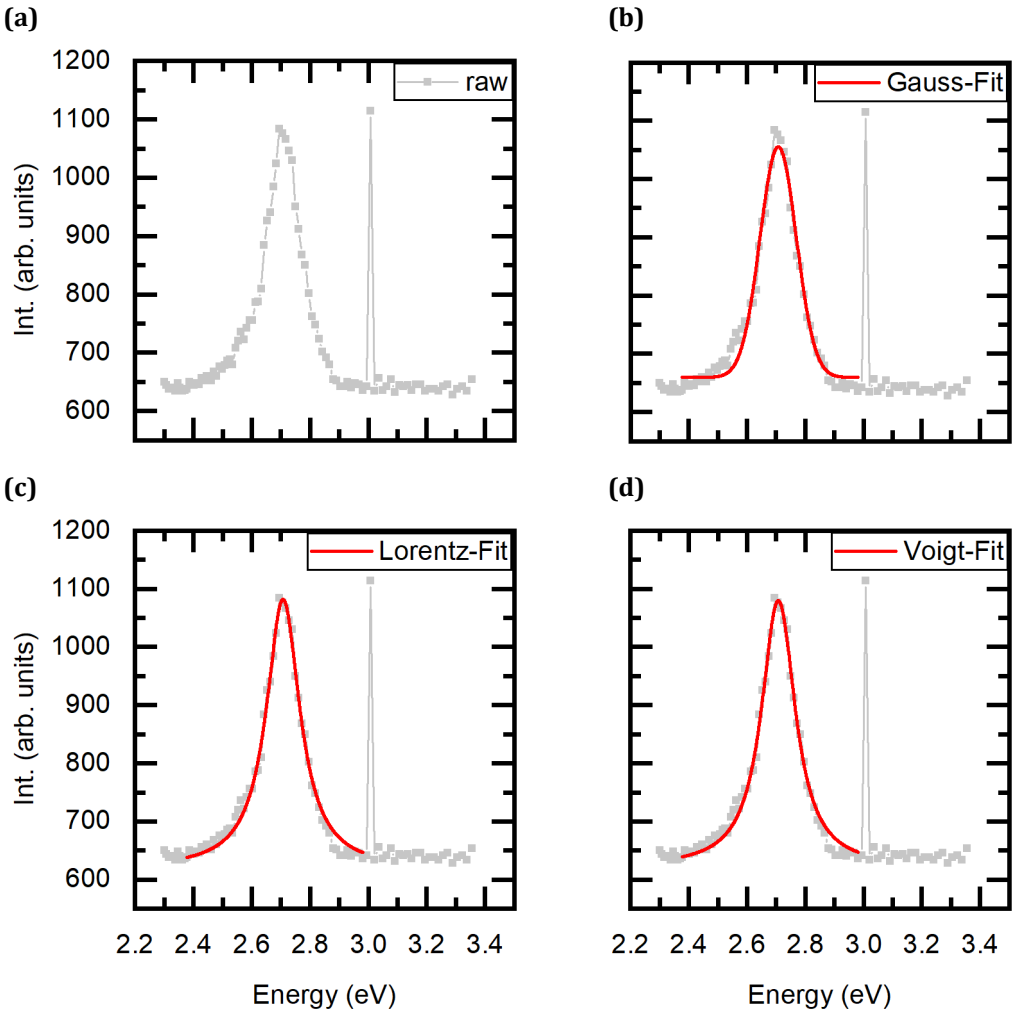

Figure A.1: Example of an STL spectrum: **(a)** raw data, **(b)** with a Gaussian-fit, **(c)** with a Lorentzian-fit, **(d)** with a Voigt-fit.

It is evident that none of the standard descriptions can capture the (asymmetric) broadening of the raw data. We have thus developed a reliable data treatment which allows to extract the integrated intensity, the peak energy, low-energy half width at half maximum, W_{LE}, and the high-energy half width at half maximum, W_{HE}. The W_{LE} and W_{HE} (defined below) allow us to reveal and

analyze the asymmetry of the STL line shape. The following data treatment includes the removal of artefacts, the background correction and a smoothing procedure based on the filtering of high frequency contributions in the spectra Fourier transform.

A.1.1 Elimination of artefacts

The first step of this analysis is to track spot artefacts such a cosmic ray detection. These parasitic lines manifest themselves as intense spikes of only a few pixels width (**Figure A.2**). Once such an artefact is identified, it is replaced by the average value of the surrounding points.

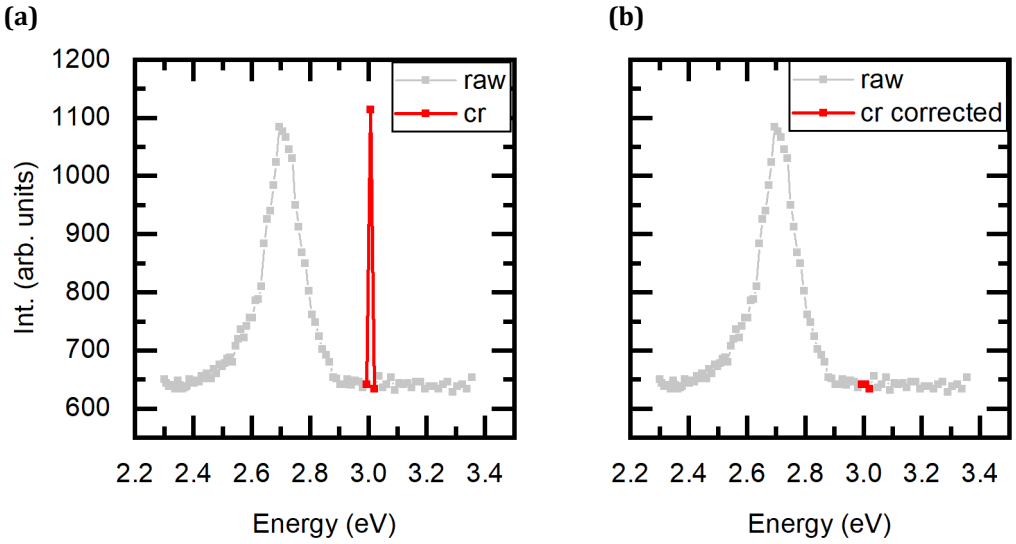

Figure A.2: (a) Raw spectrum with highlighted cosmic ray (cr). **(b)** Corrected cosmic ray by mean value of surrounding values.

A.1.2 Background correction

To account for the background noise of the light detector a linear fit of the baseline is carried out and subtracted from the raw data (see **Figure A.3**).

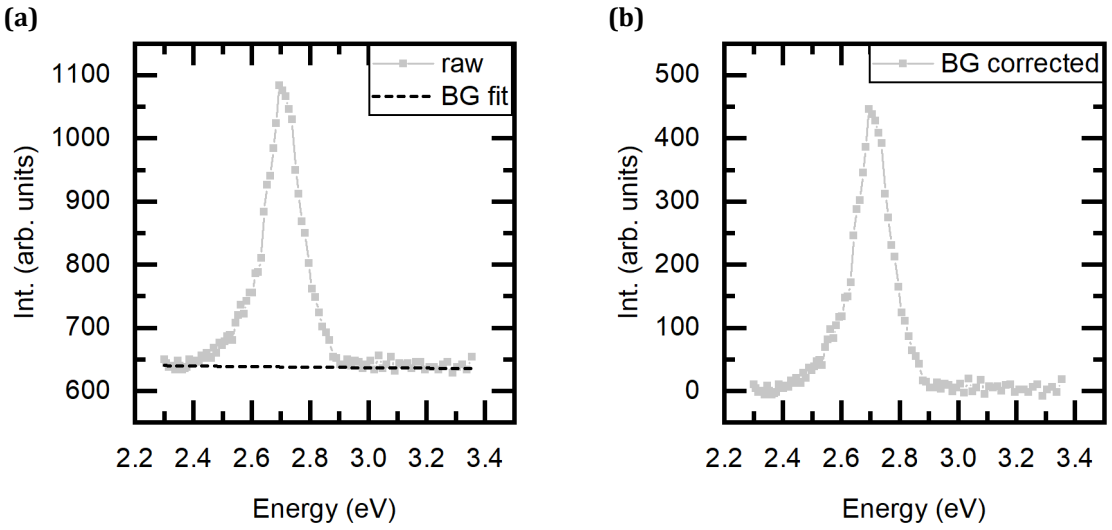

Figure A.3: (a) Cosmic ray corrected STL spectrum with linear background (BG) fit. **(b)** Background corrected spectrum.

A.1.3 Smoothing procedure

A sufficient signal-to-noise ratio is needed to perform a reliable automized analysis of the spectra. We, therefore, chose to only account for peaks with more than 40 counts above zero after the background correction. The key point of the spectra line shape analysis is the determination of the peak energy. The noise introduces an uncertainty on this determination. Therefore, the spectra have to be smoothed in most cases. The smoothing method used in the following is based on the mathematical process of Fourier transform which is applied via the algorithm of Fast Fourier Transform (FFT) implemented in the NumPy package of Python. An example spectrum and its FFT are shown in **Figure A.4**. The Fourier transform relates the collected waveform of the spectrum to its frequency domain. Moreover, it sorts the intensity and frequency present in the original spectrum; the relevant information is carried by the contributions occurring at low energetic frequencies. We chose a filter width slightly smaller than the corresponding resolution of the measurement so that higher frequencies contributions are mainly white noise and are cut out [74,92]. Then, the smoothed spectrum is obtained by reversed FFT.

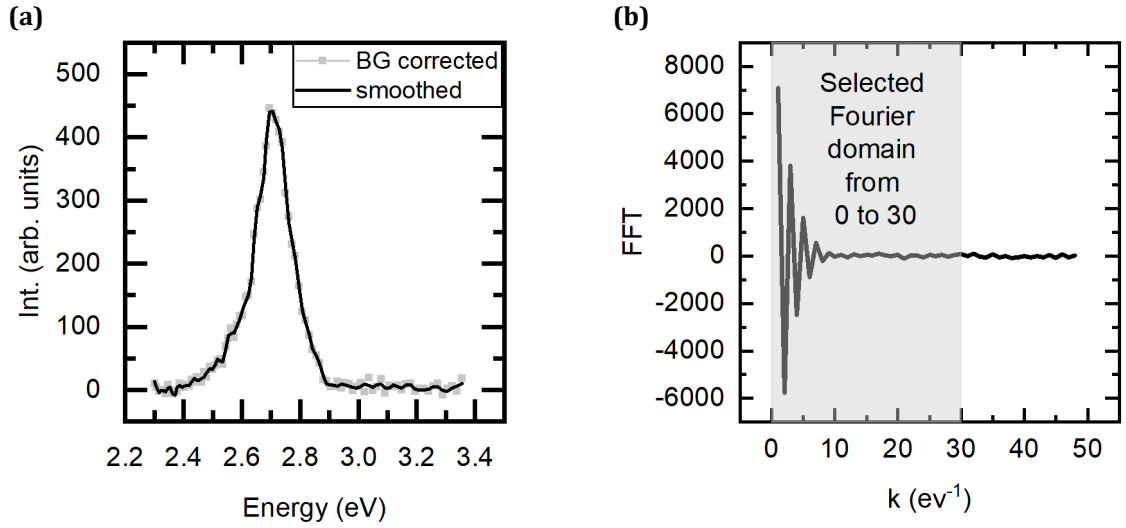

Figure A.4: (a) STL spectrum before (gray dots) and after (black line) fast Fourier Transform (FFT) filtering. **(b)** FFT of spectrum energy (k) the spectrum with the selected filtering interval.

A.1.4 Spectra analysis

The peak energy, E_P, is taken on the main contribution of each local STL spectrum. Then, we extract the energies E_{LE} and E_{HE} which correspond to the energy positions of the two extreme points of the spectrum at half of the peak intensity. The uncertainty on the determination of these energies is related to the spectrum acquisition sampling. The half widths at half maximum at low and high energy are then respectively equal to $W_{LE} = E_P - E_{LE}$ and $W_{HE} = E_{HE} - E_P$. Finally, the integral intensity is the sum over all the counts of the spectrum.

To finally extract these properties from each spectrum we have developed an automatized procedure based on the Python package PeakUtils [93]. We consider peaks above a threshold value of 40 counts and minimum width size of the peak of 20 meV.

In **Figure A.5** we exemplify on a selected spectrum the relevant quantities of E_P, W_{LE} and W_{HE}. Further examples are shown in **Chapter 3 Results** in **3.2 Analysis of STL spectra line shape**.

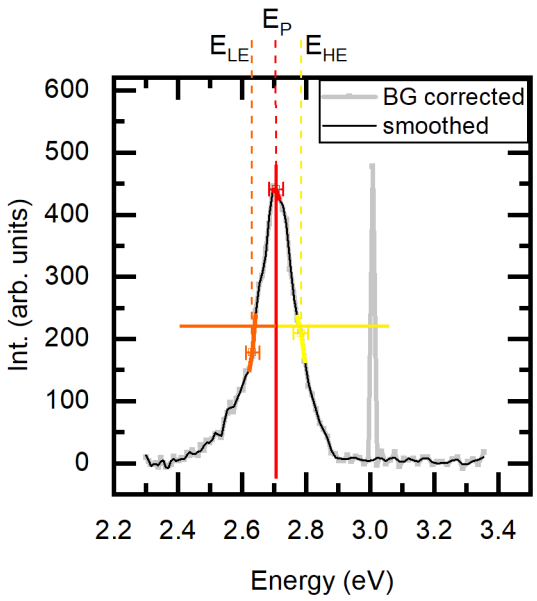

Figure A.5: Illustration of the data analysis of an STL spectrum after applying the data treatment. The values of the quantity extracted from this analysis are: peak energy E_P = 2.706 ± 0.022 eV, W_{HE} = 78 ± 23 meV, W_{LE} = 73 ± 20 meV.

A.2 Pearson correlation

To evaluate linear correlations, we use the Pearson correlation. The correlation coefficient *r* for n samples of × and y of average value $\bar{x}$ and $\bar{y}$ is defined as follows [94]:

$$r = \frac{\sum_{i=1}^{n}(x_i - \bar{x})(y_i - \bar{y})}{\sqrt{\sum_{i=1}^{n}(x_i - \bar{x})^2 \sum_{i=1}^{n}(y_i - \bar{y})^2}}$$

The correlation coefficient is in the range from -1 to 1 where 1 (respectively -1) represents a direct positive (respectively negative) linear correlation and 0 being no linear correlation. The value of r measures of the strength of correlation. The closer the value is to 1 (-1) the stronger the positive (negative) linear correlation is between the dataset of x and y [94]. An absolute value of 0.05 is considered significantly nonzero. In our case we use the Pearson correlation to identify the relation between E_P, W_{LE} and W_{HE}.

B. Comparison between our STL setups

In this thesis we show results from two different STL setups. On the one hand, we have an STL operating in air based on an Omicron CRYOSXM. On the other hand, we have an STL setups in UHV based on an RHK Technology's UHV 300 VT STM. To compare both our STL setups, we studied the SQW p-type sample grown under industrial standards by Soraa Inc., which were introduced in section **4.3.1**. In **Figure B.1** we show the results of line scans performed in the STL setup in air and map scans performed in the STL setup under vacuum (10^{-8} mbar) on these samples at 4.5 V and 16 nA.

Although a similar behavior in the integrated luminescence intensity against bias voltage is observed, their respective onset and plateau of luminescence intensity are shifted by more than 1.0 V. At this point, it is still unclear whether this is related to the operation in air, to the respective positioning of the tip to the contact or a rectifying behavior of the contact itself.

The STL spectra line shape and width are comparable. Despite a shift of the peak energy by 30 meV the range of exhibited peak energies is similar. The slight shift could originate from a growth inhomogeneity.

For both experiments a positive (negative) linear correlation between peak position energy E_P and low (high) energy width W_{LE} (W_{HE}) can be retrieved by the Pearson coefficient (see **Appendix A**). Their Pearson correlation coefficients are:

$$r_{\mathrm{vacuum,LE}} = 0.7350,$$

$$r_{\mathrm{air,LE}} = 0.6780,$$

and:

$$r_{\mathrm{vacuum,HE}} = -0.6284,$$

$$r_{\mathrm{air,HE}} = -0.5012.$$

Summarizing this comparison, we observe comparable results from both setups. For a final conclusion of the comparison between the two setups in air and under vacuum we suggest, however, further measurements on both the same and different samples.

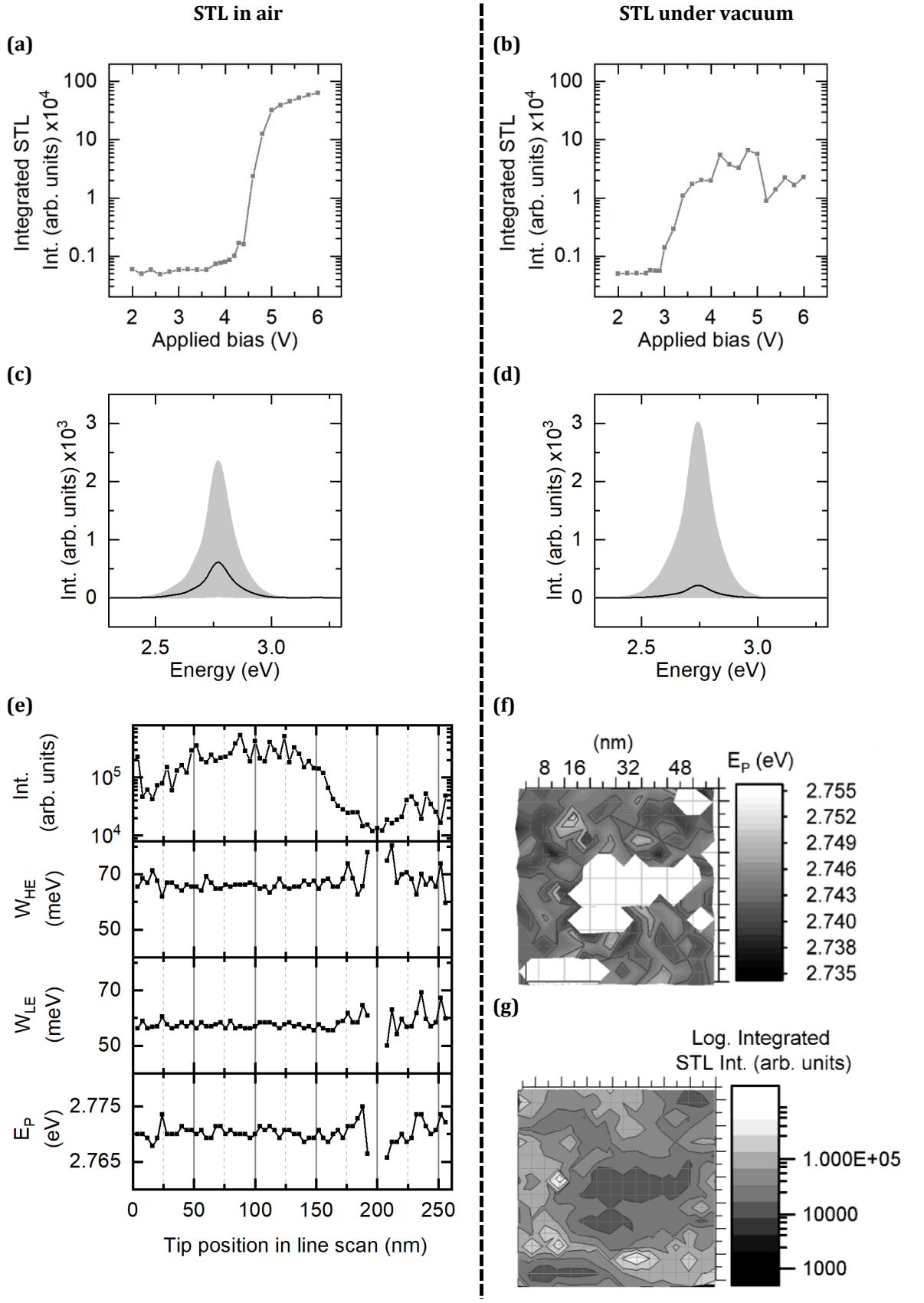

Figure B.1: Comparison of STL setup in air (left) and vacuum (right). **(a) – (b)** Average spectrum (black) in envelope of minimum and maximum of emission energy values. **(c) – (d)** Spatially integrated luminescence intensity versus applied bias voltage. **(e)** Data analysis of line scan (step size 4 nm) showing E_P, W_{LE}, W_{HE} and intensity of each spectrum. **(f)** E_P from map scan with step size 4nm. **(g)** Intensity at every position of map scan.

C. HRXRD measurements

We performed further investigation on the p-type and n-type SQW InGaN/GaN heterostructure grown under industrial standards at Soraa Inc. (see **4.3.1** and **0**) by using high resolved X-ray diffraction. The scan along the (004)-plane of p-type and n-type InGaN/GaN samples are shown in **Figure C.1**.

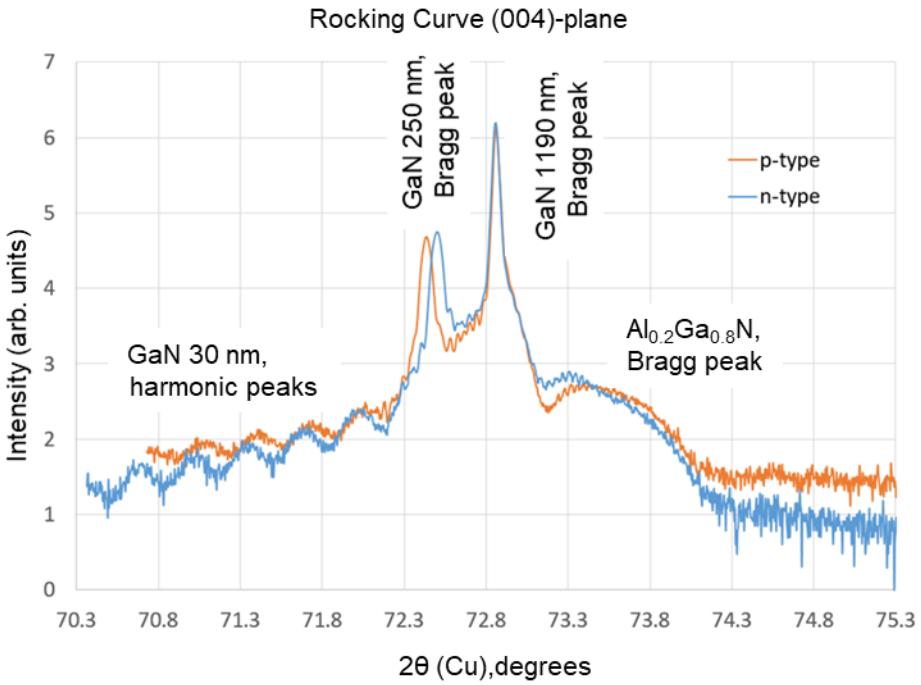

Figure C.1: HRXRD scan along the (004) plane of n-type and p-type InGaN/GaN heterostructure.

Due to the well-defined interference peaks (so-called harmonic peaks) we can determine the cap layer thickness to 30 nm in both samples. We resolve the Bragg peaks of the GaN layer at 250 nm depth as well as the substrate, and the AlGaN layer. However, the strong Bragg peaks of the GaN layers cover the contribution of the QW so that we can only extract the In concentration and quantum well width due to the change in amplitude of the interference pattern. Doing so, we retrieve for both samples an In concentration of 11% and QW thickness of 4 nm.

Bibliography

[1] T. A. Edison, "Electric lamp", US patent, US223898A (1880).

[2] K. Lehovec, C. A. Accardo, and E. Jamgochian, Phys. Rev. **89**, 20 (1953).

[3] H. G. Grimmeiss and H. Koelmans, Zeitschrift Fur Naturforsch. - Sect. A J. Phys. Sci. **14**, 264 (1959).

[4] R. Dingle, D. D. Sell, S. E. Stokowski, and M. Ilegems, Phys. Rev. B **4**, 1211 (1971).

[5] The Nobel Prize in Physics 2014. NobelPrize.org. Nobel Media AB 2020. Sat. 18 Jul 2020. <https://www.nobelprize.org/prizes/physics/2014/summary/>

[6] C. Weisbuch, Comptes Rendus Phys. **19**, 89 (2018).

[7] C. Weisbuch, ECS J. Solid State Sci. Technol. **9**, 016022 (2020).

[8] C. Weisbuch, M. Piccardo, L. Martinelli, J. Iveland, J. Peretti, and J. S. Speck, Phys. Status Solidi Appl. Mater. Sci. **212**, 899 (2015).

[9] U. S. DOE, *2018 Solid-State Lighting R & D Opportunities* (2019).

[10] S. Nakamura, T. Mukai, and M. Senoh, Appl. Phys. Lett. **64**, 1687 (1994).

[11] B. P. Yonkee, E. C. Young, S. P. DenBaars, S. Nakamura, and J. S. Speck, Appl. Phys. Lett. **109**, 191104 (2016).

[12] L. Y. Kuritzky, C. Weisbuch, and J. S. Speck, Opt. Express **26**, 16600 (2018).

[13] U.S. DOE, *Energy Savings Forecast of Solid-State Lighting in General Illumination Applications* (2019).

[14] A. Khan, K. Balakrishnan, and T. Katona, Nat. Photonics **2**, 77 (2008).

[15] K. J. Chen, O. Haberlen, A. Lidow, C. L. Tsai, T. Ueda, Y. Uemoto, and Y. Wu, IEEE Trans. Electron Devices **64**, 779 (2017).

[16] C. Netzel, H. Bremers, L. Hoffmann, D. Fuhrmann, U. Rossow, and A. Hangleiter, Phys. Rev. B **76**, 155322 (2007).

[17] D. Cherns, S. J. Henley, and F. A. Ponce, Appl. Phys. Lett. **78**, 2691 (2001).

[18] F. Jiang, J. Zhang, L. Xu, J. Ding, G. Wang, X. Wu, X. Wang, C. Mo, Z. Quan, X. Guo, C. Zheng, S. Pan, and J. Liu, Photonics Res. **7**, 144 (2019).

[19] C. Haller, J. F. Carlin, G. Jacopin, D. Martin, R. Butté, and N. Grandjean, Appl. Phys. Lett. **111**, 262101 (2017).

[20] C. Haller, J. F. Carlin, G. Jacopin, W. Liu, D. Martin, R. Butté, and N. Grandjean, Appl. Phys. Lett. **113**, 111106 (2018).

[21] M. Henini and M. Razeghi, *Optoelectronic Devices: III Nitrides* (Elsevier Ltd, 2005).

[22] K. Motoki, T. Okahisa, S. Nakahata, N. Matsumoto, H. Kimura, H. Kasai, K. Takemoto, K. Uematsu, M. Ueno, Y. Kumagai, A. Koukitu, and H. Seki, J. Cryst. Growth **237**–**239**, 912 (2002).

[23] M. J. Cich, R. I. Aldaz, A. Chakraborty, A. David, M. J. Grundmann, A. Tyagi, M. Zhang, F. M. Steranka, and M. R. Krames, Appl. Phys. Lett. **101**, 223509 (2012).

[24] H. Amano, M. Kito, K. Hiramatsu, and I. Akasaki, Jpn. J. Appl. Phys. **28**, L2112 (1989).

[25] S. Nakamura, T. Mukai, M. Senoh, and N. Iwasa, Jpn. J. Appl. Phys. **31**, 139 (1992).

[26] W. Götz, N. M. Johnson, J. Walker, D. P. Bour, and R. A. Street, Appl. Phys. Lett. **68**, 667 (1995).

[27] C. K. Li and Y. R. Wu, IEEE Trans. Electron Devices **59**, 400 (2012).

[28] D. W. Kim, Y. J. Sung, J. W. Park, and G. Y. Yeom, Thin Solid Films **398–399**, 87 (2001).

[29] J. Piprek, *Nitride Semiconductor Devices: Principles and Simulation* (Wiley-VCH Verlag GmbH & Co. KGaA, 2007).

[30] A. David, N. G. Young, C. Lund, and M. D. Craven, ECS J. Solid State Sci. Technol. **9**, 016021 (2020).

[31] J. Iveland, L. Martinelli, J. Peretti, J. S. Speck, and C. Weisbuch, Phys. Rev. Lett. **110**, 1 (2013).

[32] M. Auf Der Maur, A. Pecchia, G. Penazzi, W. Rodrigues, and A. Di Carlo, Phys. Rev. Lett. **116**, 027401 (2016).

[33] T. J. Yang, R. Shivaraman, J. S. Speck, and Y. R. Wu, J. Appl. Phys. **116**, 113104 (2014).

[34] H. Yoshida, M. Kuwabara, Y. Yamashita, K. Uchiyama, and H. Kan, Appl. Phys. Lett. **96**, 211122 (2010).

[35] M. Shahmohammadi, W. Liu, G. Rossbach, L. Lahourcade, A. Dussaigne, C. Bougerol, R. Butté, N. Grandjean, B. Deveaud, and G. Jacopin, Phys. Rev. B **95**, 125314 (2017).

[36] B. Gault, S. T. Loi, V. J. Araullo-Peters, L. T. Stephenson, M. P. Moody, S. L. Shrestha, R. K. W. Marceau, L. Yao, J. M. Cairney, and S. P. Ringer, Ultramicroscopy **111**, 1619 (2011).

[37] B. Bonef, M. Catalano, C. Lund, S. P. Denbaars, S. Nakamura, U. K. Mishra, M. J. Kim, and S. Keller, Appl. Phys. Lett. **110**, 143101 (2017).

[38] C. M. Jones, C. H. Teng, Q. Yan, P. C. Ku, and E. Kioupakis, Appl. Phys. Lett. **111**, 113501 (2017).

[39] M. Filoche and S. Mayboroda, Proc. Natl. Acad. Sci. **109**, 14761 (2012).

[40] M. Filoche, M. Piccardo, Y. R. Wu, C. K. Li, C. Weisbuch, and S. Mayboroda, Phys. Rev. B **95**, 144204 (2017).

[41] M. Piccardo, C.-K. Li, Y.-R. Wu, J. S. Speck, B. Bonef, R. M. Farrell, M. Filoche, L. Martinelli, J. Peretti, and C. Weisbuch, Phys. Rev. B **95**, 144205 (2017).

[42] C.-K. Li, M. Piccardo, L.-S. Lu, S. Mayboroda, L. Martinelli, J. Peretti, J. S. Speck, C. Weisbuch, M. Filoche, and Y.-R. Wu, Phys. Rev. B **95**, 144206 (2017).

[43] W. Hahn, J.-M. Lentali, P. Polovodov, N. Young, S. Nakamura, J. S. Speck, C. Weisbuch, M. Filoche, Y.-R. Wu, M. Piccardo, F. Maroun, L. Martinelli, Y. Lassailly, and J. Peretti, Phys. Rev. B **98**, 45305 (2018).

[44] J.-M. Lentali, Carrier Localization in Nitride-Based Semiconductor Alloys, Ecole Polytechnique, Palaiseau, France, 2020.

[45] K. Okamoto, J. Choi, Y. Kawakami, M. Terazima, T. Mukai, and S. Fujita, Jpn. J. Appl. Phys. **43**, 839 (2004).

[46] Y. Kawakami, A. Kaneta, A. Hashiya, and M. Funato, Phys. Rev. Appl. **6**, 044018 (2016).

[47] R. Ivanov, S. Marcinkevičius, M. D. Mensi, O. Martinez, L. Y. Kuritzky, D. J. Myers, S. Nakamura, and J. S. Speck, Phys. Rev. Appl. **7**, 064033 (2017).

[48] S. Chichibu, K. Wada, and S. Nakamura, Appl. Phys. Lett. **71**, 2346 (1997).

[49] S. Sonderegger, E. Feltin, M. Merano, A. Crottini, J. F. Carlin, R. Sachot, B. Deveaud, N. Grandjean, and J. D. Ganière, Appl. Phys. Lett. **89**, 232109 (2006).

[50] G. Pozina, R. Ciechonski, Z. Bi, L. Samuelson, and B. Monemar, Appl. Phys. Lett. **107**, 251106 (2015).

[51] D. Watson-Parris, M. J. Godfrey, P. Dawson, R. A. Oliver, M. J. Galtrey, M. J. Kappers, and C. J. Humphreys, Phys. Rev. B **83**, 115321 (2011).

[52] T.-J. Yang, R. Shivaraman, J. S. Speck, and Y.-R. Wu, J. Appl. Phys. **116**, 113104 (2014).

[53] S. Schulz, M. A. Caro, C. Coughlan, and E. P. O'Reilly, Phys. Rev. B - Condens. Matter Mater. Phys. **91**, 035439 (2015).

[54] M. J. Holmes, K. Choi, S. Kako, M. Arita, and Y. Arakawa, Nano Lett. **14**, 982 (2014).

[55] S. De, A. Layek, A. Raja, A. Kadir, M. R. Gokhale, A. Bhattacharya, S. Dhar, and A. Chowdhury, Adv. Funct. Mater. **21**, 3828 (2011).

[56] S. F. Alvarado, P. Renaud, D. L. Abraham, C. Schönenberger, D. J. Arent, and H. P. Meier, J. Vac. Sci. Technol. B Microelectron. Nanom. Struct. **9**, 409 (1991).

[57] P. Renaud and S. F. Alvarado, Phys. Rev. B **44**, 6340 (1991).

[58] C. Große, O. Gunnarsson, P. Merino, K. Kuhnke, and K. Kern, Nano Lett. **16**, 2084 (2016).

[59] K. Kuhnke, C. Große, P. Merino, and K. Kern, Chem. Rev. **117**, 5174 (2017).

[60] D. Pommier, R. Bretel, L. E. P. López, F. Fabre, A. Mayne, E. Boer-Duchemin, G. Dujardin, G. Schull, S. Berciaud, and E. Le Moal, Phys. Rev. Lett. **123**, 027402 (2019).

[61] P. Dumas, J. K. Gimzewski, M. Gu, C. Syrykh, J. K. Gimzewski, I. Makarenko, A. Halimaoui, and F. Salvan, Epl **23**, 197 (1993).

[62] S. Evoy, H. G. Craighead, S. Keller, U. K. Mishra, and S. P. DenBaars, J. Vac. Sci. Technol. B Microelectron. Nanom. Struct. **17**, 29 (1999).

[63] S. K. Manson-Smith, C. Trager-Cowan, and K. P. O'Donnell, Phys.Stat. Sol. **228**, 445 (2001).

[64] The Nobel Prize in Physics 1986. NobelPrize.org. Nobel Media AB 2020. Sun. 19 Jul 2020. <https://www.nobelprize.org/prizes/physics/1986/summary/>

[65] D. A. Bonnell, *Scanning Probe Microscopy and Spectroscopy : Theory, Techniques, and Applications* (Wiley-VCH, Inc., 2001).

[66] P. Polovodov, Cathodoluminescence in Semiconductor Structures under Local Tunneling Electron Injection, Ecole Polytechnique, Palaiseau, France, 2015.

[67] C. J. Chen, *Introduction to Scanning Tunneling Microscopy* (Oxford University Press Inc., 2008).

[68] Y.-R. Wu, *One Dimensional Poisson, Drift-Diffusion, and Schrodinger Solver (1D-DDCC), http://yrwu-wk.ee.ntu.edu.tw/index.php/ddcc-1d/* (2020).

[69] O. E. Tereshchenko, G. É. Shaibler, A. S. Yaroshevich, S. V. Shevelev, A. S. Terekhov, V. V. Lundin, E. E. Zavarin, and A. I. Besyul'kin, Phys. Solid State **46**, 1949 (2004).

[70] O. E. Tereshchenko, S. I. Chikichev, and A. S. Terekhov, Appl. Surf. Sci. **142**, 75 (1999).

[71] M. Piccardo, L. Martinelli, J. Iveland, N. Young, S. P. DenBaars, S. Nakamura, J. S. Speck, C. Weisbuch, and J. Peretti, Phys. Rev. B **89**, 235124 (2014).

[72] S. Marcinkevičius, T. K. UŽdavinys, H. M. Foronda, D. A. Cohen, C. Weisbuch, and J. S. Speck, Phys. Rev. B **94**, 235205 (2016).

[73] R. Aleksiejūnas, K. Nomeika, O. Kravcov, S. Nargelas, L. Kuritzky, C. Lynsky, S. Nakamura, C. Weisbuch, and J. S. Speck, Phys. Rev. Applied **14**, 054043 (2020).

[74] G. Horlick, Anal. Chem. **43**, 61A (1971).

[75] F. Intonti, V. Emiliani, C. Lienau, T. Elsaesser, V. Savona, E. Runge, R. Zimmermann, R. Nötzel, and K. Ploog, Phys. Rev. Lett. **87**, 076801 (2001).

[76] V. Savona, E. Runge, R. Zimmermann, F. Intonti, V. Emiliani, C. Lienau, and T. Elsaesser, Phys. Stat. Sol. **629**, 625 (2002).

[77] B. P. Zakharchenyaw and S. A. Permogorov, in *Encycl. Condens. Matter Physics, Excit. Theory* (Elsevier, 2005), pp. 166–171.

[78] G. Hönig, G. Callsen, A. Schliwa, S. Kalinowski, C. Kindel, S. Kako, Y. Arakawa, D. Bimberg, and A. Hoffmann, Nat. Commun. **5**, 4 (2014).

[79] A. David and M. J. Grundmann, Appl. Phys. Lett. **96**, (2010).

[80] D. Y. Oberli, J. Shah, T. C. Damen, J. M. Kuo, J. E. Henry, J. Lary, and S. M. Goodnick, Appl. Phys. Lett. **56**, 1239 (1990).

[81] T. Tada, A. Yamaguchi, T. Ninomiya, H. Uchiki, T. Kobayashi, and T. Yao, J. Appl. Phys. **63**, 5491 (1988).

[82] M. Mensi, R. Ivanov, T. K. Uždavinys, K. M. Kelchner, S. Nakamura, S. P. DenBaars, J. S. Speck, and S. Marcinkevičius, ACS Photonics **5**, 528 (2018).

[83] J. Danhof, U. T. Schwarz, T. Meyer, C. Vierheilig, and M. Peter, Phys. Status Solidi **249**, 600 (2012).

[84] J. Hegarty and M. D. Sturge, J. Opt. Soc. Am. B **2**, 1143 (1985).

[85] B. Gunning, J. Lowder, M. Moseley, and W. Alan Doolittle, Appl. Phys. Lett. **101**, 082106 (2012).

[86] A. David, N. G. Young, C. A. Hurni, and M. D. Craven, Phys. Rev. Appl. **10**, 031001 (2018).

[87] S. Kawakami, T. Sasaki, and M. Koashi, Phys. Rev. A **94**, (2016).

[88] R. Ivanov, S. Marcinkevičius, M. D. Mensi, O. Martinez, L. Y. Kuritzky, D. J. Myers, S. Nakamura, and J. S. Speck, Phys. Rev. Appl. **7**, 064033 (2017).

[89] S. Sonderegger, E. Feltin, M. Merano, A. Crottini, J. F. Carlin, R. Sachot, B. Deveaud, N. Grandjean, and J. D. Ganière, Appl. Phys. Lett. **89**, 232109 (2006).

[90] G. Pozina, R. Ciechonski, Z. Bi, L. Samuelson, and B. Monemar, Appl. Phys. Lett. **107**, 251106 (2015).

[91] M. Kociak and L. F. Zagonel, Ultramicroscopy **176**, 112 (2017).

[92] W. F. Maddams, Appl. Spectrosc. **34**, 245 (1980).

[93] L. H. Negri and C. Vestri, (2017).

[94] L. Fahrmeir, C. Heumann, R. Künstler, I. Pigeot, and G. Tutz, *Statistik - Der Weg Zur Datenanalyse, 8. Auflage* (Springer-Lehrbuch, 2016).

ECOLE DOCTORALE

Titre : Effets de localisation induite par le désordre dans les composés et dispositifs en nitrures semi-conducteurs

Mots clés : transport électronique, semi-conducteurs, GaN, microscopie à effet tunnel, luminescence, diodes électroluminescentes

Résumé : Il y a de plus en plus d'indications que le désordre d'alliage influence fortement les propriétés électriques et optiques des composés semi-conducteurs. Dans les alliages ternaires de nitrures, le désordre intrinsèque de composition, qui résulte de la distribution aléatoire des atomes sur le réseau cristallin, induit de forts effets de localisation électronique. Ces effets semblent avoir un impact majeur sur les performances des diodes électroluminescentes (LED) à base de nitrures, utilisées pour l'éclairage. Il est donc primordial d'aborder cette question car de très importantes économies d'énergie sont en jeu. Mais l'étude des effets du désordre d'alliage n'est pas triviale car l'échelle de longueur caractéristique pertinente est de l'ordre de quelques nm.

Au cours de cette thèse, nous avons utilisé la spectroscopie d'électroluminescence à effet tunnel pour détecter la recombinaison radiative d'électrons injectés localement par une pointe de microscope à effet tunnel dans un puits quantique de type GaN / InGaN / GaN, similaire à ceux qui constituent la partie active des LED. Des pics étroits, caractéristiques de l'émission à partir d'états localisés uniques, sont détectés. Les fluctuations de la forme du spectre d'électroluminescence tunnel sont observées à l'échelle de quelques nm, qui correspond à la taille caractéristique des régions de localisation induites par le désordre d'alliage, comme le prédit la théorie dite du paysage de localisation.

Title: Disorder-induced localization effects in nitride semiconductor compounds and devices

Keywords: scanning tunneling microscopy, luminescence, electron transport, semiconductors, light emitting diodes, GaN

Abstract: There are growing indications that alloy disorder controls to a large extent the electrical and optical properties of semiconductor compounds. In nitride ternary alloys, intrinsic compositional disorder, resulting from the random distribution of atoms on the crystal lattice, induces strong electronic localization effects. These disorder-induced localization effects are suspected to have a major impact on the performances of nitride-based light-emitting diodes (LEDs). It is therefore of primary importance to address this issue as huge energy savings are concerned. However, the investigation of alloy disorder effects is not trivial since the typical disorder length scale is in the nm range.

During this thesis, we developed a scanning tunneling electroluminescence (STL) spectroscopy experiment to detect the radiative recombination of electrons locally injected by a scanning tunneling microscope tip in a GaN/InGaN/GaN quantum well, similar to those present in the active region of LEDs. Narrow emission peaks are detected which are characteristic of emission from single localized states. Fluctuations in the line shape of the local electroluminescence are observed at the scale of a few nm which evidence localization effects induced by alloy disorder. These experimental results are in good agreement with the so-called localization landscape theory which provides an effective confining potential map for the carriers exhibiting nanometer size localization regions.

Institut Polytechnique de Paris
91120 Palaiseau, France